“As you think of more ways to use the tool, you imagine more goals it can help you accomplish”

~

David Dobbs

University of Alberta

Remote activation of a microactuator using a photo-responsive nanoparticle-polymer composite

by

Anthony Zeberoff

A thesis submitted to the Faculty of Graduate Studies and Research
in partial fulfillment of the requirements for the degree of

Master of Science

in

Materials Engineering

Department of Chemical and Materials Engineering

Fall 2013
Edmonton, Alberta

Abstract

Stimulus response materials are a class of novel materials that are currently being explored in various technologies, including biomedical devices and components, food packaging, fabrics, energy harvesting and conversion, and other elementary components such as sensors and actuators. Hybrid organic-inorganic materials such as nanoparticle-polymer composites are attractive candidates as their properties can be significantly tuned for particular applications where selectivity and localized responses are critical factors. In this work we developed and optimized a photo-responsive microactuator that can operate selectively to a specific wavelength of light. The photo-responsive microactuator is comprised of monodispersed microspheres that contain gold nanoparticles. Upon irradiation, these microspheres transduce optical energy to thermal energy, driving a localized phase change in the matrix in which they are embedded. Our remotely powered microactuator can be further realized in applications where decoupling the physical connection of the energy/control source from the actuating component is necessary.

Acknowledgements

I would like to foremost thank my supervisor Anastasia Elias for the rational input in structuring arguments and experiments, idea harvesting discussions, and general support along the way in this project.

Ken Harris and Ratmir Derda, the involvement I've had with your projects was a rewarding experience, thank you. I would also like to thank Joseph Mmbaga for the helpful discussions in computational modeling. Les Dean and Walter, you guys are great, for the helpful instrumentation discussions and resources you provided from the electronics shop.

Funding from the Canada Foundation for Innovation (CFI), CMC Microsystems, and the Natural Sciences and Engineering Research Council (NSERC) is gratefully acknowledged.

Table of contents

List of tables

List of figures

List of symbols

Au	gold
AuNPs	gold nanoparticles
PEGDA	polyethylene glycol diacrylate
PEG	polyethylene glycol
PDMS	polydimethylsiloxane
PMMA	polymethylmethacrylate
COC	cyclic olefin copolymer
pNIPAAm	poly N-isopropylacrylamide-co-acrylamide
LCST	lower critical solution temperature
SRM	stimulus response material
PCM	phase change material
LOC	lab on a chip
μTAS	micro total analysis
DSC	digital scanning calorimetry
Vis	visible
UV	ultraviolet
IR	infrared
Mn	number average molecular weight
V	volume
μL	microliter
D	diameter
h	actuation height
cm	centimeter
mm	millimeter
μm	micrometer
nm	nanometer
T	temperature
^{o}C	degrees Celsius
^{o}K	degrees Kelvin
ΔH_m	enthalpy of melting

C_p	specific heat capacity
Q	heat flow
h	heat transfer coefficient
k	thermal conductivity
ρ	density
P_t	optical transmitted power
P_i	optical incident power
A	optical absorbance
ε	molar absorptivity
c	molar concentration
l	optical path length
T	transmittance
m	mass
g	gram
mg	milligram
F	force
N	Newton
P	pressure
psi	pounds per square inch
wt%	weight percent
E	energy
J	Joule
W	Watt
mW	milliWatt
t	time
s	second
ms	millisecond
μs	microsecond
α	volume expansion coefficient
η	transduction efficiency

Chapter 1

Introduction[1]

1.1 Stimulus response materials

Stimulus response materials interact purposefully with their local environment, exhibiting a programmed response upon sensing a specific stimulus [1-5]. The development and integration of stimulus response materials is central to diverse applications, for example in microfluidics they are utilized in on-chip sensing and actuating components [6]; in medicine, for drug release vehicles [7]; and in bioengineering, for bioadhesion mediators [8]. Conceptually, a stimulus-response material (SRM) combines both sensing and actuating functions, as depicted in figure 1.1. The *sensing function* is synthetically programmed and *stimulated* by predetermined levels in energy, frequency, or concentration, etc. of its particular environmental stimulus such as light, heat, electric/magnetic fields, pH, ions, solvents, enzymes, molecules, and pressure; and the corresponding *response* of the SRM can be divided into two general categories: chemical changes, and/or conformation changes.

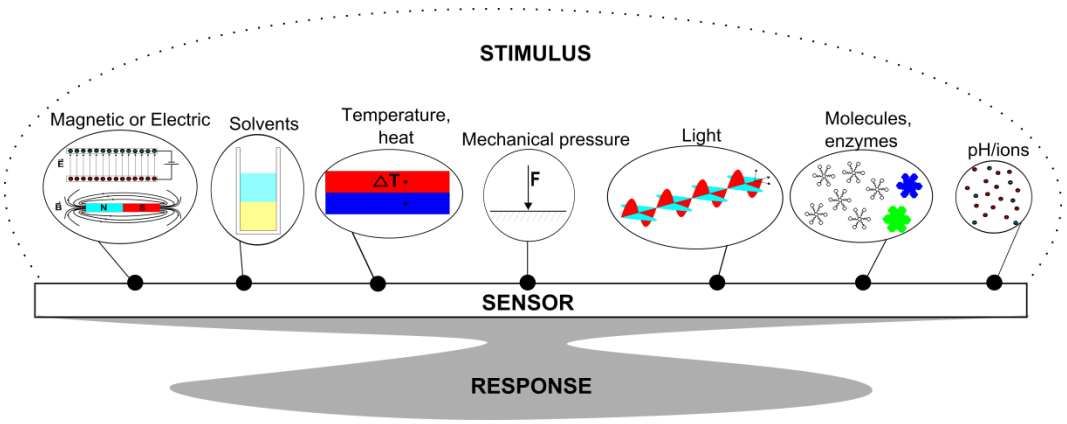

Figure 1.1: General architecture of a stimulus response material illustrating a host of possible stimuli.

Chemical responses include significant changes in intermolecular forces, where surface properties can be altered in the presence of a particular stimulus. Conformation changes of the constituent molecules can yield a mechanical response such as a change in

[1] Portions of this thesis are being submitted for publication

volume or shape. Some materials inherently combine sensing and responsive functions; for example the temperature-responsive polymer poly(N-isopropylacrylamide-co-acrylamide) (PNIPAAm) undergoes a transition from hydrophilic to hydrophobic when it is heated above its lower critical solution temperature, resulting in a volumetric change as water is expelled from the system. In other materials, transducing elements/agents/component are introduced to achieve the required functionality within the responsive material. A transducing agent is critical since it transduces energy from the stimulus to the responsive component. For example, to develop photo-responsive shape memory polymers, photo-sensitive chromophores were grafted to a polymer network, where initial irradiation ($\lambda > 260$ nm) fixed the material to a permanent shape while in a pre-strained condition, then the material was altered to a temporary different shape with no irradiation, and then final irradiation ($\lambda < 260$ nm) relaxed the polymer to return to the permanent initial shape [9]. In this case the chromophore acts as the transducer, sensing a predetermined frequency of light and transducing the optical energy to chemical energy, which initiates the formation of photoreversible crosslinks in the surrounding network. A highly selective stimulus-response hydrogel was developed by Miyata *et al* by grafting antigen and antibody molecules to a semi interpenetrating polymer network [10]. Upon introduction of a specific antigen into solution, the hydrogel underwent reversible swelling, which caused the grafted antigen-antibody bonding to detach from each other in the semi interpenetrating polymer network, resulting in preferential binding of the introduced antigen to the grafted antibody. Various SRM hydrogels that have been programmed to undergo volume changes in response to pH [11], electric fields [12], and temperature [13] have also been demonstrated.

Programming a high degree of selectivity into the SRM requires that the transducing nanoparticles be tunable to a specific stimulus. Nanoparticles – which can be blended with a variety of polymers to form composites – have also been explored as transducers, due to their ability to selectively and efficiently absorb light via surface plasmon resonance, transducing electromagnetic to thermal energy [14]. For example, it has been shown that gold nanoparticles (AuNPs) exhibit transduction efficiencies > 80% [15-18]. The process by which electrons on the surface of a nanoparticle (NP) oscillate with irradiant light is known as a surface plasmon resonance. The basic mechanism of heat generation from surface plasmon resonance is as follows: (1) First incident light at a specific wavelength is selectively absorbed on the surface of the NP by a resonating electron cloud; (2) Within the NP energy is then conserved through a thermalization

process as electrons oscillate and collide within the stationary gold ion matrix, effectively acting as a nanoheater [14]. Gold nanoparticles can establish resonance with light ranging from the ultraviolet to near infrared electromagnetic portions of the spectrum, and the wavelength/frequency at which resonance (i.e. selective absorption) occurs can be tuned by changing the diameter or shape of the nanoparticle. For example, spherical 10 nm AuNPs resonate with 532 nm wavelength light, whereas gold nanorods 12 nm wide by 80 nm long resonate at 1100 nm wavelength, as shown in figure 1.2 [14, 19, 20, 21].

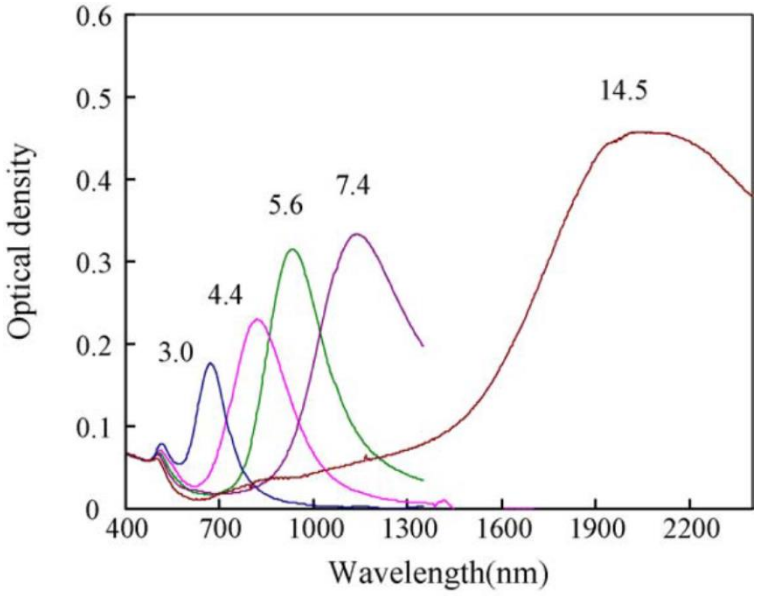

Figure 1.2: UV-Vis spectra of surface plasmon resonance peaks of gold nanoparticles in aqueous solution of different aspect ratios (L/d), where d is diameter and L is length [21]. Used with permission from Elsevier.

The size and shape of the nanoparticles can therefore be selected to program the response from a desired portion of the spectrum for the application of interest, for instance for *in vivo* applications a wavelength within the 'optical window' (where tissue is transparent, in the range 600-1300 nm) could be selected [22].

By combining tunable nanoheaters with thermoresponsive materials that undergo a volumetric change over a small temperature difference, a remotely-actuated SRM can be engineered, with a general scheme provided in figure 1.3.

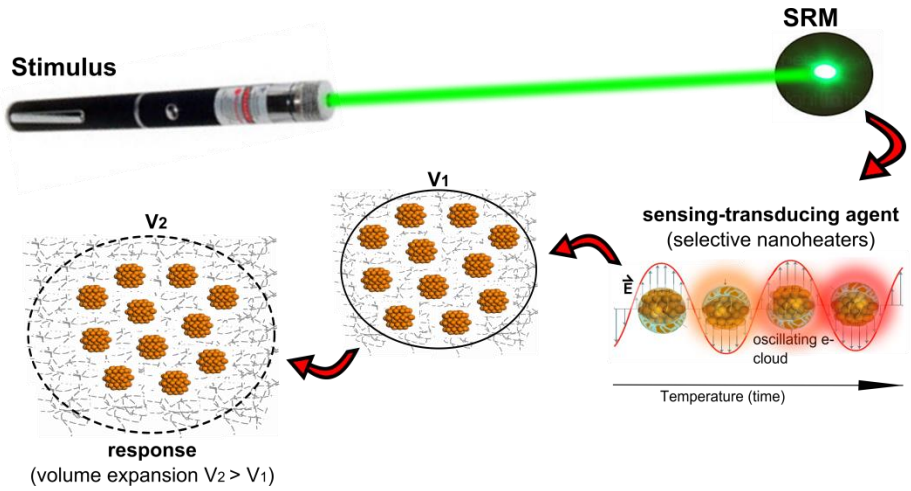

Figure 1.3: Remote laser stimulation on a stimulus response material. In the SRM, size or shape tunable nanoparticles selectively interact with a predetermined wavelength of light, effectively transducing electromagnetic to thermal energy. These thermally transducing nanoparticles combined with a thermoresponsive material induce volumetric expansion as the final response**.**

An SRM that is remotely 'switchable' or activated (using a laser, inductive heating coil, electric field, ambient temperature changes, etc.) between active and inactive physical states eliminates the physical connection of the stimulus and the SRM. Thus, remotely switchable materials – that are stimuli specific – are of particular interest in environments which are difficult to interface to external power supplies, such as in vacuum chambers, in the human body, or in reducing complexity in micro-scaled devices where connections must be lithographically patterned using a multi-step fabrication procedure [7, 8, 23]. For example, remotely activated stimulus responsive materials have been utilized to actuate the release of drugs from microcapsules made of a photoresponsive material [24], to provide on-chip heating in microfluidic devices (magnetically responsive) [25], to actuate artificial muscles (photo and thermally responsive) [26], and to change/restore shape in photoresponsive shape memory polymers [9]. Several investigations have also demonstrated the use of remote stimuli (magnetic/electric fields, and photons) as a means to control the mechanical actuator in microfluidic systems, as described below.

1.2 SRMs in Microfluidics

Microfluidic technology and science comprises the handling and sensing of biological and chemical fluid assays on a microscopic level [27, 28]. This technology will primarily find practical use in the medical industry where point-of-care devices can perform analysis on blood and other fluids, these devices are called "lab on a chip (LOC)" or

"micro total analysis systems (μTAS)" [29]. Establishing a microfluidic platform similar in size to current smart phones requires that current LOC prototypes be minimized in their footprint. Pumps and valves are the primary fluid flow manipulation components in a μTAS. Among conventional piezoelectric, shape memory alloy, electrostatic, and thermopneumatic actuators – pneumatically actuated valves and pumps have demonstrated highly effective and promising results for a LOC due to their reliable actuating membrane with large displacements, high speed pumping, and valve open-close cycles on the order of milliseconds [30-32]. For example, King *et al.* demonstrated that an array of integrated pneumatic microvalves on a single substrate was an instrumental component in the high speed parallel processing of biological assays [33]. However, pneumatic actuation requires both an off-chip pressure source and a pressure controller to regulate the pressure delivered to the on-chip microvalves and pumps [34]. Additionally, a plumbing infrastructure must support the off-chip and on-chip plumbing connection, which can easily be imagined to increase the overall size of the device. These added off-chip plumbing connections increase the size, cost, and power consumption on the overall device, therefor raising an upper engineering limit for pneumatically actuated microvalves. Nevertheless, some of the principles and materials in pneumatic based LOCs have acted as an analog for the growth of advanced and alternative mechanisms for controlling pumps and valves.

Implementing SRMs into the actuating components of microvalves and pumps has shown to reduce the energy consumption in the off-chip controllers [30]. For example, a hydrogel that swells and contracts in response to a high and low pH, respectively, has been demonstrated to act as the actuating mechanism in a microvalve [35]. Despite the reduced energy consumption, solvent stimulated hydrogel microvalves still require off-chip controllers with their complementary plumbing. One approach to eliminate on-chip plumbing has been to lithographically pattern integrated resistive-heaters and electrical conduit on the control layer of the chip. In these designs, thermal sensitive phase change materials such as copolymers, paraffin's or carbowax's are placed in a reservoir above the heater, which expand in volume or gel under thermal stimulation [31, 32, 36-39]. However, these designs require electrical connections to an off-chip power supply, which therefore limits the size of the device, since more on-chip components are required, and also require additional lithography patterning steps. Furthermore, the fact that the active material and the heating layer are independent from each other (yet still in contact) means

that heat is directly lost to its supporting substrate, which both limits the speed of the activation or deactivation cycle, and leads to undesirable heating in other parts of the device.

By decoupling the control (stimulus) system from the active layer, that is, removing the on-chip control circuitry required to power the actuator (active material) in microvalves, the off-chip and on-chip connection disappears while several benefits appear: the fabrication cost decreases (by eliminating lithography steps), and the size of the device can now be exclusively limited to the volume of the SRM required to induce adequate actuation. Naturally then, these SRMs must be activated by remote sources, such as radiation (UV, Vis, IR, etc.), electric or magnetic fields, or ambient temperature changes.

Several investigations have demonstrated the use of external photo-stimuli as a means to control the mechanical deformation of an SRM. Many of these microactuators exploit the temperature sensitive polymer PNIPAAm, which was described in section 1.1 above. Niten *et al.* used an alternating magnetic field to induce heating of magnetic nanoparticles dispersed in PNIPAAm, effectively dehydrating PNIPAAm, which demonstrated a reversible normally closed microvalve, however, with a relatively long open-close cycle of approximately 14 minutes [40]. In another study, PNIPAAm was functionalized with photoresponsive chromophores that undergo a solubility change in aqueous solution upon exposure to light, and an actuator was fabricated with this material that exhibited a reversible open-close cycle with a period of approximately 1 hour [23]. Chen *et al.* also used PNIPAAm as the active material in a light-responsive reversible microactuator, which could be cycled from open to closed and back to open in 10 s when implemented into a valve. In this case a halogen lamp coupled with a fiber optic cable was used to heat the system directly, and a high irradiation intensity (30W) was required to achieve the rapid temperature induced phase transition in PNIPAAm [41]. Despite the fast open-close cycle achieved using this design, a high power bulb with an illumination spectrum from 400 to 2000 nm was required. Other material systems have also been explored. In one study, magnetic nanoparticles embedded in a wax irradiated with a laser showed a 12 ms actuator closing time in a valve, however the actuator control was irreversible, meaning that it could only be used one time [42]. In another study, it was shown that a high-intensity, bench-top 2 Watt pulsed laser could be used to generate

localized, high pressure vapors that expanded against a PDMS membrane, driving a reversible, 200 μs open-close cycle of a microvalve [43].

The practicality of incorporating a remotely activated actuator into microfluidic applications is limited by several main factors: the size of the energy source, actuation force, actuation reversibility, volume of the SRM, and time period of the open-close cycle. Upon critical review, the greatest challenges in making remotely stimulated microactuators realistic are in engineering a minimal time for complete displacement cycles of the actuator (i.e., to be on the order of milliseconds – in matching the performance of pneumatically driven actuators), and in reducing the size of the stimulation source.

Beyond microvalves, SRMs have also been integrated into mechanical actuators for applications such as microrobots for single cell handling [44], and for stroke treatments in the removal of thrombi using a photo activated shape memory polymer [45]. Miroactuators can also be found in optical guiding systems (commercial image projectors), colorimetric devices that change color as the diffraction grating changes [46], and in membranes [47]. These materials could be applied in a wide variety of applications.

1.3 Motivation

The goal of the work presented herein is in the design and fabrication of a microactuator device that is remotely actuated with the use of light. Essential to the microactuator is an active material that undergoes a significant change in volume upon a small change in temperature; namely photo sensing-transducing nanoparticles embedded in a temperature sensitive phase change polyethylene glycol (PEG) wax. To selectively and efficiently transduce optical energy into thermal energy, 10 nm gold nanoparticles (AuNPs) were added to the phase change wax in minute quantities (< 0.13 wt.%), and optically irradiated with a predetermined wavelength (532 nm). To prevent agglomeration of the NPs in the wax, they were first encapsulated in polyethylene-glycol diacrylate (PEGDA) microspheres. The optical and thermal properties of the composites (AuNP-PEGDA-PEG wax) were then characterized, with the goal of maximizing the deformation response while minimizing the deformation time period of the material. The active material was then integrated into a substrate and bound with a flexible membrane – the microactuator – and its mechanical properties were then finally characterized. A heat

transfer model was also constructed to simulate and predict actuation times if the device were to be scaled to a smaller size.

1.4 Outline

The body of the thesis, excluding the introduction, is divided into three chapters with Appendix A serving as a reference to calibration procedures, and program codes. Chapter 2 describes the material selection process, experimental design methods, and the synthesis and fabrication of stimulus response nanoparticle polymer composites. Chapter 3 presents the integration and fabrication of the synthesized SRM into a microactuator, and then describes the characterization of the device. Modeling of this actuator is also presented. The final chapter provides conclusive remarks on this work and offers insight for future work.

Chapter 2

Characterization of polymer nanoparticle composites

2.1 Introduction

This chapter focuses on the design, realization, and characterization of the polymer-nanoparticle composites that will be utilized to drive the microactuator described in Chapter 3. These composites are comprised of a polymer matrix, which is able to undergo a large volume expansion upon heating, and nanoparticle transducers, which couple light energy from a laser into thermal energy. Important criteria in the selection of these materials will be described, and characterization of the relevant properties of each component will be presented.

2.2 Stimulus-response material design considerations

Important design parameters in SRMs include the following: the ability to undergo many reversible cycles between the active and inactive states, a high degree of selectivity, high efficiency in energy transfers, a sufficient degree of response (i.e. change in volume), and ease of manufacturability. The preceding factors guided the engineering of a light-responsive material presented in this work, consisting of a nanoparticle-polymer composite. In this material, the sensing-transducing nanoparticles will absorb light with high optical selectivity from a predetermined wavelength of a laser stimulation source, and transduce it locally as heat to a phase-change polymer in which the nanoparticles are embedded. The heat will be transferred directly to the surrounding polymer material, driving the deformation (melting) of the polymer. Since the nanoheaters are dispersed homogeneously throughout the material volume, the heating is expected to be more uniform than in systems consisting of a phase change material on top of a planar heating element (which have been used in valves and pumps in microfluidic applications) and a quicker response and lower temperature gradients are expected to result. Results comparing volumetric to planar heat of a phase change wax will be shown in section 3.6.2. Subsequent sections in this chapter describe in detail the characterization of the nanoparticles and of the phase change polymer, the challenges of mixing and fixing nanoparticles within the phase change polymer, the laser stimulation source, and the thermal properties of the composites.

2.3 Phase change wax

In the microactuator, when the wax is heated above the melting temperature, the wax undergoes a phase change, which expands in volume and deforms a membrane. A host of phase change materials (PCMs) with a variety of characteristics are commercially available. The phase-change material used in our work was selected based on the following criteria:

- Significant volumetric expansion. This minimizes the amount of material required to achieve a particular height in the device, while maximizing the overall response.
- Low enthalpy of fusion. The less energy required to induce the phase change for a given heat generation from the NPs, the faster the deformation response of the polymer for a given power, and also the lower the energy required to induce phase transformation.
- Solid at room temperature with a temperature response (melting) in the range of 30-50 ºC. For actuators applied in microfluidic based applications, temperatures should not be too high so as to affect or degrade biochemicals or organisms in the device. Lower temperatures will also typically require lower power, and result in less ambient heating than at higher temperatures. The transition should take place above room temperature, so that heating rather than cooling can be utilized to drive the phase change.
- Chemically compatible with the nanoparticles. Whether the polymer should be hydrophilic or hydrophobic depends on the hydrophilicity of the nanoparticles to ensure miscibility upon mixing.

Given the aforementioned criteria for an ideal phase change material for actuators, three particular materials arise of interest – primarily due to their large volume expansions (5 to > 100%) at near room temperatures: paraffins, carbowax's, and hydrogels [31, 32, 36-39, 48]. Despite the unique properties of hydrogels, in particular PNIPAAm, they are dismissed as a candidate since their primary mechanism for swelling is based on hydration and dehydration kinetics, occurring on the order of minutes (of course, depending on sample size), which is far too long for practical actuators. Paraffin's and carbowax's are both linear polymer chains and have very similar enthalpies of fusion and volume expansion (5-30%) and are attractive since their expansion rate (or melting time) is only limited by the heat source that melts the wax. Paraffin waxes are classified as linear carbon chains with the formula C_nH_{2n+2} while carbowax's are linear ethylene glycol chains with the formula $H(OCH_2CH_2)_nOH$, known as polyethylene glycol (PEG). For each wax, an increase in chain length (n) results in an increase in melting temperature and an increase in the volume expansion. The primary

distinguishing feature is that paraffin is hydrophobic and PEG is hydrophilic. As will be discussed in section 2.4, nanoparticles in aqueous solution are used in our system; therefore PEG wax was selected to ensure miscibility of the two phases. The chain length (n), or molecular weight of PEG, and its corresponding melting point, was selected based on the fact that the device should not exceed biologically acceptable temperatures, therefore PEG with a number average molecular weight of Mn = 1100 g/mol, which melts in the range of 36 - 43 ºC, was selected.

2.3.1 Thermal and mechanical properties of phase change PEG Wax

In evaluating the total energy required to melt PEG wax (Mn 1100 g/mol) from room temperature, the heat of fusion (ΔH_m) and heat capacity (C_p) are the determining properties. As will be shown in Chapter 3, the heat of fusion and heat capacity of PEG wax are important determinants of the time required to melt a certain volume of PEG wax from room temperature for a given heat flow into the material. These properties were measured with a differential scanning calorimeter (DSC). An additional important property is the volume expansion coefficient (α) for PEG wax, which affects the maximum height that can be achieved by the actuator. This property was measured using a technique described below. All of the values measured here will be used in Chapter 3 in models describing the behavior of the actuator itself.

2.3.1.1 Measurement of the specific heat capacity and heat of fusion of PEG wax

The heat of fusion and temperature-dependent specific heat capacity of the PEG wax were measured using a DSC (Mettler Toledo-Star^e System, Ontario, Mississauga). The DSC was calibrated with pure indium and sapphire. A standard method used to evaluate ΔH_m and C_p was obtained from published resources [49]. Figure 2.1 shows a curve of thermal behavior of PEG wax with a 10 ºC/min heating rate. The onset melting temperature was determined by drawing a line tangent to the melting curve, corresponding to 32 ºC. Complete melting of PEG wax, determined in the same way, occurred at 43 ºC.

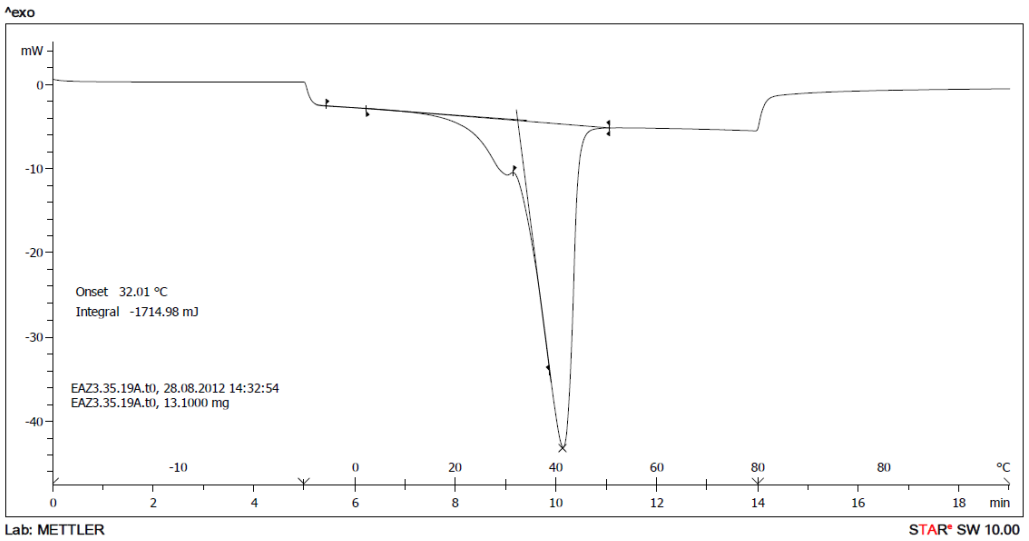

Figure 2.1: DSC temperature scan illustrating melting of PEG wax

The heat of fusion was determined by integrating the area under the curve over the melting range 32 ºC to 43 ºC in figure 2.1, with ΔH_m = 130.9 J/g. The heat of fusion measured here agrees well compared with reported values in literature for PEG wax, specifically for a higher molecular weight PEG (Mn = 1500 g/mol) the heat of fusion was measured as 164 J/g [50].

Evaluating the heat capacity as a function of temperature for PEG wax is not as trivial as the heat of fusion. In particular, the specific heat capacity as a function of temperature is calculated as the product of a calibration constant *E(T)* with the difference between heat flow of the sample $HF(T)_{sample+pan}$ and a blank pan $HF(T)_{pan}$, divided by the product of the sample mass m_{sample} and heating rate H_r, as shown in equations 2.1 and 2.2.

$$C_{p_{sample}}(T) = \frac{E(T) * \left(HF(T)_{sample+pan} - HF(T)_{pan}\right)}{H_r * m_{sample}} * 60_{s/min} \qquad 2.1$$

$$where, \quad E(T) = \frac{C_{p(sapphire)lit.}(T) * H_r * m_{sapphire}}{\left(HF(T)_{sapphire+pan} - HF(T)_{pan}\right) * 60_{s/min}} \qquad 2.2$$

In the above two equations, $Cp_{sample}(T)$ and $Cp_{(sapphire).lit}(T)$ are the specific heat of the sample and literature value of sapphire (provided as a chart) at a particular temperature, respectively. The calibration constant corrects for the difference in the heat capacity of sapphire measured with the DSC in our lab with well-characterized values of (TA Instruments) sapphire. The specific heat capacity as a function of temperature (fitted with

a 4th order polynomial) was determined over the temperature range 20.5 to 32 ºC from figure 2.1 with results presented in figure 2.2.

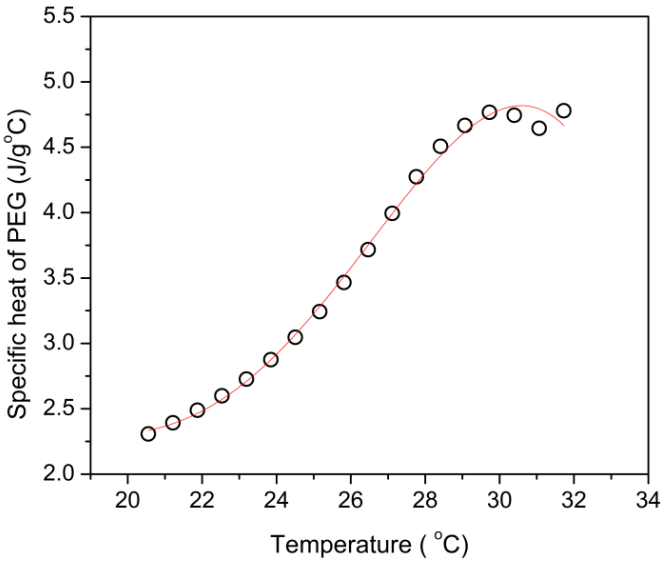

Figure 2.2: Specific heat capacity of PEG wax as a function of temperature

From room temperature to the onset of melting for PEG wax, the heat capacity ranged from 2.3 to 4.8 J/gºC.

2.3.1.2 Volume expansion of PEG wax

Determination of the volume expansion, α, for PEG wax was simply performed by measuring the difference in height Δh of PEG in the liquid state (h_1) to the solid state (h_2) (height was only measured since the area A was constant over the volume expansion range, $V_1 - V_2$), and dividing by the original height in the solid state, as shown in equation 2.3 and figure 2.3.

$$\alpha = \frac{\Delta V}{V_2} = \frac{\Delta h A}{h_2 A} \qquad 2.3$$

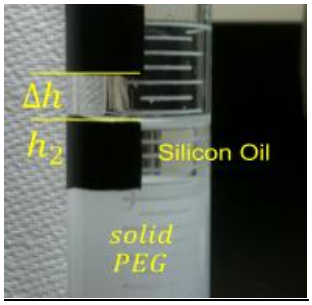

Figure 2.3: Volume expansion of PEG wax using a graduated cylinder.

A 20 g solid sample of PEG was placed in a graduated cylinder. Silicone oil was also added to set the height (h_1) to a visible marking above the volume of PEG in the graduated cylinder. The cylinder containing PEG was added to a water bath slightly above PEG's melting temperature. The hot water bath + PEG wax was cooled to room temperature in unison to ensure uniform axial shrinkage of PEG wax. This test was performed three times, and it was found that $\alpha = 0.075$.

2.4 Nanoparticle transducers

Metal nanoparticles have been widely demonstrated in many research applications as biological sensors due to their unique surface plasmon resonance phenomena and ease of surface modification [16, 51-54]. Surface plasmon resonance occurs when electrons in the nanoparticle collectively absorb energy from a particular wavelength of light, as described in chapter 1. The absorbed energy is dissipated by electron-electron and electron-ion scattering in a thermalization process. In sensing applications the thermal energy dissipating from nanoparticles has been considered as an undesirable side effect [14], however, more recently it is taken as an exploitable advantage in applications for mechanisms involving actuation [15]. Such modes of actuation include the rearrangement, construction, or degradation of molecules or molecular structures due to the thermal energy generated from the NPs embedded within the surrounding matrix or attached to the molecule. Some examples of heating of nanoparticles by surface plasmon resonance include photothermal therapy in cancer treatment by tissue degradation of tumorous cells [55], photothermal imaging of cells [56], and drug delivery by breakdown of temperature-sensitive materials [57]. Candidate nanoparticle materials that display surface plasmon resonance upon irradiation (transducing light energy to thermal energy) include gold, silver, copper, and other noble metals [16, 53].

Of particular interest is the energy efficency in the optical to thermal energy transfer of irradiated metal nanoparticles dispersed in a medium, as its value suggests whether or not heating by metal NPs is practical for particular applications and what metal is most efficient. In terms of a power-in/power-out efficiency in the energy transfer of incident optical power (P_i) to transduced thermal power (Q), and considering transmission and absorbance as the primary quantities (i.e., no reflection), equation 2.4 simply defines such an efficiency (Ƞ):

$$\eta = \frac{Q}{P_i - P_t} \tag{2.4}$$

where P_t is the transmitted optical power. Equation 2.4 can be rearranged and generalized in terms of absorbance of the material, A_λ (equation 2.5), which more precisely defines the effect of absorbance due to the presence of suspended particles. The absorbance is defined by Beer-Lambert's Law: $A_\lambda = \varepsilon_\lambda cl$, where ε_λ is the wavelength-dependent molar absorptivity, c is the molar concentration of absorbing particles, and l is the path length that light travels through the material.

$$\eta = \frac{Q}{P_i(1 - 10^{-A_\lambda})} \tag{2.5}$$

Under equation 2.5, the transduction efficiency for gold nanoparticles has been shown to be quite high, $0.8 < \eta < 1$ [17, 58], which was measured to be dependent on the irradiant power.

Due to their high transduction efficiency, gold nanoparticles were considered as an ideal candidate to be embedded in phase change PEG wax. Additionally, the commercial availability and lower relative cost to other noble metal nanoparticles, further substantiated the choice in using AuNPs. As described in Chapter 1 in figure 1.2, gold nanoparticles can be shaped or sized to selectively resonate with a particular optical wavelength. As a result, it was a matter of selecting a type of gold nanoparticle for a predetermined wavlength of light or vice versa. For the purpose of exploiting and experimenting with the thermal effects of irradiated embedded gold nanoparticles in polymer materials, and to study the feasabitlity of how such composites can act as a means for actuation, working with irradiation sources in the visible spectrum (opposed to UV and IR) simplifies the overall instrumentation and design, and lowers the cost. Green lasers (532 nm) are low cost and commercially abundant. Therefore, under a preselected

532 nm laser source, 10 nm spherical gold nanoparticles that resonate at 522 nm were judged to be most suitable for this application.

2.5 Nanoparticle-wax composites

With PEG wax (Mn 1100 g/mol), 10 nm gold nanoparticles and a 532 nm irradiation source selected to form a AuNP-wax composite that was theoretically capable of undergoing a phase change under optical irradiation, a mixture of PEG wax and gold nanoparticles were blended at various ratios for the purpose of assessing the chemical and physical feasibility of such a composite immediately after formation and after a few heating and cooling cycles.

Composites were formed using the following method. To achieve a suitably high concentration of NPs in the polymer, a concentrate of AuNPs was formed from a native gold nanoparticle solution (citrate-capped 10 nm AuNPs in water, 60 ug/mL, Sigma Aldrich #741957) before adding the particles to the polymer. To form the concentrate, eight vials were filled with 1 mL each of the native AuNP solution. The vials were centrifuged (Eppendorf 5415D) for 20 minutes at 15000 rpm. The supernatant was removed from each vial. The AuNP concentrate was then added into a single vial from all the eight vials achieving a final concentration of 1.9 mg/mL AuNPs in solution. To test the viability of the AuNP-PEG composite, different ratios of AuNPs to PEG wax were prepared, table 2.1. Each vial was agitated above 43 ºC in a vortex mixer until a homogenous mixture formed.

The appearance of the samples after mixing suggested that the composites were poorly dispersed. Samples 2 to 4 turned to a purplish color after 5 minutes of mixing, indicating that the particles were agglomerating, while sample 5 turned to a light purple/red color immediately upon mixing and completely purple after 5 minutes. Additionally, even for lower concentration samples that maintained their red appearance after mixing, once these samples were exposed to one cooling and heating cycle, agglomeration (purple-blackish) was evident, as summarized in table 2.1. Agglomeration is undesirable as it leads to insufficient absorption of light at the predetermined irradiant wavelength.

Sample	AuNPconc (µL)/PEG(µL)	Stability of 10 nm AuNPs in PEG wax			
		Initial mixing	5 minutes after mixing	(cool-heat)×1	(cool-heat)×3
1	0.1	YES	YES	YES	NO
2	0.3	YES	YES	YES-NO	NO
3	0.71	YES	YES-NO	NO	NO
4	1	YES	NO	NO	NO
5	1.5	NO	NO	NO	NO

Table 2.1: Qualitative chart representing the stability of gold nanoparticles mixed with PEG wax at various volume ratios. A value of 'NO' is entered if agglomeration (change of color to dark purple/black) had occurred upon mixing the two materials, a value of 'YES' (remained red in color) indicates that the particles are stable, while a value of 'YES-NO' indicated partial stability (color of dark red/purple).

The optical properties of the composites before and after heating were further characterized using a Perkin-Elmer Lambda 900 UV/Vis/NIR spectrophotometer, figure 2.4. The optical absorbance spectra of the composite with 0.123 wt % AuNPs in PEG wax (corresponding to sample 3 in chart 2.1) was recorded both for samples mixed after 5 minutes, and for samples that were completely mixed and had undergone two heating and cooling cycles to 45 ºC and 25 ºC, respectively. All spectra were recorded over the range of 400 to 800 nm, with an optical resolution of 1 nm. To prepare the samples for characterization, liquid and liquid-solid mixtures of the composites were placed in custom molds comprised of two sandwiched glass slides coupled together with adhesive tape. The adhesive tape was initially cut out to provide a reservoir of constant thickness and size into which the mixtures could be placed. Samples were then mounted in the beam path.

Agglomeration of the gold nanoparticles embedded in the PEG wax is evident from both the broadening of the absorbance peak and the overall decrease in absorbance (figure 2.4, peaks a – c). It was also visually evident that the red colored AuNP solution turned purple upon mixing with molten PEG wax followed by two heat-cool cycles, which corresponds to the undesirable degradation of the surface plasmon resonance property at 532 nm.

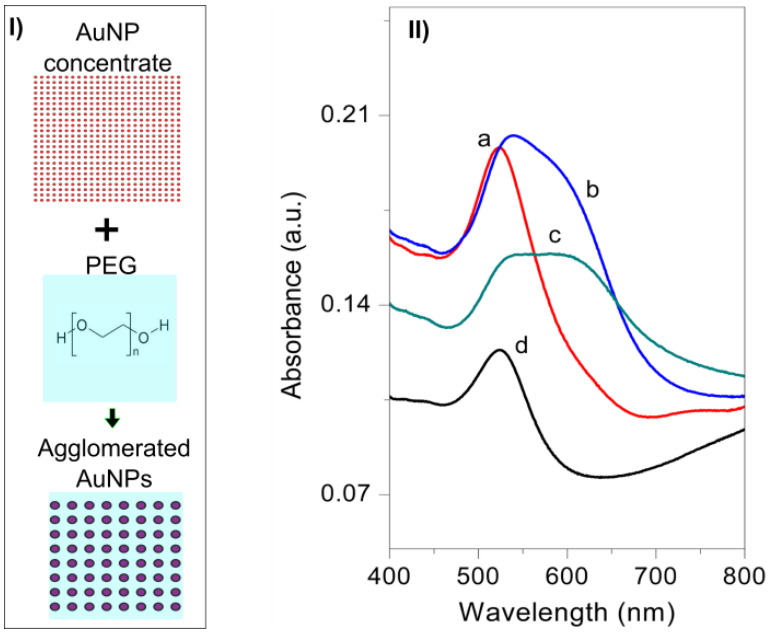

Figure 2.4: Agglomeration results after mixing gold nanoparticles with PEG wax. I) Drawing of AuNP concentrate mixed with PEG wax, and the agglomeration that results. II) AuNP-PEG UV-Vis spectra, in absorbance units (a.u.). When AuNPs are mixed with PEG wax directly, the absorption peak shifts from 'a' (AuNP concentrate + water) and gradually widens and decreases in intensity to peak 'b' (AuNP concentrate + PEG wax after 5 minutes of mixing). After subsequent heating cycles the peak broadens further from 'b' to 'c'. Curve'd' is a native concentration of AuNPs provided directly from Sigma Aldrich.

The occurrence of agglomeration or phase separation when nanoparticles are mixed with various media is reported as a common problem in nanoparticle-polymer synthesis [59]. In our case, agglomeration of gold nanoparticles is undesirable since the absorbance peak would be shifting and decreasing, which lowers the transduction efficiency at a given wavelength, and reduces the reversibility of the actuation mechanism. To overcome the issue of agglomeration, AuNPs were rigidly encapsulated in a compatible polymer matrix in the form of micrometer sized particles. The particles were then dispersed in PEG wax, which successfully endured many reversible heating and cooling cycles without any sign of nanoparticle agglomeration, as described below.

2.6 Nanoparticle-polymer microsphere composites

As described above, the initial synthesis of homogeneously dispersed aqueous-based 10 nm gold nanoparticles in PEG wax – via direct mixing of the two materials – proved unsuccessful due to agglomeration, an alternative solution was necessary (and briefly mentioned above) in dispersing AuNPs throughout PEG wax. To prevent agglomeration from occurring, AuNPs were encapsulated in a crosslinked polymer in the form of monodisperse (equally sized) microspheres, which could then be dispersed in PEG wax.

The crosslinked polymer would prevent the NPs from agglomerating during heating and cooling. Small monodispersed microspheres of the composites were an attractive geometry since they could be easily handled during characterization (due to a single shape and size), and instead of nanoheaters dispersed throughout PEG they would still provide localized heating as microheaters. It was then a matter of selecting a monomer which could form crosslinks – effectively encapsulating and fixing NPs in a rigid network, while maintaining stability of gold nanoparticles (preventing agglomeration) prior to polymerization to ensure the resonance properties of AuNPs was retained throughout the preparation steps. Gold nanoparticles were therefore encapsulated in polyethylene-glycol diacrylate (PEGDA), a hydrogel material which can be photo-crosslinked in the presence of a suitable initiator to form a stable network. Like the PEG wax itself, this material is based on poly(ethylene-glycol), and it is expected to have good miscibility with the wax matrix.

2.6.1 Synthesis of Microspheres

AuNP-polymer microspheres were fabricated using a microfluidic device to form droplets of Au-loaded spheres that could be crosslinked. To form the monomer solution from which the microparticles were made, eight centrifuge vials were separately filled with 1 mL of native Au NP solution. The vials were centrifuged for 20 minutes at 15000 rpm. The supernatant was removed from each vial. The AuNP concentrate was then added into a single vial from all the eight vials. Then 200 µL of PEGDA (monomer, Sigma Aldrich), containing ~ 1.9 wt % 2,2-dimethoxy-2-phenylacetophenone (photoinitiator, Sigma Aldrich), was homogeneously combined in a vortex mixer with 60 µL of the AuNP concentrate. The concentration of the photoinitiator (1.9 wt%) was selected because this was the minimum concentration at which polymerization would occur for microspheres for a particular UV illumination intensity. It is interesting to note that for a non-microsphere composite made of large disks (5 mm diameter, 1 mm thick), a far lower weight percent of the photoinitiator is required to induce polymerization. The difference may be caused by several factors: reflected light by the high surface area of all microspheres which reduces the penetration of light throughout the microsphere volume, absorbance of the surfactant used in the manufacture of microspheres, or insufficient quantity of photoinitiating molecules when present in individual microspheres, which may explain the higher intensity used.

A microfluidic device was utilized to manufacture the microspheres; complete details into the physics of monodisperse droplet formation can be found elsewhere [60]. The fabrication of the device itself is summarized in section A.2. The microsphere-producing device consists of microchannels where two chemically distinct fluids (aqueous and organic) are transported to meet at a junction, specifically a nozzle. Fluid in the aqueous phase is 'pinched' into the continuous organic phase where liquid microspheres (droplets) emerge at the outlet. Subsequently, these liquid microspheres travel with the continuous phase out of the microchannel and into tubing, where the two fluid phases drip into a petri dish. As a macroscale droplet falls into the petri dish it is irradiated with UV light, which photopolymerizes the liquid microspheres to solid ones. This process is illustrated in figure 2.5.

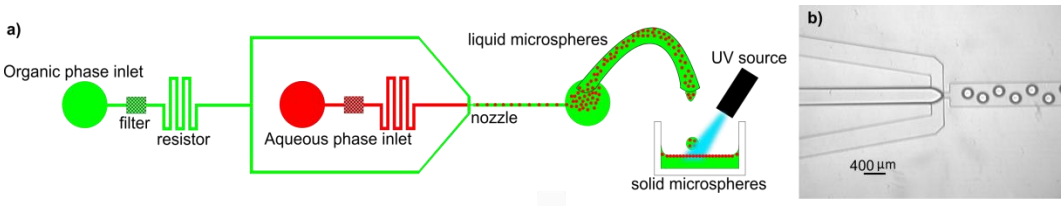

Figure 2.5: Illustration of the microdroplet generator. (a) The organic phase (green) is filtered, passed through a resistor (removes flow instabilities originating from the syringe pump), and split into two streams, between which an aqueous phase (red) is introduced. Both phases are driven using syringe pumps. The streams are fed through a nozzle, and due to immiscibility of the liquids, droplets of aqueous-phase fluid form in the device outlet channel. These droplets are dispensed into a dish in which they are photopolymerized through irradiation with UV light. (b) Optical image of the nozzle, depicting the emerging microspheres.

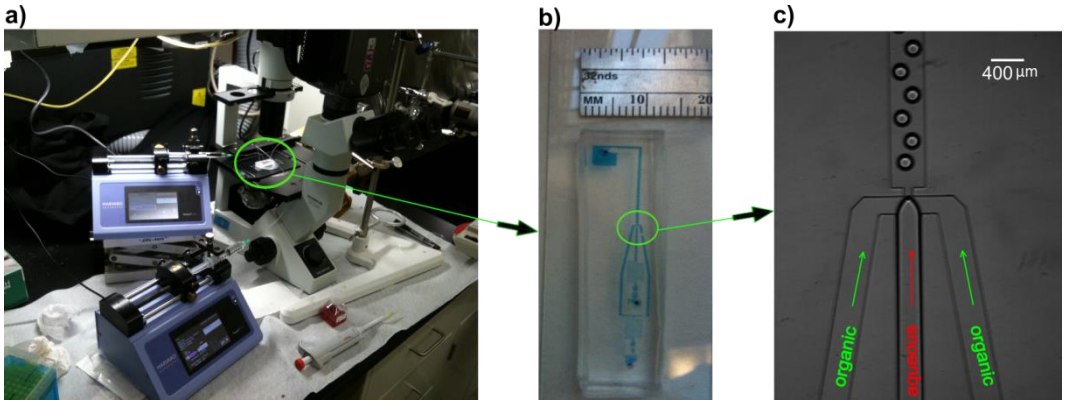

Figure 2.6: Photo of a microfluidic device generating microdroplets. (a) Lab set-up required to fabricate devices. (b) Optical image of a device, shown with dye for contrast. (c) Microscope image depicting the combination of the three streams to form microspheres.

In figure 2.6 two syringe pumps independently control the aqueous and organic phase at specific flow rates to yield a certain droplet size and rate of production. Note the blue dye in the microchannel, which depicts its geometry. The droplets emerging at the

outlet are directed off-chip through a tube into a petri-dish, where they are subsequently photopolymerized with UV light directed through a fiber optic cable.

The AuNP-PEGDA solution (aqueous phase) was added to a 1 mL syringe, and the perfluorocarbon with surfactant [61] in another syringe. The two syringes were connected to their respective inlets using BD Intramedic tubing. Using the digital syringe pump, the flow rate in the continuous phase was set to 30 µL/min and the aqueous phase to 20 µL/min. These flow rates were experimentally determined to yield steady production of microspheres. In the first few minutes, microdroplets were dispensed into a separate petri-dish. Once the droplets stabilized, a new petri-dish with a small amount of perfluorocarbon was positioned to receive the droplets. The UV source (LC8 lightning Cure, Hamamatsu) was aligned to irradiate a point on the petri-dish from which the droplets would fall onto the perfluorocarbon surface. The intensity of the UV source was set to 0.9 mW/cm^2, and was sufficient to crosslink the PEGDA monomer to form polymer microspheres. The size of the microspheres was governed by the width of the nozzle outlet and the ratio of the aqueous to continuous flow rate. Our flow rate yielded spheres with a diameter of 130 um, as determined by optical microscopy, figure 2.7.

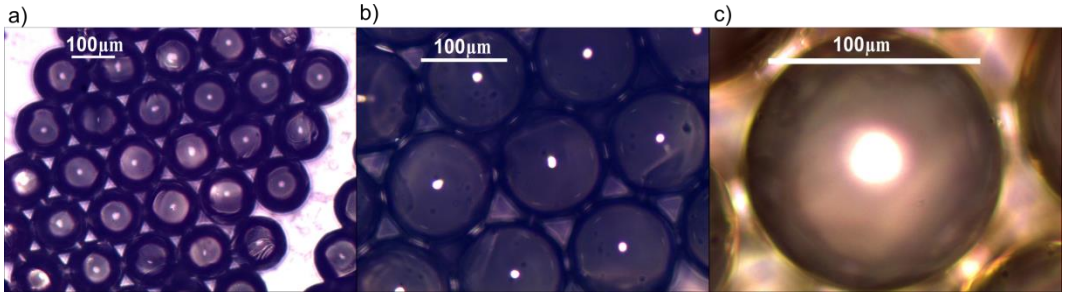

Figure 2.7: Micrographs of monodisperse AuNP-PEGDA microspheres with a diameter of 130 µm. a) 100X magnification. b) 300X. c) 500X

UV-VIS spectra were collected for AuNP-PEGDA microspheres in PEG wax, immediately after preparation, and after several heating and cooling cycles. It is shown in figure 2.8(II) that the absorbance spectrum of the AuNP-PEGDA microspheres (0.123 wt% AuNPs) is virtually identical to that of AuNP spheres in water, indicating that the AuNPs have been crosslinked into the PEGDA in a well-dispersed state. Furthermore, when the AuNP-PEGDA microspheres were added to PEG wax and subjected to several heating and cooling cycles, the peak position remains unchanged (curve b), indicating a robust polymer-nanoparticle composite with good thermal stability.

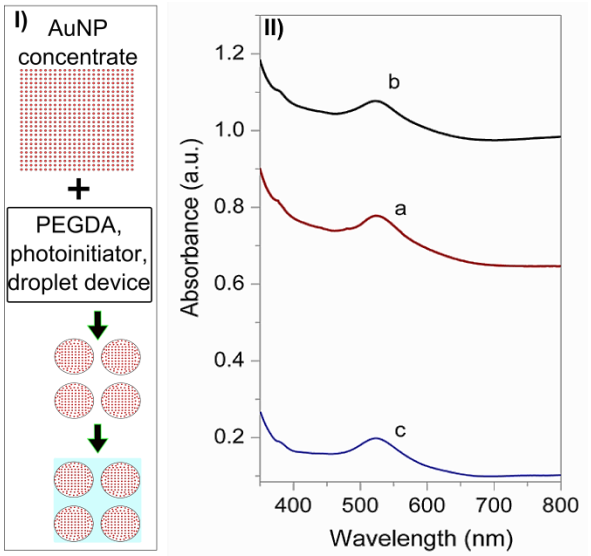

Figure 2.8: Results of mixing gold nanoparticle-polymer microspheres with PEG wax. I) Drawing showing how the gold nanoparticles embedded in solid microspheres are fixed in their original form even after mixing with PEG wax. II) Neat Au NP-PEGDA microspheres (0.123 wt% Au NPs) (a), and Au NP-PEGDA microspheres which have been mixed with PEG wax and subjected to two heating and cooling cycles (b) show very similar absorption spectra. Also for comparison, curve 'c' illustrates a concentrated gold nanoparticle solution in water (0.123 wt% AuN Ps).

Differences in absorption are seen between curves (a) and (b), and are attributed to the opacity of PEG wax. Nonetheless, the overall shape and location of the absorption peaks are very similar, indicating that the AuNPs do not agglomerate, even upon heating.

2.7 Thermal characterization of the nanoparticle-polymer microspheres

This section describes the characterization of several thermal properties of the photo-responsive AuNP-PEGDA microspheres. The thermal properties of interest included the temperature and heat flow response of the composite upon irradiation with a laser, and the specific heat capacity.

2.7.1 Temperature response of the monodisperse microspheres

It was of primary interest to determine if the photo-responsive microspheres embedded in PEG wax could be used to drive its phase transition from solid to liquid, therefore it was necessary to determine the maximum temperature that could be reached by the microspheres as a function of nanoparticle concentration and irradiation intensity.

The temperature measurement of the AuNP-PEGDA microspheres (*without* PEG wax) utilized a calibrated IR camera (SC300-series, FLIR, Burlington, Ontario), as shown

in figure 2.9. The calibration steps of the IR camera and emissivity value of the material under measurement are described in section A.1. The benefit in using an IR camera over a thermocouple in contact with the microspheres under irradiation is that the IR camera does not transduce energy from the laser, whereas a thermocouple does, which minimizes the complexity in post analysis of the data (i.e. subtracting the effect of transduction from the thermocouple).

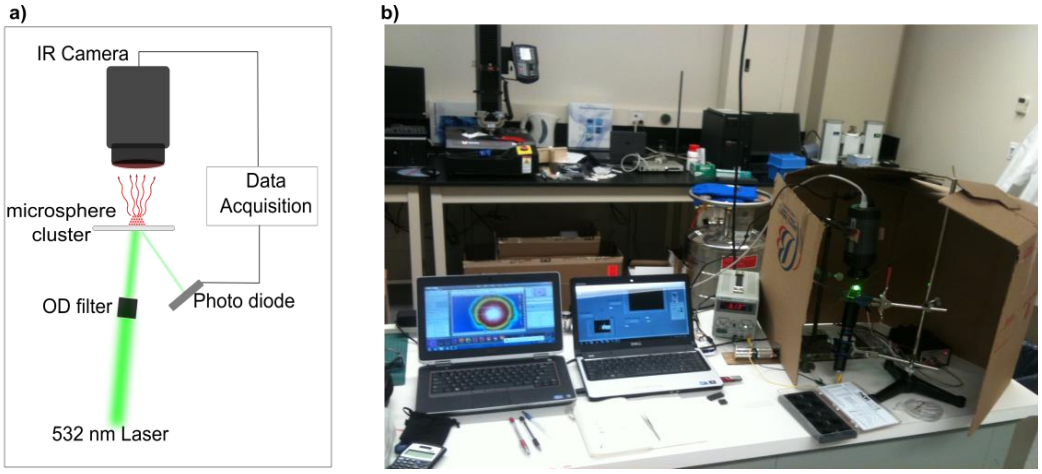

Figure 2.9: Temperature measurement using the IR camera and 532 nm laser. (a) Schematic of the set-up, (b) Photo of the set-up.

The temperature measurement setup consists of two sensors: the IR camera and photodiode. The photodiode (Thor Labs, FDS 1010) was connected to a data acquisition module (NI USB 6009), with calibration details in section A.1.2, and provided in situ feedback of the irradiation power on the sample. In all measurements, the 72 mW laser (532 nm Aries series, Laser Glow Technologies, Ontario, Toronto) was positioned 10 cm below the glass slide which served both as a beam splitter and support for the microsphere cluster under irradiation. The glass slide supporting the sample was tilted slightly so that the reflected beam was incident on the photodiode while the transmitted beam interacted with the sample. Measurement of the reflected beam power was necessary since it enabled calculation of incident power on the sample. The fraction of light reflected from the glass slide to the photodiode was measured as 0.04. To determine irradiant power, the incident beams power value was therefore multiplied by (1-0.04). Intercepting the beam path between the laser and glass slide were optical density filters (Absorptive Neutral Density Filters – NEK01, Thor Labs, Newton, New Jersey), which enabled controlled attenuations of the irradiant intensity on the sample. It is important to

note that in all irradiation measurements, temperature values were measured only once a steady state temperature was achieved.

2.7.1.1 Sample preparation of microsphere clusters for temperature measurements

Monodisperse microspheres (0.123 wt% AuNPs in PEGDA) in an ethanol mixture were dispensed from a pipette on a glass slide in such a way so that a cluster of randomly packed microspheres were formed no larger than the laser beam diameter ($m = 0.8 \pm 0.2$ mg). The cluster was then air dried until all ethanol evaporated. The sample on the glass slide was aligned in the x-y plane with the laser beam axis to yield the maximum observed temperature

2.7.1.2 Temperature response results of microsphere clusters under irradiation

The primary objective of the temperature measurement of microsphere clusters was to explore how the temperature changed when both the concentration of AuNPs in PEGDA and irradiation power were varied independently. The first set of measurements involved the determination of the maximum temperature microsphere clusters at different AuNP loading concentrations could reach for a fixed irradiation power, beam diameter, and sample size. The second set of measurements involved varying the irradiant power for a fixed loading concentration of AuNPs.

Constant laser power and change in AuNP loading concentration:

In the first set of temperature measurements, in which the NP concentration was varied while the laser intensity was kept constant, the measured temperature increased with increasing concentration, as shown in figure 2.10. Beyond a certain concentration (0.023 wt% AuNPs) no further increase in temperature occurred as the concentration was increased.

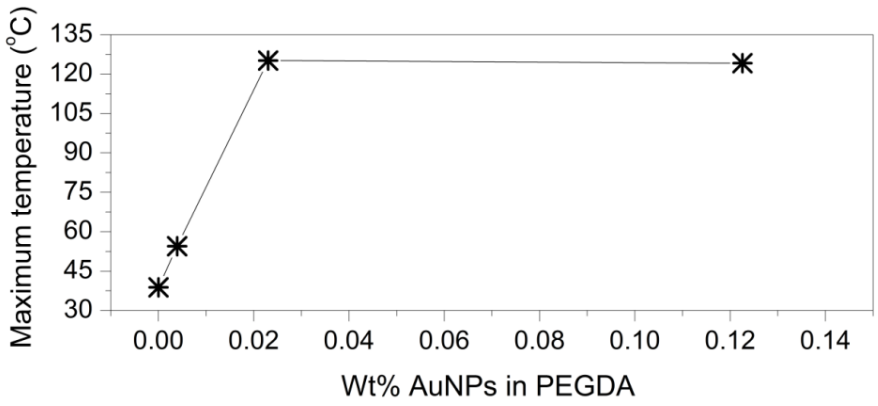

Figure 2.10: The effect of gold nanoparticle concentration on observed temperature of irradiated (69 mW) microsphere composites. The line connecting the points is included to guide the eye.

While irradiating AuNP microsphere clusters at constant laser power (69 mW) and measuring the corresponding temperature, several features of the composite were determined: (1) As quite high temperatures were reached (125 ºC), it was expected that the temperature generated by the AuNP-polymer microspheres would be sufficient to melt PEG wax (which has a peak melting point of 43 ºC) to achieve a remotely-actuated composite, provided that the concentration of the microspheres within the wax was sufficiently high, (2) As the concentration of AuNPs in PEGDA micropsheres is increased, an upper absorption limit is reached, as indicated by a maximum temperature.

Constant AuNP loading concentration with changes in irradiant laser power:

In the second set of temperature measurements, the irradiant power incident on a microsphere cluster (concentration of 0.123 wt% AuNPs, mass = 0.6 mg) was varied. The purpose of this measurement was to explore how temperature and irradiant power are related, that is, to determine if the relationship between these variables was linear.

The temperature of the sample was measured under various irradiation powers using the same 72 mW laser with appropriate optical density filters to attenuate the laser power. Again, the power incident on the sample was determined by calculating the fraction of light incident on the photodiode. Upon irradiation of the sample volume with the laser at various attenuations, its center was measured as the hottest region, as shown in a thermograph in figure 2.11(a), and at various irradiant powers, shown in figure 2.11(b).

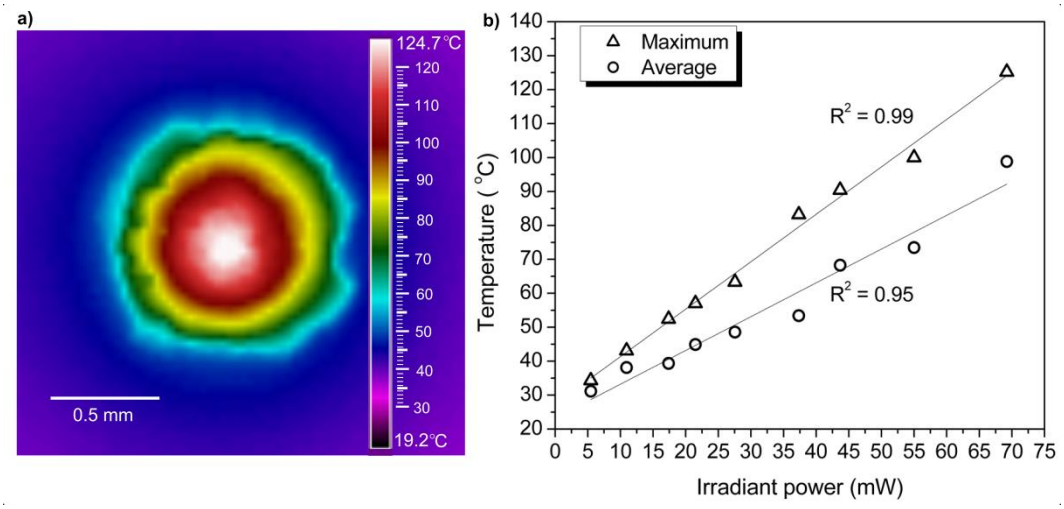

Figure 2.11: Average and maximum temperature of a microsphere cluster at 0.123 wt% under various irradiant powers. a) IR camera image depicting the temperature profile of a cluster of microspheres under irradiation. b) Plot of peak and average temperatures measured from a microsphere cluster as a function of the irradiant power of the laser. Higher irradiant power results in higher peak and average temperatures.

The temperature response in figure 2.11(a) at various irradiant powers displays a linear relationship, which indicates constant transduction efficiency over the irradiant power range. Additionally, the linear response indicates that the temperature could increase even further with greater irradiant powers.

The average temperature of the sample was also determined, figure 2.11(b). The purpose in determining an average temperature is that it more accurately represents the temperature for the given sample mass, which becomes important when developing a lumped capacitance heat flow model as described in Chapter 3. The average temperature was determined by converting the image in figure 2.11(a) to a greyscale followed by determining the intensity distribution across the sample width. This curve was then fitted with a Gaussian distribution, as shown in equation 2.5., with the fitted curve shown in figure 2.12.

$$f(x) = \frac{\int_{x1}^{x2} Ae^{\left(-\frac{\left(\frac{x-x_c}{w}\right)^2}{2}\right)} dx}{x_2 - x_1} \qquad 2.5$$

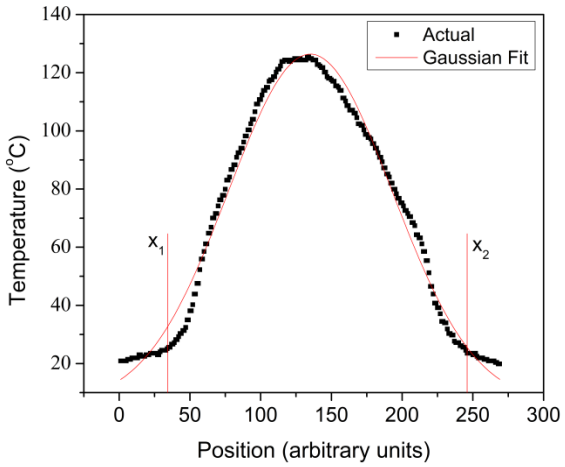

Figure 2.12: Temperature distribution across width of microsphere cluster and Gaussian fit.

Where *f(x)* is the distribution as a function of location *x*, *A* is a constant, *w* is the width and x_c is the peak center. From this equation, two parameters were extracted, namely *w* and x_c The average temperature (T_{avg}) was then determined by taking the area under the curve over the range that specifies the width of the sample mass, as shown in equation 2.6.

$$T_{avg}\ (°C) = \frac{\int_{x1}^{x2} T_o + (T_{max} - T_o) e^{\left(-\frac{\left(\frac{x-x_c}{w}\right)^2}{2}\right)} dx}{x_2 - x_1} \qquad 2.6$$

The value T_o is the temperature of the plate supporting the sample at constant room temperature and T_{max} is the maximum temperature in the distribution. The quantity (x_2-x_1) represents the diameter of the sample, since the integration is taken over the sample mass only. The reason for fitting a Gaussian distribution is due to the precision of the function, with an average R^2 value of 0.991 for all the different irradiation intensities. As mentioned above, the average temperature provides a more accurate measure of temperature per unit mass under irradiation. When relating temperature to heat flow, via the lumped capacitance method described in Chapter 3, the mass corresponding to the average temperature more accurately links the two properties.

2.7.2 Heat flow response of the monodisperse microspheres

In the second technique, the heat flow of the AuNP-PEGDA microspheres during optical irradiation was measured using a photo-differential scanning calorimeter (photo-DSC,

Mettler Toledo-Star^{e} System, Ontario, Mississauga). This tool consists of a differential scanning calorimeter coupled to a UV lamp through a light pipe, and is able to measure heat flows from small sample masses with high sensitivity. The heat flow as a function of both irradiant power and AuNP loading concentration was measured. Additionally, the transduction efficiency of AuNP-PEGDA microspheres could be determined, providing evaluation in the performance of electromagnetic to thermal energy transfer of the composite. This device can also be used as a regular DSC in ambient lighting.

2.7.2.1 Heat flow measurement details and sample preparation for irradiated microsphere clusters

To measure the heat flow from irradiated microspheres, the photo-DSC and microsphere samples were first prepared. The photo-DSC was configured to isothermal mode, maintaining a stable temperature of 25 °C during all irradiation measurements. Monodisperse microspheres in an ethanol mixture were dispensed from a pipette into a photo-DSC compatible aluminum pan (5.5 mm in diameter) in such a way so that a cluster of randomly packed microspheres were tightly formed. The cluster was then air dried until all the ethanol evaporated. The sample pan was then placed on the sample-sensor in the photo-DSC. A blank aluminum pan was then placed on the reference-sensor. Irradiation was only on the sample pan (not the reference pan); hence in this arrangement the photo-DSC measures the sum of heat flow from the sample and the pan. It is important to note that four temperature scans were performed on each sample in all subsequent measurements, with the first as a conditioning run and the other three as measurements, which concluded high precision data values with a standard deviation less than 1%.

To determining power density as a function of irradiant power, corrective measures are of primary importance for accurate transduction results. For instance, it is necessary to subtract the quantity of heat transduced by the pan to determine a true sample heat flow, since the photo-DSC measures the sum of heat flow from the transduction of light with the microsphere sample and pan. Additionally, due to differences in transmission that occur between samples at different concentrations, the energy transduced *by the pan* itself is different for each AuNP concentration in PEGDA, which also needs to be taken into account. The power that the pan transduces is proportional to the intensity of light that transmits through the sample for a particular concentration of AuNPs in PEGDA. When more AuNPs are in the PEGDA matrix, more light energy is absorbed in the microspheres, and less is transmitted through the sample to

transduce with the pan. To determine the heat flow from the microsphere sample alone, the quantity of heat transduced by the pan is subtracted from the photo-DSC measurement value representing the sum of heat flows. To determine the contribution from the heat flow, it is first necessary to determine the intensity of incident light reaching the pan at each concentration. The irradiant power drop across each different AuNP concentration in PEGDA microspheres was measured by irradiating the sample from the laser source (*Pi*) with a photodiode collecting the reflected beam (*Pr*) and another photodiode collecting the transmitted beam (*Pt*), figure 2.13 and equations 2.7 to 2.9.

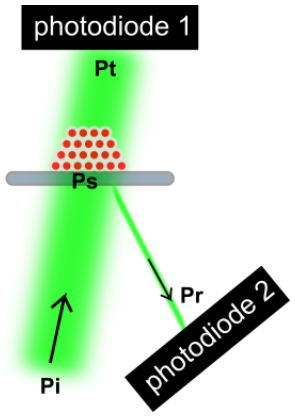

Figure 2.13: Schematic illustrating measurement setup for fraction of light transmitted through microsphere cluster

$$P_i = \frac{P_r}{0.04} \quad 2.7$$

$$P_s = P_i * (1 - 0.04) \quad 2.8$$

$$T = \frac{P_t}{P_s} \quad 2.9$$

The results are summarized in table 2.1. As expected, the transmission of light through the sample decreases with increasing concentration of nanoparticles, as a higher concentration of NPs absorbs more light from the laser source.

Wt% AuNPs	0	0.004	0.023	0.123
T	0.38	0.36	0.33	0.11

Table 2.2: Fraction of light transmitted through various concentrations of AuNPs in microsphere clusters

To determine the total amount of energy absorbed at a given intensity, it was also necessary to determine how much heat was actually absorbed by the pan at a given intensity. These values were measured by the photo-DSC by irradiating blank aluminum pans at different intensities. The results are shown in figure 2.14.

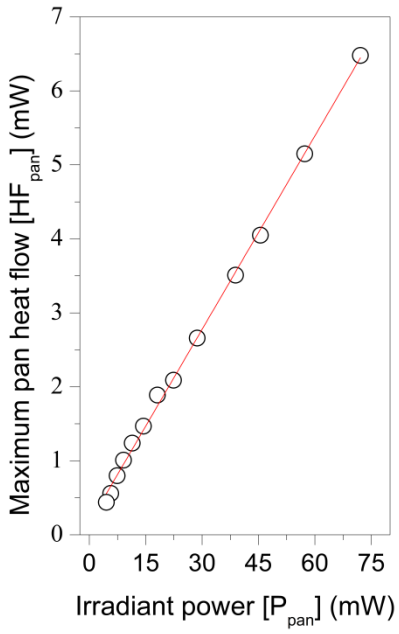

Figure 2.14: Heat flow transduced by empty DSC aluminum pan at various irradiation powers.

The heat flow from the pan followed the linear relationship [$HF_{pan}(mW) = [S_{pan}(mW)]\ P_{pan} + a_{pan}$] (figure 2.14), where P_{pan} is the irradiant power on the pan, (S_{pan}) is the slope and (a_{pan}) is the y-axis intercept.

To determine the fraction of the light absorbed by the pan at a given concentration of nanospheres (and to correct for this contribution), the power transduced by the pan was determined by the product of the fraction of transmitted light (T) and the power irradiant on the sample (P_s). This calculated heat flow transduced by the pan was finally subtracted from the original heat flow to obtain the heat flow exclusive to the microsphere cluster. The corrected heat flow ($HF_{corr.}$) could then be calculated according to equation 2.10.

$$HF_{corr.} = HF_{DSC} - HF_{pan} = HF_{DSC} - (S_{pan} * P_s * T - a_{pan}) \qquad 2.10$$

The linear equation from figure 2.14 was used to determine how much the pan transduces for a particular concentration corresponding to a particular incident power.

As an example, the effect of subtracting pan heat flow from the combined heat flow (i.e., corrected heat flow) for a sample containing 0.023 wt% AuNPs irradiated at 69 mW is shown in figure 2.15.

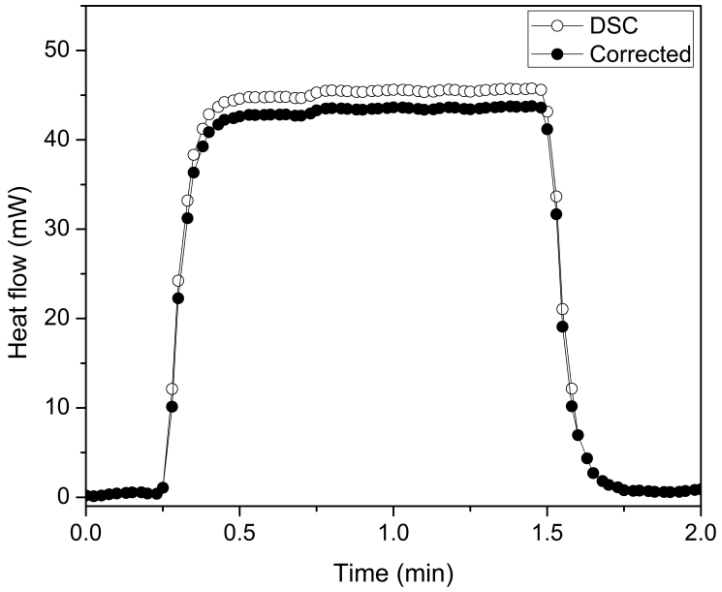

Figure 2.15: Subtracting the effect of transduction by an aluminum pan from transduction by the combined aluminum pan + microsphere sample. 'DSC' curve represents the sum of heat flow of the microsphere sample plus the pan while the 'Corrected' curve represents the subtraction of transduction by the pan from the DSC curve.

In figure 2.15 the quantity transduced by the pan is small as seen in the minor shift in heat flow from the DSC curve to the corrected curve. As the AuNPs are enriched to higher concentrations in PEGDA microspheres, the effect of transduction by the pan becomes less pronounced, a result due primarily to the fraction of light transmission decreasing in samples of increasing AuNP concentration as seen in chart 2.2.

This correction was performed throughout the measurements.

2.7.2.2 Power density and transduction efficiency of AuNP-PEGDA microspheres

With the effect of pan transduction subtracted, the power density of each sample was determined by dividing the corrected transduced thermal power measured by the sample mass, and the irradiant flux was calculated by the irradiant power divided by the laser beam area (0.00785 cm^2). As was shown in figure 2.15, an initial transient period is present followed by a steady-state heat flow period, which applied to all irradiated

samples with each showing different response times; as a result, heat flow values to determine power density were obtained from the steady state period for each sample under irradiation. The power density as a function of irradiant power at various AuNP loading concentration is shown in figure 2.16. The heat flow results are plotted in metrics of power density (W/g) versus irradiant flux (W/cm^2).

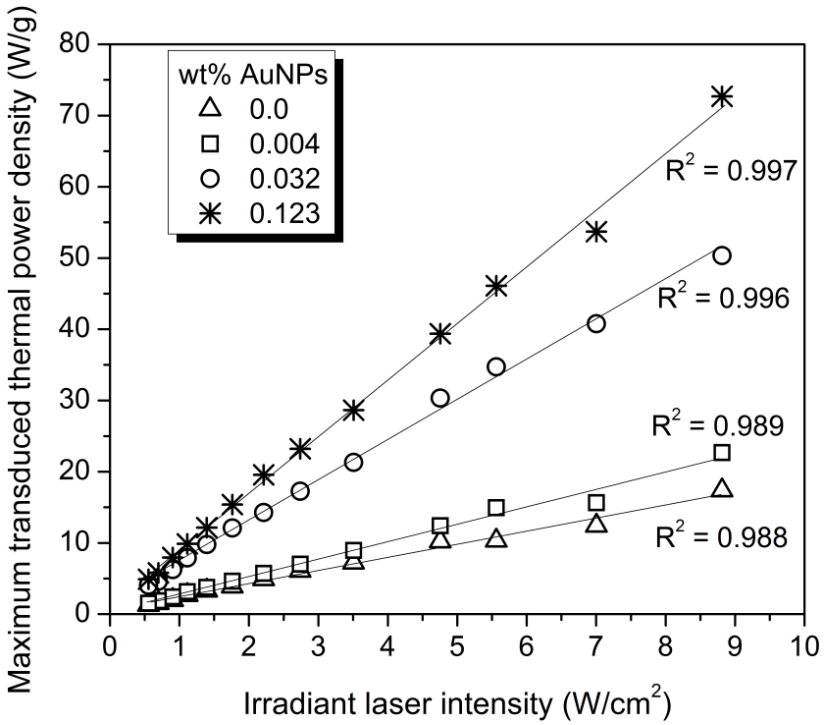

Figure 2.16: Power density versus irradiant flux for various AuNP loading concentrations in PEGDA

The heat flow results in figure 2.16 show the heat transduced primarily due to the microspheres; the transduced heat flow from the pan supporting the microspheres was subtracted for each measurement. As expected, even the neat polymer (0 wt% NPs) was able to absorb some heat from the beam, however increasing the concentration of AuNPs led to increased power density within the sample. It is observed that the heat flow follows a linear relationship in response to the irradiant power, with higher irradiation intensities resulting in higher amounts of heat absorbed per unit mass. Furthermore, these curves indicate that the transduction can be extended with even higher irradiant power. However, it was desirable in our system to utilize higher concentrations of nanoparticles with lower intensities of light (rather than lower concentrations with higher intensities) to prevent non-localized heating of the surrounding elements in the system.

The average transduction efficiency [η, i.e. the fraction of input power (P_i - P_t) transduced to heat (Q)] can be calculated from figure 2.16 by taking the slope and multiplying by the sample mass and dividing by the laser beam area, which is equivalent to equation 2.4. The result of this calculation for the 0.123 and 0.023 wt% AuNP-polymer microsphere samples, is η = 70 ± 3% and η = 75 ± 6%, respectively. This transduction efficiency is comparable with our previous thermal analysis study on low power irradiation of gold nanoparticles in a polymer (PEGDA) matrix, with 80 % TE under 3.1 mW irradiation power. As an important point to make note of, the heat transduced by the microsphere sample (Q, as shown in equation 2.4) is measured by the photo-DSC. In reality a small fraction of heat is lost to the surroundings (Q_{loss}) despite the DSC having superior sensitivity, which is ultimately the result of a temperature gradient between the sample and the isothermal background temperature at 25 ºC. In the foregoing calculated transduction efficiencies, it is assumed no heat is lost to the surrounding air. If this loss was taken into account, the transduction efficiency would slightly increase. Overall, the 0.123 wt% sample would be preferable for use in a device because it has the highest power density compared to all other concentrations.

In summary, measurement of the maximum and average temperature of the AuNP microspheres under optical irradiation demonstrated that the temperature achieved in a microsphere under irradiation would be sufficient to locally melt PEG wax in its surroundings. Due to the variable amount of microspheres added to the reservoir of the actuator (as seen in Chapter 3), knowing the power density (in addition to the heat capacity, described below) for a given irradiation power, provided information as to how much heat flowed from the microspheres to the surroundings. Finally, the high (> 70%) transduction efficiency justifies the effectiveness of gold nanoparticles as an energy transducing interface.

2.7.2.3 Specific heat capacity of the AuNP-PEGDA composite

The specific heat capacity of the AuNP-PEGDA microspheres was also determined using the same DSC. The procedure used to determine the specific heat for PEG wax as described above in section 2.3.2.1, was also used to determine the specific heat capacity of the composite, and the results are show in in figure 2.17.

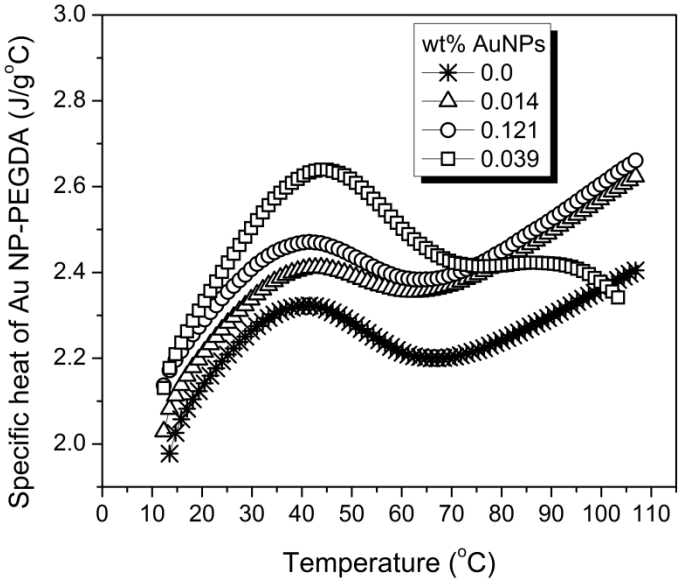

Figure 2.17: Specific heat capacity versus temperature of the Au NP-PEGDA photo-responsive composite

Three temperature scans were performed on each sample. The first run was a conditioning run, and the second and third runs were in good agreement (varying by less than 2%). At high temperatures the 0.039 wt% AuNP in PEGDA certainly displays a C_p as a function of temperature different than the other concentrations, with an unknown reason. In the region of interest, the Cp of each composite was similar, ranging from 2.0 to 2.7 J/g°C.

The importance in knowing the heat capacity of the AuNP-PEGDA composite becomes apparent in Chapter 3 when modeling actuation time. For instance, the heat transfer equations used to determine the time it takes for PEG wax to melt in the actuator – with a given amount of heat flow generating from the microspheres of a particular AuNP concentration – requires that the heat capacity of the heat source material is known. Additionally, the specific heat as a function of temperature, opposed to a single value, more accurately estimates the melting time in the heat transfer model.

2.8 Discussion

The temperature and heat flow of the AuNP-PEGDA composites were measured over a range of irradiation powers with each showing a linear increase in thermal response to an increase in irradiation power. Both the temperature as a function of irradiant power and power density as a function of irradiation intensity provides thermal property information if irradiation powers are extrapolated further for other applications. Additionally, the

maximum and average temperature of the AuNP microspheres observed under optical irradiation (125 °C and 100 °C) greatly exceeded the melting point of the PEG wax (43 °C), suggesting that a stimulus-responsive composite could be formed from these materials (provided that the concentration of the microspheres in the wax is also sufficiently high). PEG wax (Mn 1100 g/mol) was shown to undergo high volumetric expansion upon solid to liquid phase change (7.5%), which could form the basis for mechanical actuation. Finally, the high (> 70%) transduction efficiency justifies the effectiveness of gold nanoparticles as an energy transducing interface, and suggests that *localized* heating from a predetermined irradiation source should be achievable.

Chapter 3

Design, fabrication, testing, and modeling of the microactuator (and valve)

3.1 Introduction

This chapter describes the integration of a gold nanoparticle-polymer composite into an optically controlled microactuator. The actuator consists of a reservoir that contains phase change wax embedded with the photo-sensitive gold nanoparticle-polymer microspheres that were characterized in Chapter 2. Upon irradiation of the actuator with a predetermined wavelength of light, the phase change material expands considerably against an elastomer membrane due to the volumetric expansion that occurs upon melting of the wax. In this chapter, design aspects, fabrication, testing and modeling of the actuator are described.

3.2 Microactuator design

The main goal of this work was to design an optically-selective, remotely controlled microactuator, and to optimize this device to minimize the open-close (cycle) time and maximize the stroke displacement. For biologically-based microfluidic applications, practical actuation cycle times and displacements are considered to be on the order of milliseconds and in the range 5 to 150 μm, respectively. As described in Chapter 1, microactuators have been applied in microfluidic platforms such as microvalves and micropumps. The drawback in conventional microactuators (i.e., pneumatically controlled) – that display practical displacements and cycle times for parallel assay processing – is both their inherent bulky size and requirement for a physical connection to an off-chip air source, which limits their applicability to portable devices. To circumvent this limitation, it is envisaged to engineer and exploit stimulus-response materials as the actuating mechanism. The current drawback however, is that most remotely activated SRM-based microactuators either require several minutes, even up to hours, for the actuation cycle, and/or require a significant amount of energy to achieve actuation, as described in Chapter 1.

In our design, the microactuator is conceptually realized by enclosing a composite of PEG wax embedded with the photo-responsive AuNP-PEGDA microspheres (active material) in a sealed rigid reservoir with one end open and in contact with a flexible membrane that would expand upon melting of the wax, as shown in figure 3.1. Once irradiation on the reservoir stops, the membrane returns to its inactive position. The idea is that solid PEG wax would be stored in a small reservoir, then upon melting (irradiation), the liquid PEG would force through an orifice ($D_{orifice}$) to achieve a reasonable actuation height ($h_{actuator}$) for microfluidic applications.

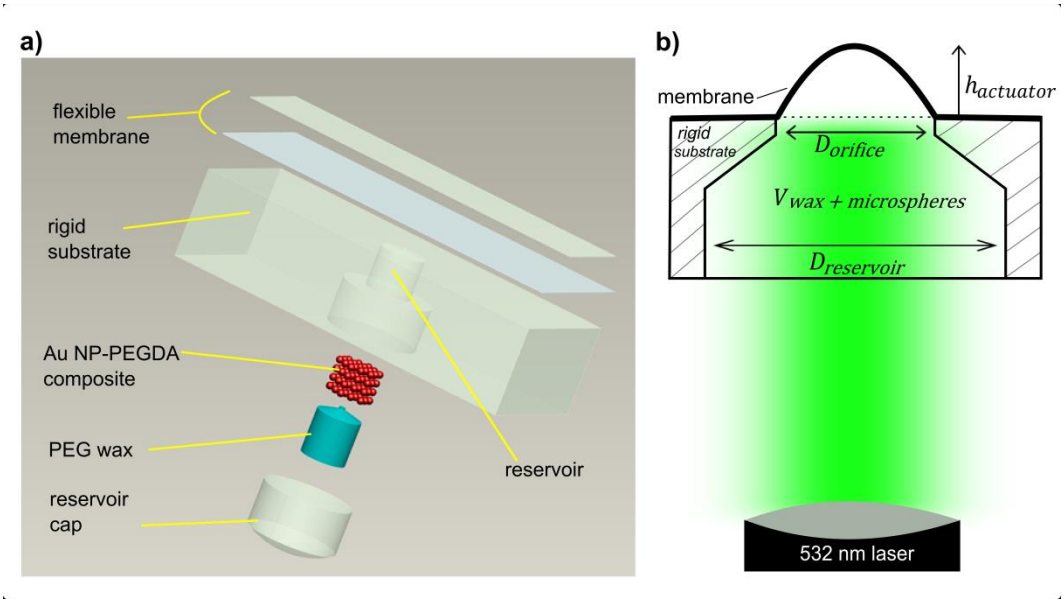

Figure 3.1: 3D and 2D drawing of the microactuator. a) Exploded view of the microactuator. b) Schematic of the remote activation of an actuator by a 532 nm laser source. Upon irradiation, the wax/microsphere composite in the reservoir melts, deforming a thin membrane to form a structure with height $h_{actuator}$ in the channel.

A critical parameter in actuators is the maximum height they can reach for a fixed volume of wax. A practical objective in the design of an actuator involves minimizing the volume of wax while maximizing its actuation height. Figure 3.2, compares two actuator geometries, D_1 and D_2, leading to different actuation heights ($h_2 > h_1$) with the same volume (V) of wax in each reservoir.

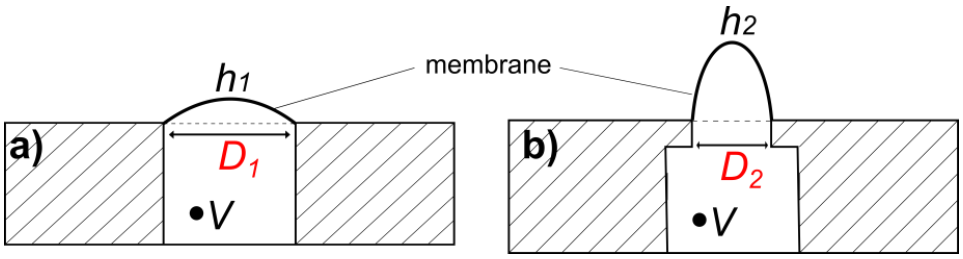

Figure 3.2: Comparing the effect of actuation height by changing the diameter of the orifice. a) Orifice diameter equivalent to the reservoir diameter, permitting small displacement over a larger area. b) Orifice diameter smaller than reservoir diameter resulting in a large vertical displacement over a smaller area.

Due to conservation of volume, it can be realized that if the orifice (identified with the diameter *D*) is decreased while the volume remains constant in the reservoir, the actuation area is compensated by this decrease in the actuator diameter, which effectively increases its actuated height. This can also be mathematically verified by solving for *h* when changing *D* in equation 3.1.

$$\alpha V_{PEG} = \frac{1}{6}\pi h_{actuator}\left(\frac{3}{4}D_{orifice}^2 + h_{actuator}^2\right) \quad 3.1$$

Where α is the coefficient of volumetric expansion of PEG wax, V_{PEG} is the volume of solid wax in the reservoir, $D_{orifice}$ is the diameter of the orifice and $h_{actuator}$ is the actuation height. In equation 3.1 the required volume (V_{PEG}) of PEG wax to fill a cap to a height $h_{actuator}$ can be calculated if *f*, $D_{orifice}$, and $h_{actuator}$ are known, which is important when comparing measured height to the theoretical actuation height.

In addition to the design parameters described above, the substrate material, active material, membrane material and method of bonding it to the substrate, reservoir cap material, and fabrication tools must be selected and optimized in the engineering of this device.

3.3 Microactuator materials selection

The main components of the actuator are the active material (i.e., photo-responsive microspheres and phase change wax), substrate material, elastomer membrane material, and the capping material.

3.3.1 Active material

Based on the characterization results in Chapter 2, the phase-change polymer wax composite with the highest concentration of gold nanoparticles (0.123 wt% AuNPs) was selected as the active material. The reason is because this concentration provided the highest power density for a given radiation intensity, and as a result would melt the PEG wax faster than if any lower concentration of AuNPs were used otherwise.

3.3.2 Substrate

The reservoir substrate had to meet the following criteria: It had to be easy to machine, to allow the 'insertion' of the reservoir, and it had to be rigid, so that the expansion of the wax did not lose mechanical energy due to compression with the sidewalls of the reservoir. Two rigid materials were considered due to the ease of their machinability and workability: cyclic-olefin-copolymer (COC) and polymethylmethacrylate (PMMA). PMMA (purchased from a local window supplier) was ultimately selected due to its easier workability.

3.3.3 Elastomer membrane

The membrane has two functions in a reversible device: (1) to isolate the wax from the fluid in the channel (preventing mixing), and (2) to apply a restoring force to the device, compressing the wax back into its initial reservoir during the cooling process. The membrane must be flexible enough to expand without tearing, but stiff enough to restore the actuator to the initial position. The bond between the membrane and the substrate must be sufficiently high to prevent any delamination at the orifice circumference. A polymer of particular interest was PDMS elastomer (Sylgard 184, Dow Corning), due to its flexible and ubiquitous nature. Designing the membrane layer depended primarily on the method of attaching it to the active material. As PDMS cannot be bonded directly to PMMA, in our design the idea was to apply first a thin (25 μm) double sided silicone adhesive (8026-15, Adhesives Research) to the PMMA, and then forming a thin layer of PDMS on the surface of the adhesive. The bonding of these layers initially proved problematic, and will be discussed in further depth in section 3.4.2.

3.3.4 Reservoir capping material

A final design factor was the capping material used to seal the AuNP-PEGDA-PEG mixture in the reservoir, as shown in figure 3.1(a). The capping material had to meet the

following criteria: it had to be optically transparent, to be in the initial form of a liquid state (photopolymerized resin) to ensure good conformation in the reservoir, and to form a strong bond with the PMMA substrate and reservoir material. A UV curable adhesive (Norland optical adhesive 68, Thor Labs) was selected as this material. To maximize the area of contact between the PMMA and the reservoir capping material, a larger diameter hole was drilled below the reservoir (i.e., a cap seat), as seen in figure 3.1(a).

3.4 Fabrication of the microactuator

As was depicted earlier in figure 3.1, the actuator consists of three geometric features shaped in PMMA plastic: a reservoir and an orifice, and a cap seat that contains the reservoir. The reservoir volume supports the microspheres and wax, and the orifice is a hole sharing a common axis with the reservoir through which wax flows when melted. The process used to fabricate the actuator is illustrated in figure 3.3.

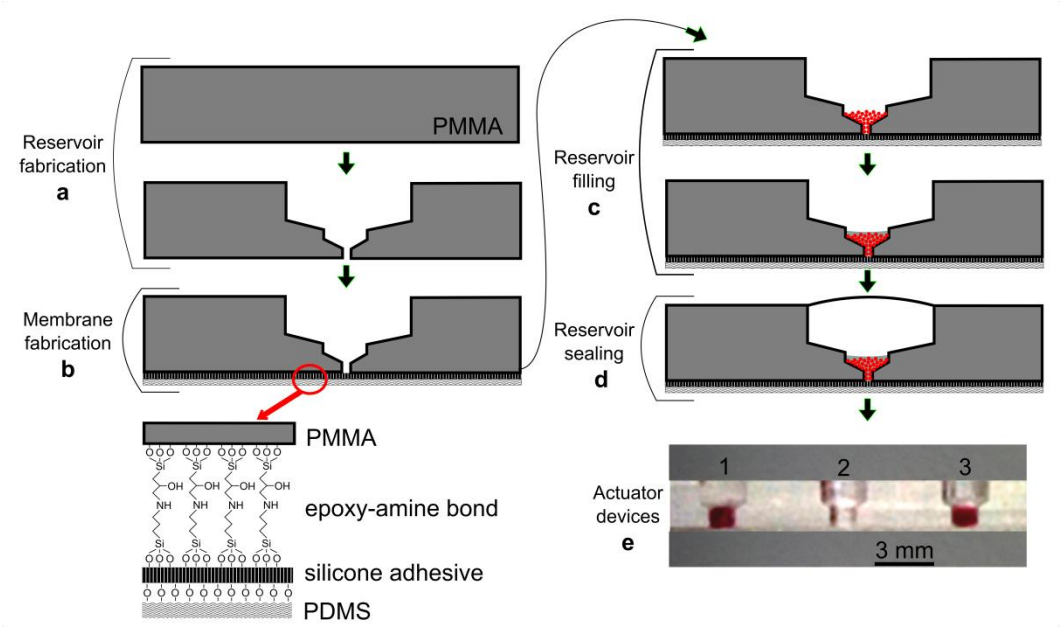

Figure 3.3: Microactuator fabrication steps. a) A hole is drilled in the PMMA substrate to create the reservoir. b) The surface of PMMA and the silicone adhesive are functionalized using amine-epoxy terminated silane to promote adhesion. The silicone adhesive is then applied to the PMMA followed by spin coating a thin layer of PDMS to form the flexible, well-bound membrane layer for the actuator. c) The photo-responsive microspheres are inserted into the reservoir. PEG wax is then added to the reservoir. d) The reservoir is finally sealed using a transparent, UV-curable adhesive. e) A photograph of three final devices in one PMMA substrate. Device 1 has a higher ratio of microspheres to PEG wax in comparison to device 3, and therefore appears darker in color. Device 2 has an empty reservoir.

3.4.1 Reservoir fabrication

The first step in the fabrication process was to create the reservoir to hold the stimulus-responsive composite mixture. The diameter of the reservoir was designed to be identical to the laser beam diameter (1 mm), which enabled irradiation of all the microspheres for optimal energy transduction. The reservoir tapers to an orifice ~3/10 of the initial diameter of the reservoir in order to increase the actuation height for a given volumetric expansion of PEG wax. The diameter of the orifice was determined by optical microscopy to be 270 μm, as measured in comparison to a well-known reference. Fabricating the reservoir involved three separate shaping steps: (i) boring the preliminary hole, which served as the volume to support the reservoir cap as shown in figure 3.3(a); (ii) drilling the secondary hole, forming the volume in which the wax and microspheres were contained; (iii) and finally boring the orifice hole through which the wax actuated from the taper from the reservoir. Each of the preceding steps was carried out with standard machine shop drilling tools, with the exception that the 270 μm orifice hole, which was made using a 30 gauge syringe needle.

3.4.2 Membrane bonding

In our design, actuation occurs as the AuNP-PEG wax composite expands through the tapered orifice, reversibly deforming a thin membrane which provides both a physical barrier for the wax and provides a restoring force to return the actuator to its initial state upon cooling. To ensure reversible actuation and to prevent delamination, it was important to form a strong bond between the flexible membrane and the PMMA substrate. To guarantee a strong bond between the adhesive-PDMS composite layer delaminating from PMMA, a chemical treatment was utilized to introduce an epoxy-amine bond at the interface [61]. This technique involved functionalizing a double-sided silicone adhesive and PMMA surface with two molecules: of (3-aminopropyl) trimethoxylsilane and (3-glycidoxypropyl) trimethoxysilane, followed by mating the two layers under pressure for a period of time (figure 3.3(b)) – the exact surface treatment details can be found in the above reference. After treatment, PDMS was then spin coated on the other adhesive side bound to PMMA and cured at 70 ºC for 2 hrs. The membrane thickness was then measured using an alpha step profilometer as 50 μm, which is the combination of the silicone adhesive and PDMS layer. This surface treatment proved highly effective in preventing delamination and wax leakage, as shown in figure 3.4(c, d). Without surface treatment, it was confirmed that the adhesive-PMMA bond alone was

delaminating during the volume expansion of wax, which was visually evident as wax leaked around the orifice perimeter, as shown in figure 3.4(a, b).

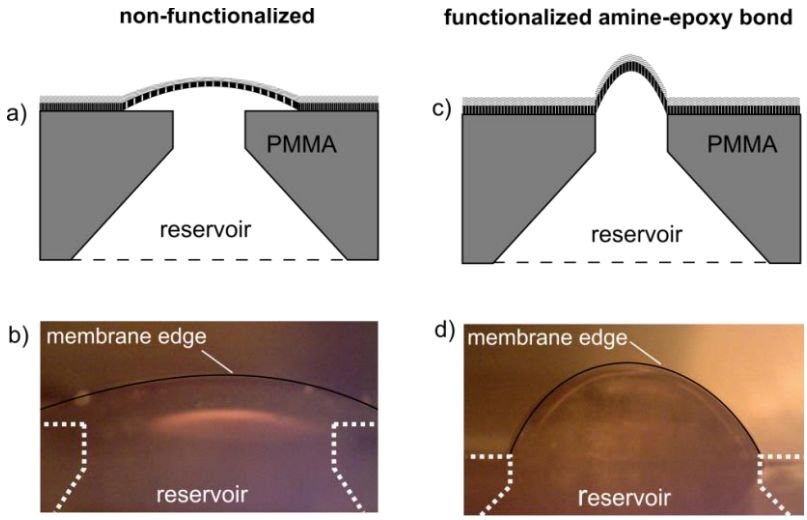

Figure 3.4: Comparing functionalized and non-functionalized surface treatment of the elastomer membrane with a substrate in expanded PEG wax. a) Diagram, and b) photo illustrating delamination of the membrane with the substrate due to an insufficient bond. c) Diagram and (d) photograph illustrating an actuator with a strong bond between the membrane with the substrate due to the surface treatment.

3.4.2.1 Testing of the PDMS elastomer bond strength with a PMMA substrate

The strength of the amine-epoxy bond was evaluated with a peel test mechanism mounted to a tensile tester (Instron tensile tester, 5940 Series, 1 kN load cell, Norwood, MA). The objective of the test was to measure the effect of the epoxy-amine chemical bond between PMMA and the silicone adhesive at various curing temperatures and times. A diagram depicting the cross-section of the material layers in the test coupon (PMMA-(epoxy-amine bond)-silicone adhesive-PDMS) is shown in figure 3.5.

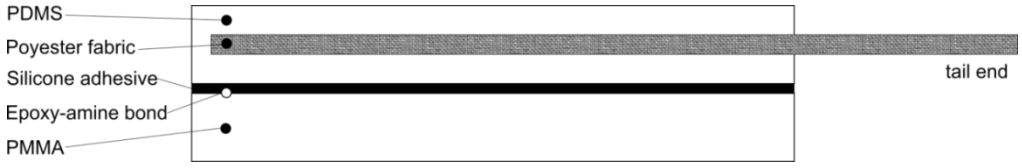

Figure 3.5: Diagram illustrating the cross section of a test coupon in evaluating the effect of surface treatment.

A polyester fabric strip was embedded in PDMS a distance away from the silicone adhesive, and with enough fabric overhanging, as a tail end, to be later used as the clamping location with the tensile tester grips. The fabric was selected based on the fact that it bonds readily to PDMS. Upon extension (12 mm/min) of the tail end, the tensile

force is transferred from the fabric to the PDMS-(epoxy-amine)-PMMA interface, figure 3.6.

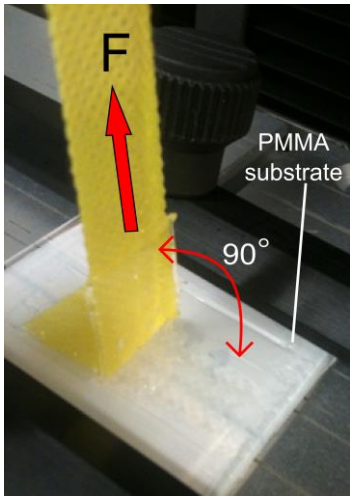

Figure 3.6: Photo of a test coupon used in evaluating the effect of surface treatment. The symbol 'F' represents the direction of force from the tensile tester.

The effectiveness of the surface treatment was so great that the PDMS (sample cured at 70 ºC for 2 hrs) started tearing from itself at approximately 8 N, indicating that a strong bond was achieved, whereas using the same PDMS and adhesive layers without surface treatment, a force of only 0.1 N was required for delamination, as shown in figure 3.7.

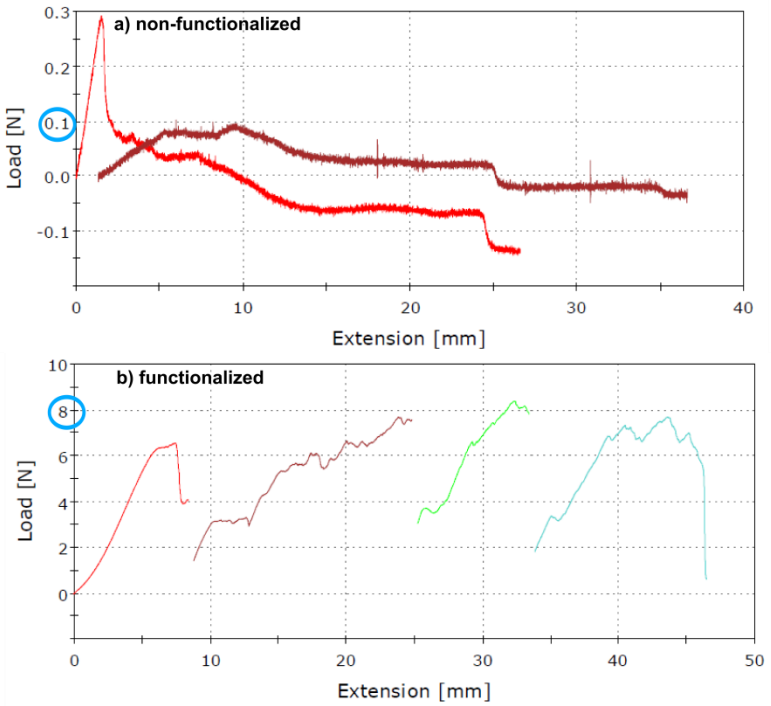

Figure 3.7: Peel test data comparing functionalized and non-functionalized substrate and film composite. a) Non-functionalized sample. b) Functionalized sample showing significantly higher forces required to peel off PDMS. Each curve represents the same sample with consecutive interruptions (without zeroing the gauge length). The amine-epoxy bond strength was so high that PDMS was tearing from itself, hence each test of the same sample was stopped at the onset of tearing. To confirm tearing, the sample was first conditioned with a knife to remove the PDMS tear (creating a tear free extension surface), followed by tensile extension.

Comparing the two graphs in figure 3.7, it is apparent that the force required to peel the functionalized material is nearly two orders of magnitude greater than for the non-functionalized material. Note that the peel area across all tested samples was the same. Figure 3.7(b) represents consecutive tests on a single sample. Each time that the PDMS would tear away from the fabric (rather than delaminating from the PMMA), the test was interrupted, and the fractured PDMS was removed. The test was then performed again on the same sample (without zeroing the gauge length). As can be seen from the figure, failure typically occurred when the force reached around 8 N. The actual force required to delaminate the PDMS from the PMMA is therefore higher than this value. Overall these results show that good bonding between the PDMS and PMMA was achieved.

3.4.3 Reservoir filling and sealing

The final step of the fabrication process was to back-fill the wax-Au NP-polymer microsphere composite into the reservoir. Microspheres were first added to the reservoir

in increments with the use of a digital pipette (figure 3.3(c)). PEG wax was then added to the reservoir (figure 3.3(c)). Solid chunks of PEG wax were placed into a small vial and melted at 50 °C. At the same time a metal disk (body of thermal mass) was heated to 60 °C. The developed PMMA sample was placed on the thermal mass to keep the system above the melting point of PEG wax. Using the tip of a pipette, a small quantity of PEG wax was dispensed so that a very small volume contacted the microspheres in the cavity. The samples were then placed in a vacuum desiccator for 30 minutes with the thermal mass to remove trapped air bubbles. When the PEG wax solidified, the Norland optical adhesive was doused into the larger cavity and exposed to UV light for 2 minutes to polymerize the resin (figure 3.3(d)). Due to the small volumes involved, adding precise amounts of microspheres and wax was challenging. The total mass of microspheres and wax added was determined by weighing the devices using an analytical balance (Mettler Toledo XS105, with 0.01 mg resolution) before and after the addition of each material.

3.5 Testing of the microactuator and valve

Measuring actuation displacements amounted to two different measurement techniques: mechanical displacement measurement, and an optical displacement measurement which proved superior. Since the actuator device was difficult to integrate with measurement systems, custom instrumentation for displacement measurements was built in-lab.

3.5.1 Cantilever displacement measurement

Visualizing the small displacements achieved by the actuator was initially challenging. The first approach that was employed used a thin wire placed on the actuator as a cantilever to amplify the displacement. If the height of the displacement of the cantilever was known, it could be used to calculate the actual displacement of the actuator using basic geometry, as shown in figure 3.8. The method used to determine actuation height exploits the fact that small rotational changes can yield large arc length displacements, given a long enough radial arm.

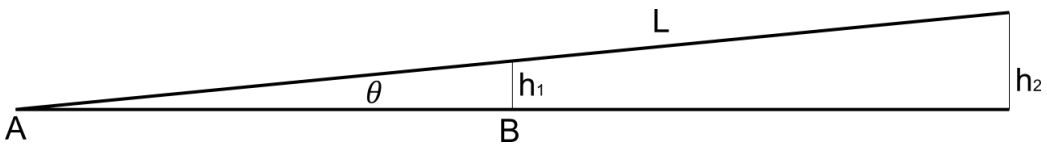

Figure 3.8: Geometry used to determine actuation height in the displacement measurement setup.

If it is imagined that the actuator is placed at position B and actuates to a height h_1, then the resolution for measurement increases by exploiting the radial arm L, which increases to h_2. Hence if one knows the distance AB and length L, after measuring h_2 one can determine h_1, equation 3.2.

$$\theta = \sin^{-1}\frac{h_2}{L} = \tan^{-1}\frac{h_1}{AB} \rightarrow h_1 = AB * \tan\left(\sin^{-1}\frac{h_2}{L}\right) \quad 3.2$$

To realize actuation, the measurement architecture was tested by placing a thin copper wire (100 µm), which was free to rotate, on the actuator. The wire was used both as an electrical conductor and as a radial lever, which was connected in a closed loop circuit according to figure 3.9.

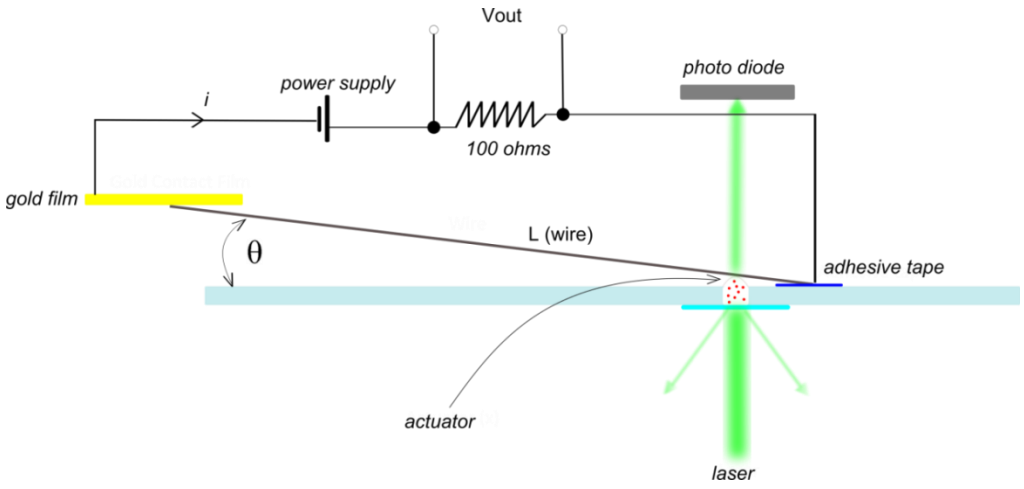

Figure 3.9: Setup in the cantilever displacement measurement of the actuator

In this set-up, the power of transmitted light through the sample and voltage in the closed/open were simultaneously measured, figure 3.10. Once the copper wire would make contact with the gold pad, the circuit would close and the voltage would drop by 3 volts. Recall that when the actuator would move, the cantilever (wire) would rotate radially through an angle θ, eventually making contact with the gold film. The actuation height could be determined from equation 3.2. This experiment was performed using an actuator sample that contained 0.7 mg of AuNP-PEGDA microspheres (0.123 wt%) and 1.2 mg of PEG wax in the reservoir, with the fabrication method described in section 3.4.1. The voltage profile collected during this experiment is shown in figure 3.10, along with the transmitted power profile from the laser, as measured by a photodiode behind the sample. When the laser was turned on, the photodiode measured transmission of light

through the actuator. The non-linear profile in figure 3.10 of the irradiant power represents the melting profile of PEG wax in the reservoir, which eventually levels off to a point where all the wax has melted.

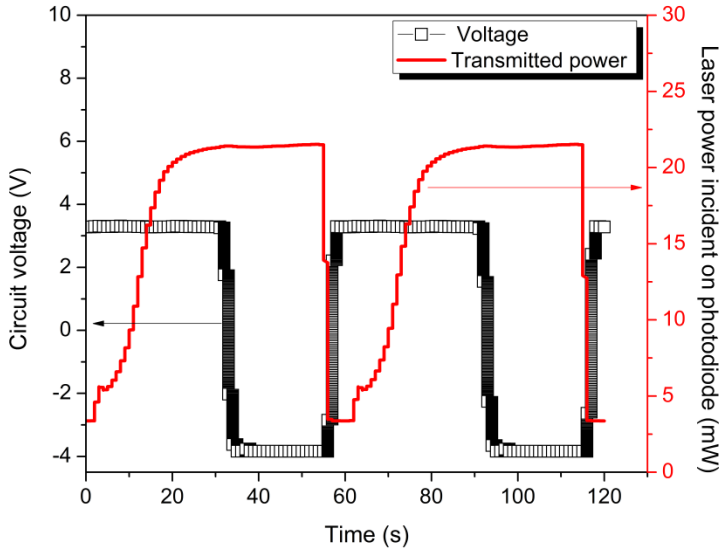

Figure 3.10: Results of the cantilever actuator displacement measurement. When the actuator displaces to a maximum height, the lever resting on it makes contact with a contact pad effectively closing the circuit, as seen in a voltage polarity reversal. When the laser is turned off, an open circuit is formed as a sudden rise in voltage.

Proof of actuation was observed from the results illustrated in figure 10, where from 32 s to 58 s, the voltage switched in polarity – indicating that actuation had occurred. The time to actuate, from the onset of irradiation, was 29 s. A second actuation cycle was again demonstrated from 90 s to 119 s. Using equation 3.2, along with known values from the actual geometry of the cantilever, the actuation height h_1 was calculated as 32 µm. The cantilever method provided evidence of reversible and cyclical actuation of the devices. However, post actuation inspection of the contact area of the wire with the actuator membrane showed that the wire was too heavy for the membrane, evident as a dimple in the actuator membrane. The influence of mass on the actuator was hampering the true, un-weighted, displacement of the actuator. In addition, only a maximum displacement could be measured (binary yes/no), and it was of interest to know the dynamic response of the actuator. A different approach was therefore required to allow quantification of the total displacement.

3.5.2 Optical displacement measurement

A measurement which proved higly succesful in observing quantitative micrometer displacements combined optical detection and implementation of an image processing algorithm. The optical detection setup is illustrated in figure 3.11. A 72 mw laser (the same laser used in all measurements performed in Chapter 2) was positioned 10 cm below the actuator device, with the laser beam aligned to irradiate the reservoir. A video camera (Aven Mighty Scope, 500X magnification) was positioned with a x-y-z micrometer to view the actuator. A beam splitter (glass slide) was aligned with the laser beam, and reflected a small portion of light to a photodiode, which was used to monitor the laser intensity. A video camera was used to image the deformation of the actuator. As scattered green light disrupted this imaging, a high-pass optical filter was placed in front of the camera, and additional illumination of the sample was achieved using a red LED (630 nm). The LED and photodiode were connected to a data acquisition module (NI USB 6009) and programmed with LabView in a sense and control arrangment (see section A.4 for LabView code), whereby the LED would illuminate whenever laser light was detected with the photodiode.

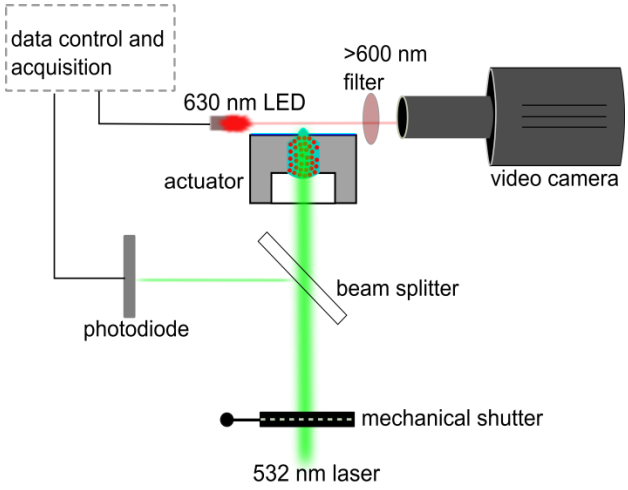

Figure 3.11: Schematic of the optical measurement system utilized to characterize the actuation of the membrane device.

The raw video footage was then processed in matlab using a custom image processing algorithm (see section A.5.1 for program code) to obtain height versus time data with results shown in figure 3.12. Two programs were run simultaneously: one analyzed the red LED versus time and the other analyzed the membrane edge versus time. Each image in the video sequence was then analyzed in a logic loop to determine the

pixel location of the membrane edge at a particular time. The true height of the actuator was calibrated against a standard reference. By dividing the image height by a ratio of pixel width to true width of the reference, a true displacement was determined.

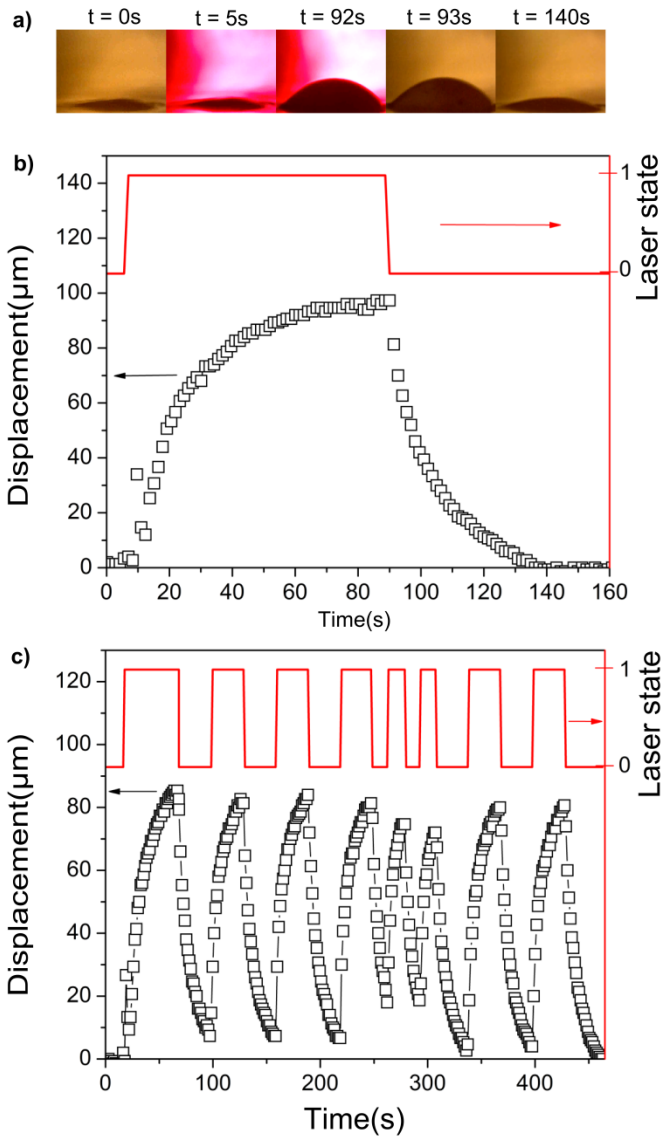

Figure 3.12: Results demonstrating displacements of the optically driven microactuator. a) Actuation displacement timeline. The red light is an indicator light when irradiation with the laser occurs. b) Corresponding displacement versus time of the actuator from the timeline video footage. c) Actuator displaying reversible actuation cycles.

In figure 3.12(a) frames are shown from the raw video footage display the deformation of the membrane during irradiation and cooling for an actuator device containing 1.4 mg of PEG wax and 0.84 mg of microspheres (0.123 wt% Au NPs in PEGDA). These images were analyzed using the algorithm described above to yield the displacement versus time results provided in figure 3.12(b). The 'Laser state' axis in

figure 3.12(b) describes whether the laser was on or off, as imaged through the red LED. Eight reversible actuation cycles are shown in Figure 3.12(c). Each cycle took approximately 100 s to complete.

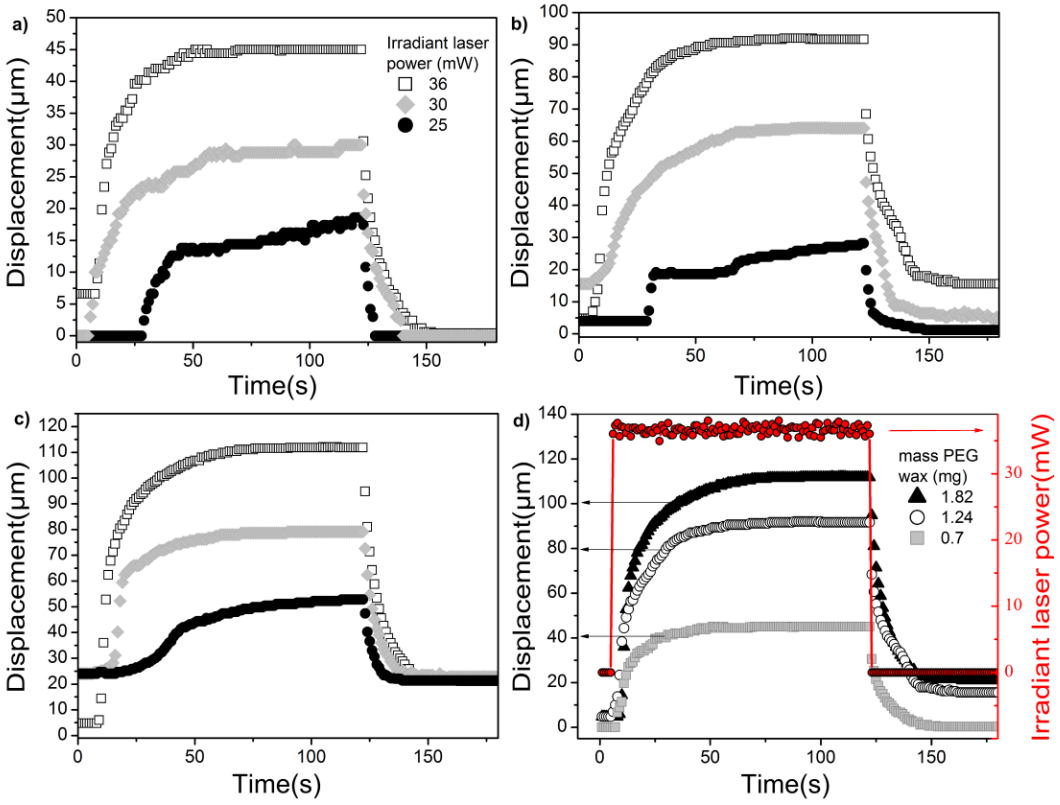

Figure 3.13: Displacement versus time curves at different irradiation intensities. a) Mass of 0.7 mg of PEG wax in the reservoir. b) Mass of 1.24 mg of PEG wax in the reservoir. c) Mass of 1.82 mg of PEG wax in the reservoir. d) Compiled plot representing maximum irradiant power and mass of PEG wax in the reservoir.

Two variables were independently controlled for the characterization of the performance of the actuator: the irradiation power and the mass of PEG in the reservoir. The actuation curves for three devices are shown in figure 3.13(a-c), with each having a different loading of Au NP-polymer microspheres and PEG wax in the reservoir as shown in Table 1. For each device, the displacement of the membrane was measured successively at intensities of 36 mW, 30 mW, and 25 mW. Figure 3.13(d) summarizes the mass-based displacement curves in (a-c) which were illuminated at the greatest intensity (36 mW), and provides data of irradiation power.

Device	mass of microspheres in reservoir (mg)	mass of PEG wax in reservoir (mg)
a	0.86	0.7
b	0.7	1.24
c	1.23	1.82

Table 3.1: Mass of Au NP-PEGDA microspheres and PEG wax in the reservoir of the actuator. Devices **a**, **b**, and **c** correspond to graphs a-c in figure 3.13.

While ideally the mass of microspheres would be constant between devices, the accuracy in adding microspheres to the reservoir was limited by the precision that could be achieved using the 20 μL digital pipette, with an average mass of 1 ± 0.3 mg. The spread in microsphere loading is not expected to have a significant impact on device performance because each mass of microspheres exceeds the threshold required to absorb all of the incident light at the relevant intensities (i.e. all of the energy from the beam was absorbed by the particles in each of the three devices).

Three different performance effects are observed in figure 3.13: (1) decreasing irradiant power decreases actuation height, (2) increasing the mass of PEG wax in the reservoir increases both the actuation height and cycle time, and (3) as the mass of PEG wax in the reservoir increases, the tendency of the membrane to return to its original zero displacement decreases. By reducing the irradiant power, the actuation height decreases for each device. Each curve appears to asymptote to a particular displacement, corresponding to the steady-state between heat flow to the system and heat lost to the surroundings. Different heights are likely achieved due to different fractions of material undergoing the phase transition. At 36 mW, it could be seen visually that all of the wax in the system was melted, therefore further increases in intensity are not expected to lead to significantly greater displacements. The second effect (increasing actuation height with increased loading of PEG wax) is simply due to the fact that as the mass of PEG wax in the reservoir increases, the available volume of PEG wax for expansion also increases, which in turn increases the overall actuation height. As shown in figure 3.13, the mass of PEG wax in the reservoir also influences the hysteresis in the deformation of the device: for higher masses of the PEG wax in the reservoir, the final shape of the actuator upon cooling is less flat. Two factors may contribute to this effect: (1) The restoring force of the PDMS membrane may be insufficient for higher masses of wax, since larger masses will require higher forces, and (2) when larger displacements are achieved (i.e. in reservoirs with higher masses of PEG wax), higher surface areas result

along the membrane. If cooling proceeds preferentially from these surfaces, the deformed shape is more likely to be preserved upon cooling (rather than a return to the undeformed shape). The data in figure 3.13 also illustrates that a fine balance is required to fully optimize an actuator that yields a maximum height while having the ability to return to zero displacement (i.e. undergo a fully reversible cycle).

The actual and theoretical displacement of the microactuator were also compared in table 3.2. By using equation 3.1, the theoretical maximum displacements ($h_{actuator}$), as a function of mass of PEG in the reservoir, were calculated for the same devices **a**, **b**, **c** from figure 3.13.

Device	PEG wax (mg)	actual displacements (μm)	theoretical displacements (μm)
a	0.7	42	401
b	1.24	90	502
c	1.82	110	581

Table 3.2: Comparing actual to theoretical displacements of the actuator as a function of PEG wax in the reservoir. Devices **a**, **b**, **c** corresponds to the same devices in figure 3.13.

The exact cause for the discrepancy between the actual and theoretical actuation height is unknown, however, several possibilities are suggested:

1 Fabrication
   - In step c of figure 3.4, the addition of PEG wax to the reservoir may result in air voids.
   - In step d of figure 3.4, the interface of the capping layer and the reservoir may not form a perfect seal, effectively creating an air void.

2 Material degradation
   - PEG wax is known to undergo oxidative degradation whereby oxygen from the air creates scissions in the long polymer chains, effectively reducing the melting point [50]. Since it was often observed in the samples that a glossy surface would arise after 30 minutes exposure to air, it was believed that a fraction of the PEG in the cavity was effectively degrading to a melting temperature lower than room temperature.

It is important that the measurement error in the measurement of PEG wax added to the reservoir was ruled out, as the mass could be repeatedly confirmed with a high precision weigh scale (Mettler Toledo XS105, with 0.01 mg resolution). Air voids

present due to fabrication errors were not observed with optical microscopy, however, their presence is not necessarily ruled out. To determine whether or not the melting point of PEG wax reduced as a result of successive exposure to air (oxygen) and elevated temperatures, DSC was utilized to observe whether differences in thermal properties could be seen in PEG wax samples exposed to elevated temperatures for extended periods of time. A DSC was highly suitable to evaluate chemical degradation of PEG wax since it measures endothermic and exothermic heat flows to or from a material, which reflects the properties of the material such as heat capacity, melting point, etc. In this particular case, if the chain length of PEG wax was decreasing due to oxidative degradation, the melting point should also have decreased, therefore the DSC would be highly effective in measuring this change. The results are shown in figure 3.14.

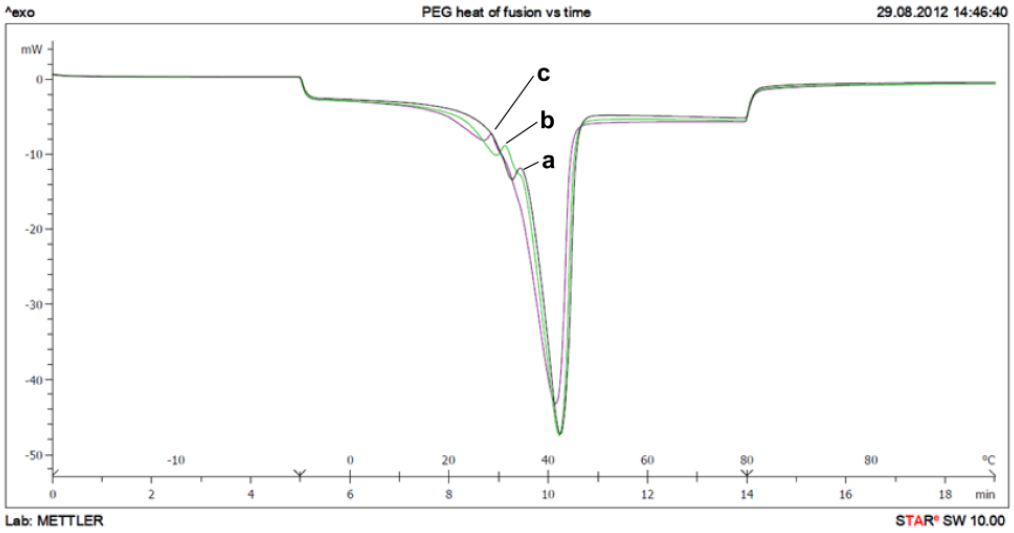

Figure 3.14: Cyclic DSC temperature scan of PEG wax exposed to air. The heating rate was 10ºC/min with each curve representing the same sample. a) Scan of PEG wax 5 minutes after air exposure. b) Scan of the same sample but 22 minutes of exposure to air and elevated temperature. c) Scan of the same sample after 24 hrs of exposure to air at 25 ºC.

A small trend was observed in figure 3.14 from curves 'a' to 'c' with cycled atmosphere and temperature exposure. For each melting profile of PEG wax, there is a preliminary peak prior to the major melting peak, which may be due to material softening or chain rearrangement prior to complete melting. This preliminary peak shifted to lower temperatures in successive DSC temperature scans. In figure 3.14, curve 'a' shows the melting curve after PEG was exposed to ambient air for 5 minutes. Curve 'b' is immediately after the first test (22 minutes) and curve 'c' is a DSC temperature scan 24 hrs after the second test while maintained at room temperature. It is evident that the

melting point is shifting to a lower temperature, however not considerably. In this temperature and air exposure cycling, it is unknown also by how much the volume expansion changed and therefore cannot be considered as the main source of error.

To conclude on the discrepancy between the actual and theoretical displacement, its exact source is unknown but it is believed to source from the processing of PEG wax in the reservoir that results in voids and/or due to the chemical degradation of PEG wax. In Chapter 4, ideas are proposed to circumvent this discrepancy under the possible sources of error listed above.

It is also important for various applications to know the force generated by actuators. The force that the deformed membrane produced was also measured for device c in table 3.1. A force transducer was calibrated for small forces using a high precision weigh scale, with a calibration plot shown in Appendix A.3. The force generated by this particular actuator was 22 mN. If this force is taken over the membranes footprint area, the pressure it creates is P = 45 psi, while taken over the membranes total surface area P = 22 psi.

3.6 Modelling

3.6.1 Predicting actuation time

To explore scaling effects in our design, and to understand how changing the size of the reservoir would affect the time response of the system, a COMSOL heat transfer model was developed. If one excluded the effect of heat transferred to the surroundings and only considered the heat generation to the PEG wax alone, then the time to melt the wax can be analytically calculated as follows:

$$E_{in} = E_{out} \tag{3.3}$$

$$\int Q\,dt = m_{spheres}\int_{T1}^{T2} C_p(T)dT + m_{PEG}\Delta H_{m(PEG)} \tag{3.4}$$

Equation 3.4 is simply an energy balance, in which the heat capacity of microspheres is given by $Cp\ (T) = -5E\text{-}08x^4 + 2E\text{-}05x^3 - 0.0016x^2 + 0.0658x + 1.5123\ J/g^oC$, where the temperature is represented as T, the heat flow $Q = 23$ to $49\ mW$, the mass of the microspheres $m_{spheres} = 0.7$ to 1.23, the mass of the PEG $m_{PEG} = 0.7$ to $1.82\ mg$, $(T2 - T1) = (43 - 26.5)^oC$, and the enthalpy of fusion of the PEG $\Delta H_{m(PEG)} = 130.9\ J/g$. For the

range of masses used in the actuation experiments, the time required to melt the wax was calculated to be between 4 to 6 seconds. Indeed this actuation/melting time is significantly shorter than what was actually observed (42 to 91 seconds), hence the need for a numerical model that takes into account heat loss from the wax to the surroundings.

With greater accuracy, the theoretical time to melt all the wax (which should correspond to the time required to achieve full actuation/displacement of the membrane) for a given volume of PEG in the reservoir was calculated using a numerical heat conduction model in COMSOL. Within the heat conduction model, the heat source was a collection of micropsheres of the AuNP-PEGDA material embedded in a solid cube of PEG wax, as shown in figure 3.15(b and c), where the two materials are enclosed in the 'reservoir boundary'. The position of the two materials within the PMMA was mimicked to their location in the actual microactuator device; therefore the same dimensions, offsets and values of proportionality were used. Equations 3.5 and 3.6 can then be used to estimate the time to melt wax.

$$\rho C_p \frac{\partial T}{\partial t} + \rho C_p \boldsymbol{u} \cdot \nabla \mathrm{T} = \nabla \cdot (\mathrm{k} \nabla \mathrm{T}) + Q_{gen} \quad 3.5$$

$$-\boldsymbol{n} \cdot (-k \nabla T) = h \cdot (T_{ext} - T) \quad 3.6$$

Where C_p is the specific heat capacity, ρ is the density of material, k is the thermal conductivity, h is the convection coefficient, Q_{gen} is the heat source, T_{ext} is the external air temperature, t is time, and T is the temperature of the thermal element of interest. The heat source originated from the mass of PEGDA-AuNP microspheres used in real devices, and their heat capacity was evaluated in Chapter 2. The $C_p(T)$ of PEG wax was considered as the sum of the specific heat capacity and the heat of fusion (130 J/g^{o}C), which was also measured with a DSC in Chapter 2. The thermal conductivity of the PEGDA-AuNP composite was estimated to 0.69 W/mK by calculating a weighted average of polyethylene glycol and gold in the mixture with their respective thermal conductivities, 0.26 and 318 W/mK. Convective cooling was also taken into account in equation 3.6. The external ambient temperature was the same as in the actuation measurements (23 °C). The convection coefficient is typically in the range of range 1 – 20 W/m^{2}K, depending on the degree of air flow and sample geometry, here a value of 5 W/m^{2}K was utilized to reflect the fact that the flow of air across the actuator during the experiment was very low.

To evaluate the time required to completely melt PEG wax – and fully actuate the device, the time-dependent model established from equations (1) and (2) was run for 150 s, and the average temperature of PEG wax in the reservoir was calculated as a function of time, with the result shown in figure 3.15(d). The wax was considered melted when this temperature was equal to the melting temperature of the PEG wax 43 °C (216 °K).

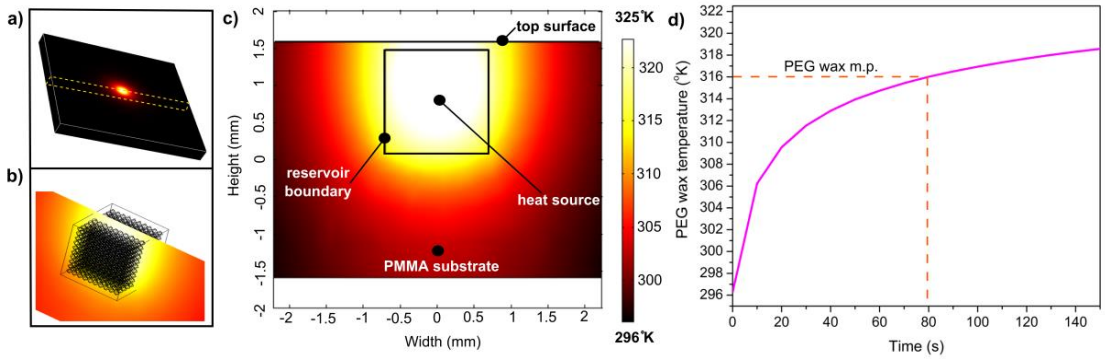

Figure 3.15: Thermal modelling of the reservoir corresponding to the microactuator. a) Top view showing the temperature of the actuator surface at 150 s irradiation. b) Side view depicting a collection of microspheres embedded in a cube of PEG wax. c) Temperature profile of the heat source embedded in PEG wax. Temperature at the PEG wax-PMMA interface. The horizontal (red) dotted line is the melting temperature of PEG wax and corresponding time to reach this temperature

To compare the results of the model with the experimental results, the time required to reach 99% of the maximum displacement was experimentally chosen as the time at which all the PEG wax in the reservoir melted. It can be seen that the range of melting times as a function of mass of PEG wax in the reservoir is $42 < t(s) < 91$. Under the simulation, the predicted time as a function of mass (0.7, 1.24, and 1.82 mg) were in the range $39 < t(s) < 80$. The predicted range differs on average by approximately 10% to the actual range of time required to melt wax. The ultimate source of discrepancies are the differences in the geometry of the real and modeled systems, the fact that in the real system heating would proceed non-uniformly (originating preferentially from the direction of the laser beam) among distributed microspheres, differences between the utilized and actual convection coefficient, and the assumption that all the wax in the reservoir melted. Nonetheless, the model provides a fairly good prediction of the actual behavior.

The model was also utilized to examine the effect of varying the reservoir size, as in many systems the time of actuation can be reduced greatly as the size of a system is reduced due to scaling effects. To perform this prediction, three constraints were applied to the system:

1) The ratio of mass of the heat source to the phase change material was held to a constant equivalent to the ratio of mass of microspheres to PEG wax in device b from table 3.1: $\frac{m_1}{m_2} = 0.56$
2) The total heat generation of microspheres was held constant: $Q_{gen} = 23\ mW$
3) The ratio of the center location relative to the top surface of the device from a common datum, for the heat source and PEG wax was held constant.
4) Convection coefficient was held constant: h = 5 W/m^{2}K

The results of scaling are presented in figure 3.16 as time versus effective radius (taken as a sphere: the sum volume of PEG wax + microspheres). The results indicate, under the above constraints, time decreases to the fifth power with radius.

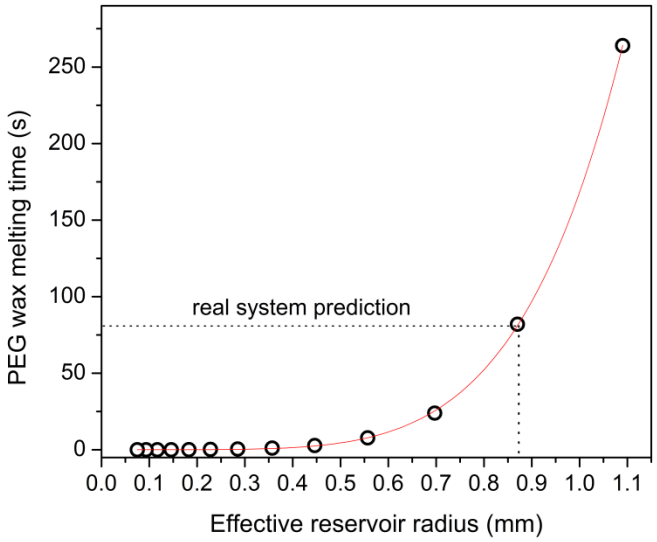

Figure 3.16: Theoretical prediction of the time required to melt the PEG wax as a function of reservoir radius for constant AuNP-PEGDA microsphere concentration, heat generation and constant ratio of AuNP-PEGDA microspheres to PEG wax in the reservoir. The data can be fit by a fifth order exponential curve.

The results summarized in figure 3.16 indicate that if the radius is halved the required melting time remarkably decreases from 80 seconds to 1 seconds. Based on this prediction, it is recommended to scale the system smaller from our current design, and to verify with further research. Though this prediction shows exponential decrease in melting with a small reduction in reservoir radius, there will be trade-offs. For instance, decreasing the radius will decrease the available volume of PEG wax for expansion. An optimal balance of reservoir radius and wax volume would require further research.

3.6.2 Comparing volumetric versus planar heating of PEG wax

It was hypothesized in Chapter 2.1 that volumetric heating of a phase change material would melt faster than planar heating of the same mass of PCM with equivalent heat generation. This is proved by utilizing the COMSOL model as described in the preceding section. The geometries compared are illustrated in figure 3.17.

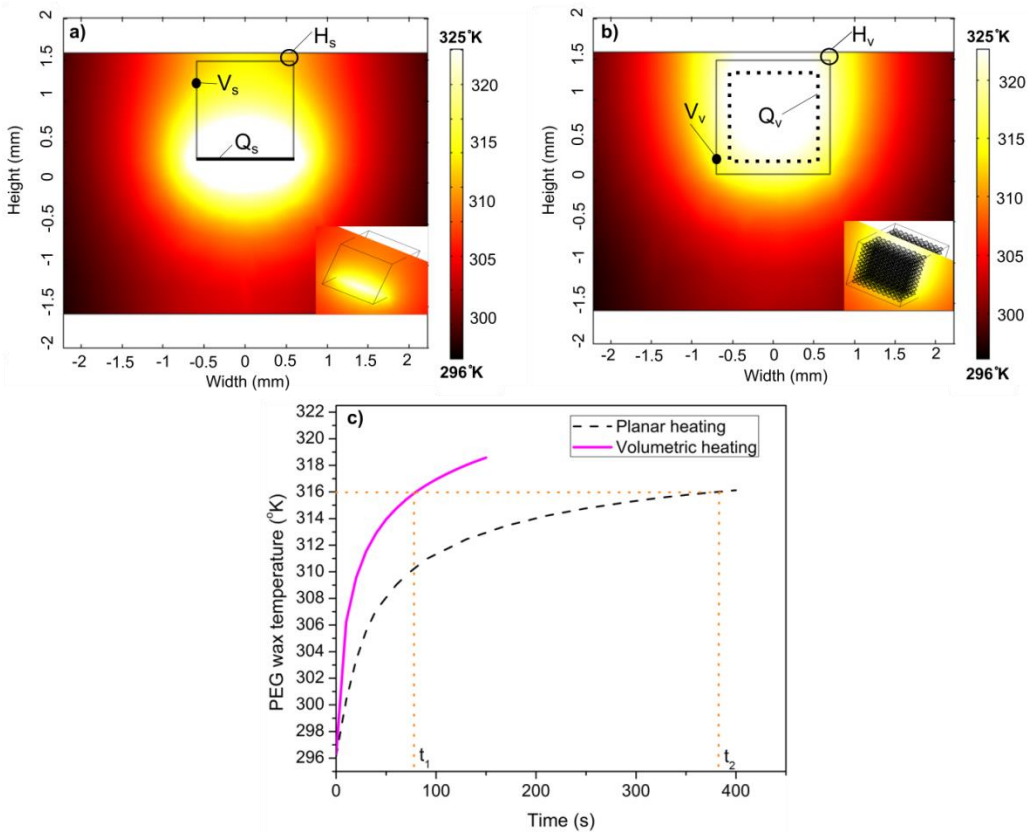

Figure 3.17: Comparing geometries of planar and volumetric heating with equivalent volume of PEG wax and heat generation. a) Planar heating below a cube of wax situated in a PMMA substrate. a) Volumetric heating via microspheres distributed in a cube of wax. c) Results showing the time it takes for both geometries to completely melt the entire cube of wax.

In figure 3.17(a) a surface heating element Q_S is positioned at the bottom of a cube of PEG wax, while in figure 3.17(b) a collection of microspheres generating heat Q_V are distributed throughout a cube of PEG wax. To make respectable comparisons between geometries, several common properties were applied: (1) The volume of PEG wax in each geometry is the same, $V_S = V_V$ (2) The total heat generation is the same, $Q_S = Q_V$ (3) And the position of the top surface of the cube of wax to the top surface of the PMMA substrate is the same, $H_S = H_V$. The time required to melt PEG was compared by referring to the time it takes to reach an average temperature of the volume of PEG wax corresponding to 316 °K, with results presented in figure 3.17(c). It can be easily verified

that the melting time of a cube of wax via volumetric heating compared with planar heating of the same cube of wax occurs more rapidly as $t_1 < t_2$ shown on the x-axis in figure 3.17(c).

3.6.3 Analytical heat transfer modeling of the microspheres

It was also of interest to explore if the measured transient thermal behavior of AuNP-PEGDA microspheres characterized in Chapter 2 could be analytically modeled. Such a model would enable a direct comparison of the heat flows observed by DSC with the changes in temperature observed using the infrared camera. One of the simpler analytical heat transfer models is the lumped capacitance model. This model makes the assumption that temperature gradients within the solid are neglected. To confirm that the lumped capacitance method is valid for this case, the Biot number (*Bi*) need be calculated. A critical parameter to the calculation of the Biot number is the heat transfer coefficient (*h*), equation 3.7.

$$h = \frac{Q}{A(T_{max} - T_{\infty})} \tag{3.7}$$

The convection coefficient is the ratio of heat flow (*Q*) from the object to the product of the surface area of heat transfer (*A)* and temperature difference (T_{max}-T_{∞}) of the object surface and surroundings. Using measured data of average temperature and heat flow of microsphere clusters from Chapter 2 with Q = 45.8 mW and (T_{max} - T_{∞}) = (98.8 – 26.5), with corresponding surface area of microspheres, the heat transfer coefficient was determined to be h = 23 W/m^{2}K. The Biot number was then calculated for a single microsphere according to equation 3.8.

$$B_i = \frac{h\,(r/3)}{k} = \frac{23\,(65 \times 10^{-6}/3)}{.69} = 7.2 \times 10^{-4} < 0.1 \tag{3.8}$$

Where k is the thermal conductivity and r is the radius. The Biot number (B_i) is a condition, which represents if conduction or convection heat transfer dominates within or from the object. Calculated Biot numbers below 0.1 are considered to be conduction dependent and above, convection dependent. Since the Biot number calculated in equation 3.8 is below 0.1, the lumped capacitance model was used to develop an analytical model of the transient temperature response of irradiated microspheres.

Using the calculated heat transfer coefficient and using the lumped capacitance model (derivation provided in Appendix A.6) to develop an equation representing a transient temperature response, equation 3.9, a calculated temperature response is compared against the temperature measured response, shown in figure 3.18.

$$T(t) = T_{\infty} + \frac{Q_{max}\tau_{conv.}}{m_{conv.}C_p}\left[1 - e^{-\frac{t}{\tau_{conv.}}}\right] \qquad 3.9$$

Where T_{∞} is the surrounding ambient temperature, Q_{max} is the maximum heat flow for the same sample mass ($m_{conv.}$) under irradiation, $\tau_{conv.}$ is the time constant, and C_p is the specific heat capacity.

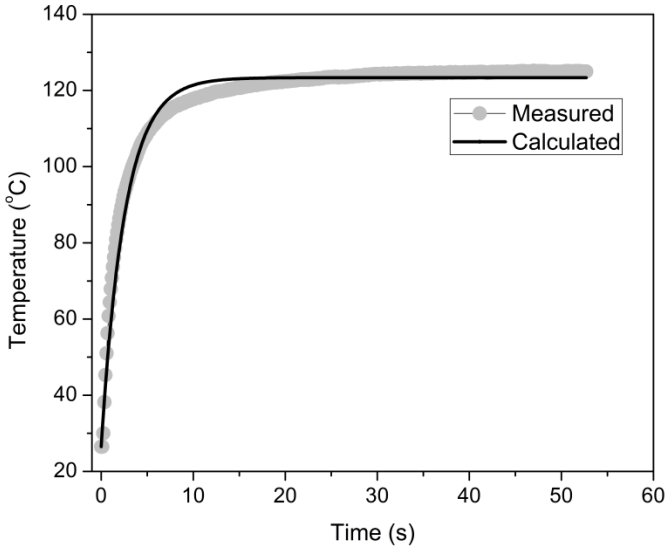

Figure 3.18: Comparing measured and calculated temperature response using the lumped capacitance model of irradiated microspheres.

The accuracy of equation 3.9 is quite high as the average difference between measured and calculated data in figure 3.18 is 1.6%. To conclude, this analysis suggests that the lumped capacitance model works well in predicting the transient temperature response compared with the observed heat flow data.

3.7 Microvalve

Ultimately we envisioned incorporating our actuator devices into on-chip valves (although the full implementation of this is beyond the scope of this thesis). Preliminary attempts at developing reversible microvalves were undertaken. To engineer a reversible device, it was necessary to construct a compartment/reservoir containing the wax that

could be placed next to a microfluidic channel, separated by an elastomeric membrane, as shown in Figure 3.19

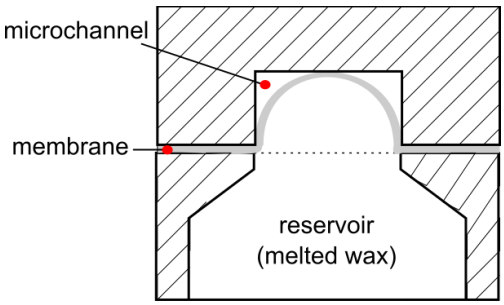

Figure 3.19: Diagram illustrating cross-section of a microvalve concept. A flexible elastomer membrane deforms against the sidewalls of a microchannel effectively stopping fluid flow. Melted wax contained in the reservoir expands the membrane, while the membrane reversibly contains the wax and prevents contamination of the wax with fluid in the microchannel.

3.7.1 Testing the microvalve

The idea in testing the microvalve was to delivery fluid from a syringe pump to both the inlet of the microvalve and to a bypass line. The fabrication details of the microvalve are provided in Appendix A.3. If the microvalve closed, the fluid would preferentially flow throw the bypass line. The outlet of the microvale line (outlet1) was integrated into a microdroplet generator, as used to manufacture microspheres in Chapter 2, where droplets would emerge if the valve was open, and none would emerge if the valve was closed, figure 3.20. In this setup, the flow rate of the microvalve was measured indirectly. The flow rate was therefore measured by observing the formation rate of microdroplets. All that is then needed to calculate flow rate of the aqueous phase emerging from the valve (figure 3.20, outlet1) is the flow rate of the organic phase, number of spheres that form in a unit of time, and the volume of each sphere.

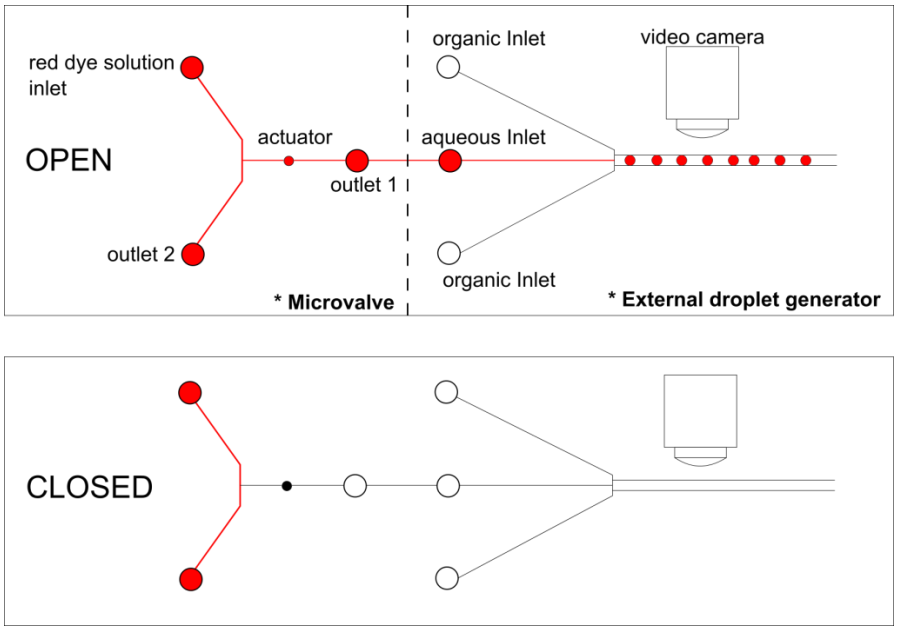

Figure 3.20: Concept illustrating indirect method for microvalve flow rate measurement. In the 'OPEN' state, fluid from the inlet flows through both outlet 1 and 2, where droplet formation is observed in an external device. When the photo-responsive gold nanoparticle composite is irradiated, the valve translates to the 'CLOSED' state and no droplets emerge in the external device.

In figure 3.20, when the valve is open, fluid is directed to an external device where microdroplets are observed with a video camera. When the valve is closed, the laser is irradiant on the actuator cavity and no droplets emerge at the nozzle of the external microfluidic device. This can also be seen in an actual photo, figure 3.21.

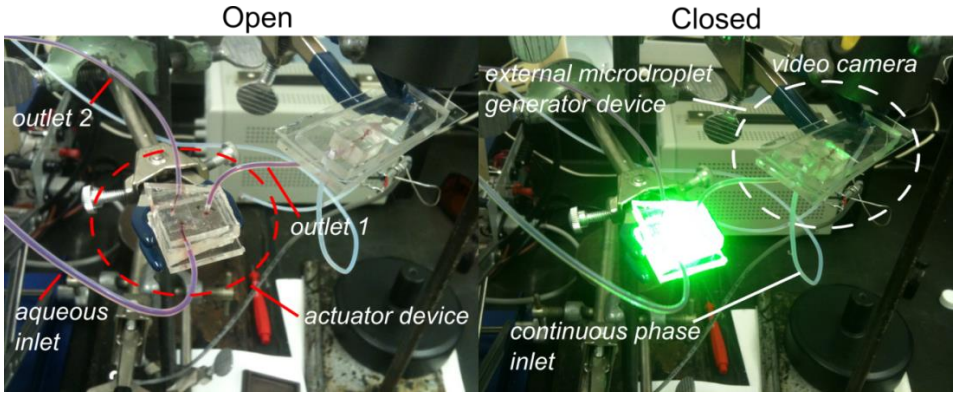

Figure 3.21: Photo of the components of the microvalve during measurement.

The flow rate of inlet 1 was experimentally set to a maximum of 2 µL/min, above which the valve appeared to not stop the flow at all. Also, by starting with a high flow rate, above 2 µL/min, then lowering the flow rate jeopardized the open-close cycle of the valve indefinitely. The reason may be due to an imperfectly sealed reservoir. For instance, it was thought that the fluid force acting on the actuator membrane would

deform its shape, effectively permitting fluid to preferentially flow through the deformed area.

Measuring flow rate from the microvalve was obtained from a custom particle counting algorithm developed in matlab (code is provided in Appendix A.5.2). In general, the flow rate was determined from individual peaks, representing a microdroplet passing through a 'particle counter'. The valves performance was measured for two cycles, after which the valve did not close, figure 3.22(a).

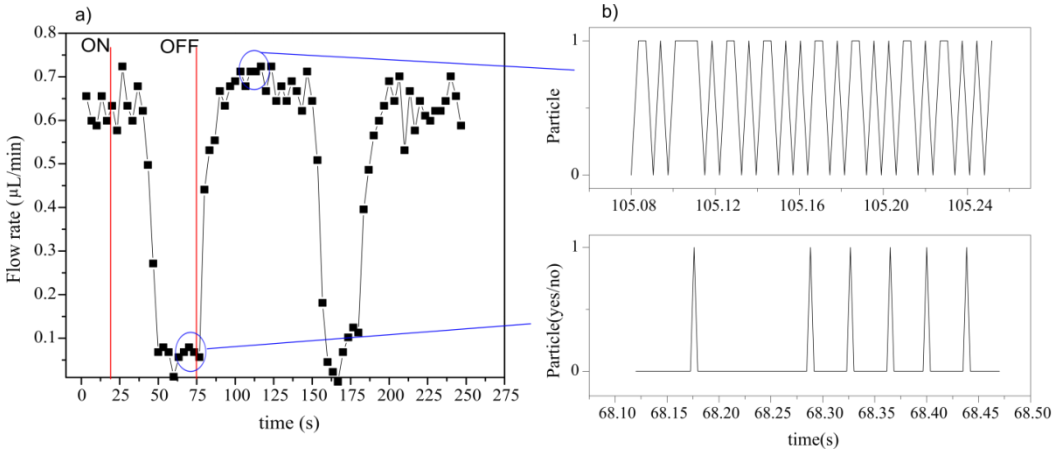

Figure 3.22: Flow rate of the valve showing open-close cycle. a) Flow rate versus time with a maximum of two open-close cycles observed of the valve upon laser irradiation. b) Magnified view of the flow rate data representing droplet peaks in time.

It is evident that when the valve is closed, a flow rate still persists, perhaps better termed as a throttle, with the counting of fewer particles. The fact that the valve did not completely shut may be due to the actuator membrane not completely displaced or the fluid pressure buildup effectively migrating fluid around the membrane and breaking the seal. Out of 20 devices, three devices worked with one open-close cycle, while one device demonstrated 2 close-open cycles before completely failing to close. Ideas to improve the design in the future will be discussed in Chapter 4.

3.8 Discussion

The optically selective microactuator containing a composite of microspheres with a loading of 0.123 wt% AuNPs and phase change PEG wax (Mn 1100 g/mol), demonstrated reversible actuation cycles using a hand held 72 mW laser source. Both the mass loading of PEG wax in the actuator reservoir and the irradiant power on the composite affected the performance of the actuator showing vertical displacements of the actuator in the range 42 to 110 µm. Additionally, the response of the actuator was quite

fast as a displacement of 20 μm could be reached in 10 s, while a displacement of 90 μm could be reached in 100 s for a particular actuator. Integration of the microactutor with a microchannel, effectively forming a microvalve, also revealed throttled control of fluid flow. Thermal modeling of the microactuator demonstrated that as the reservoir decreased in size, while the heat flow remained constant, the time to melt PEG wax in the reservoir decreased exponentially. The scaling prediction provides a line of sight for practical implementation for future devices, since this particular actuator can possibly operate on the order of milliseconds if the reservoir size decreases.

Chapter 4

Future work and conclusions

Several ideas are proposed in this chapter to improve and/or improve the versatility of the photo-responsive nanoparticle composite and the photo-controlled microactuator. Additionally, possible applications for the microactuator demonstrated in this work are also described.

4.1 Nanoparticle-polymer composites

4.1.1 Tuning the optical absorbance of nanoparticles

In figure 1.2(b) of Chapter 1, it is observed that by changing the aspect ratio of the nanoparticle, high optical absorption occurs at wavelengths in the near-IR region. Human skin is transparent at wavelengths ~1100 nm, suggesting that nanoparticles that can *selectively* absorb and transduce energy upon irradiation at this wavelength, could be exploited for *in vivo* applications such as remotely activated drug release. Testing the viability of this idea would require selecting a nanorod (i.e., 80 nm long and 12 nm in diameter), embedding and fixing the nanorod in a polymer matrix, and irradiating the sample. Similar techniques such as the IR camera and DSC could be used to characterize the transduction efficiency. In general, gold (or other noble metal) nanoparticles with different sizes and or shapes (which are able to selectively absorb light at different wavelengths) could be utilized in close physical proximity to engineer actuators which can be controlled independently or in various environments.

4.1.2 Functionalizing nanoparticles with the polymer matrix

In section 2.5 of Chapter 2, agglomeration of nanoparticles with PEG wax via direct mixing was unavoidable unless gold nanoparticles were first polymerized in microspheres then dispersed in PEG wax. Manufacturing the microspheres added a level of complexity to the construction of the final devices. The composite could be simplified by chemically functionalizing the nanoparticles to render them stable in PEG wax, rather than encapsulating them in microspheres. Indeed other phase change waxes with different chemical functionality could also be explored, such as paraffins.

4.2 Optically controlled microactuator

4.2.1 Integrating the microactuator to form a microvalve

Two major challenges for developing a microvalve were the precise control in adding the photo-responsive microspheres and PEG wax into the actuator reservoir, and the formation of a seal between the actuated membrane and the microchannel. To accurately fill the reservoir, it is proposed that molten wax be injected (via mechanical control) into a similar elastomer-capped reservoir to fill to a height (h) which corresponds to a theoretical value (based on α of the wax), followed by cooling of the system to return the actuator to zero displacement, shown in figure 4.1(a). To form the microvalve, and to create a strong seal, it is suggested that the membrane deforms against a small hole which then prevents fluid flow, as illustrated in figure 4.1(b).

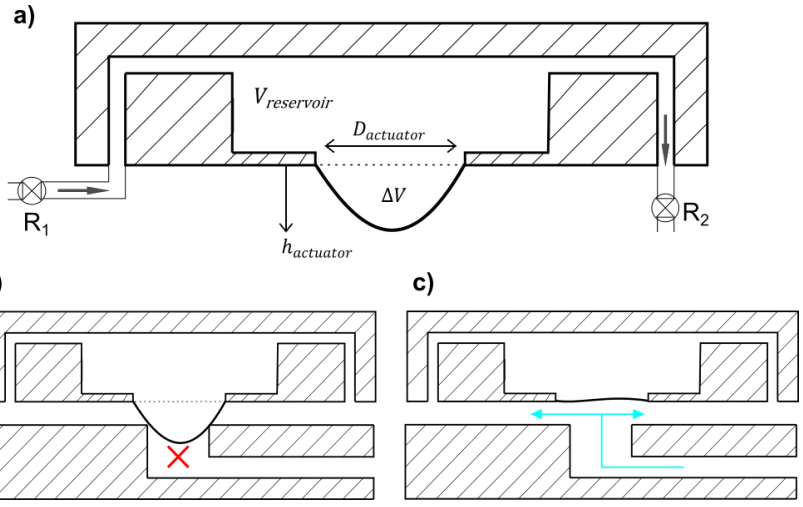

Figure 4.1: Proposed microvalve architecture. A) Filling the actuator reservoir with PEG wax by regulating the internal reservoir pressure by controlling the flow rate ratio R_2/R_1. B) Membrane of the actuator intercepting a small hole due to irradiation of the composite contained in the reservoir, which forms the valve. In this arrangement, no fluid flows due to a firm seal between the membrane and circumference of the hole. C) Irradiation of the reservoir stops, returning the actuator to zero displacement and opening the valve.

In figure 4.1(a) the volume of molten PEG wax added to the reservoir could be precisely controlled by a fine tuning of the ratio R_1/R_2 of the flow regulators to create a constant pressure in the reservoir that corresponds exactly to the change in volume (ΔV) of the actuator. This can also be controlled in a feedback mode whereby a displacement sensor controls R_2, so that the theoretical actuation height ($h_{actuator}$) is reached. Prior to installation of PEG wax to the reservoir, it may be necessary to perform a surface treatment, which would enable complete wetting of molten PEG with the inner surface area and hence prevent voids from forming. In addition, this approach would be most

effective if the NPs were predispersed in the wax, as described in Section 4.1.2, rather than needing to be added separately. The operation of the proposed microvalve can also be seen in figure 4.1(b and c) where irradiation of the reservoir containing the photo-responsive composite melts the wax effectively causing the valve to close, and opens when irradiation stops. Integrating the actuator with a small hole to form a microvalve will require innovative fabrication techniques. The benefit of having the actuator intercept a hole, opposed to a microchannel, in our design, is that the flexible membrane may conform more firmly within the circumference of the hole.

4.2.2 Implementation of photo-responsive microspheres to form multi-arrayed microvalves

When AuNP-PEGDA microspheres are hydrated, the volume expands by 28 %. If the same microspheres developed in this work can be individually isolated in microwells and sealed with an elastomer membrane, then upon hydration of the microsphere the membrane deforms. This deformation can be simply reversed by irradiating the photo-responsive microsphere, which effectively dehydrates the microsphere to its original volume. This scheme is illustrated in figure 4.2.

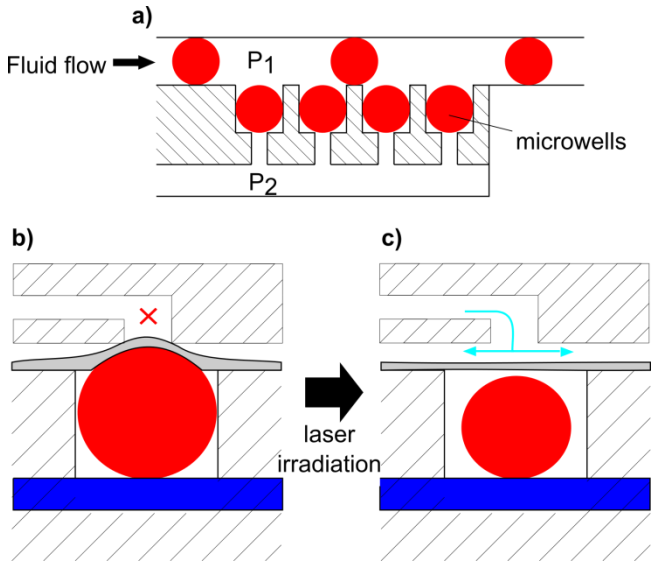

Figure 4.2: Proposed photo-responsive microsphere microvalve array. a) Method for isolating microspheres in microwells by developing a pressure drop ($P_1 > P_2$) across each well. b) Hydrogel-based microsphere expands due to uptake of water from the hydration layer, which closes the valve. The hydration layer is expected to be of large size relative to the sum of microspheres, so that it remains constantly hydrated. c) Upon laser irradiation of the microsphere, water locally evaporates effectively shrinking the microsphere and opening the valve.

Individual microspheres can be isolated in microwells by establishing a pressure drop ($P_2 < P_1$) across the microwell. When microspheres are passed through the main channel, they become fixed in the well due to the low pressure, as shown in figure 4.2(a). Upon innovative fabrication steps, the idea is that the microsphere contacts two surfaces: an elastomer membrane for actuation and a hydration layer. Once the membrane deforms it compresses against a small hole, which forms a seal and prevents fluid flow, figure 4.2(b). When the laser stops irradiating the microsphere, moisture is suspected to evaporate from the microsphere, which effectively shrinks in volume and permits fluid flow, figure 4.2(c). The hydration layer is viewed to be very large relative to the sum of microspheres so that upon moisture uptake from a microsphere, the local moisture-deprived region in the hydration layer becomes immediately saturated again. It would be necessary that a water reservoir on the chip continuously feed the hydration layer.

4.2.3 Testing actuation time versus reservoir radius

At the end of Chapter 3, thermal modelling of the microactuator predicted that the time to melt wax in the reservoir reduces exponentially with respect to the reservoir radius. For example, if the heat source was a single microsphere (130 μm in diameter) embedded in a volume of PEG wax (200 μm in diameter), irradiated with the same 72 mW laser, the theoretical time to melt the PEG wax is 60 ms. It would be interesting to test this prediction to perhaps improve aspects of the heat transfer model or to demonstrate that wax-based microactuators are potentially good candidates for portable microfluidic platforms. A simple measurement scheme to test this prediction is illustrated in figure 4.3. If the same laser is to be used in this analysis, then the beam diameter must be scaled to an appropriate size equivalent to the effective reservoir diameter with the use of a concave lens.

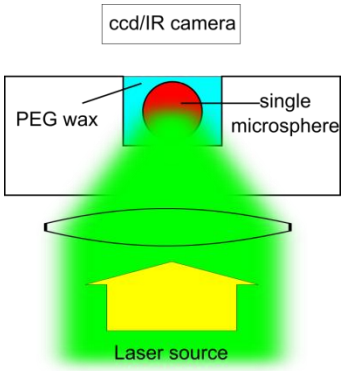

Figure 4.3: Illustration for single microsphere irradiation and melting time for surrounding phase change wax.

The challenge in implementing the measurement setup illustrated in figure 4.3 is in the materials handling and processing. Installing both a minute volume of PEG wax and a single microsphere into the microwell will be the single most challenge. Fabricating the microwell can be simply achieved by hot embossing a pattern in COC or PMMA. On the other hand, inserting a microsphere 130 μm in diameter into the microwell is not trivial. This may be achieved iteratively by using an x-y-z micrometer with a needle mounted to a stage probe where upon contact of the needle and a microsphere, the two bind upon a passive electrostatic force or by charging the needle. The microsphere can be released into the well by aligning and lowering the probe then slightly wetting the chamber, which enables the microsphere to preferentially adhere to the water, as the microsphere is hydrophilic. Installing PEG wax into the well can be achieved by coupling a low volume syringe needle with a micrometer dial. It is important that the needle of the syringe be first hydrophobically coated. By carefully adjusting the micrometer, an extremely small volume (~ 3 nL) of PEG wax will emerge at the tip of the needle. The needle will then be lowered to make contact with the sphere in the well, effectively wetting the entire surface. An alternative is to eliminate the chamber and to fix isolated microspheres to a substrate followed by spin coating PEG wax to a desired height. Microspheres can be isolated on a substrate by a trial and error process by perhaps pipetting dilute solutions of water containing microspheres onto an adhesive base, followed by air drying and pressing the spheres into the adhesive with the backing layer that was first removed from the adhesive.

4.2.4 Optically controlled variable displacement microactuator

Referring to figure 3.13 in Chapter 3, it is noticed that lower irradiation powers lead to different actuation heights that eventually reach an asymptotic maximum. This is

interesting since it implies that variable irradiant power leads to corresponding unique actuation heights. Complete melting of the wax in the reservoir does not occur at lower irradiant powers due to heat loss from the heat source and surrounding wax to the surroundings. Thus a fine balance of energy in to energy out regulates the displacement height of the actuator. To exploit this consequence, two applications are proposed: an optically controlled variable diffraction grating and an analog capacitor described below.

The variable diffraction grating operates by the actuator changing the grating period of a patterned material, which effectively changes the diffracted wavelength relative to the incident wavelength. The grating equation (equation 4.1) for diffraction can be implemented into the design to determine the range of wavelengths for a change in strain of the patterned material.

$$n(\sin(\theta_m) - \sin(\theta_i)) = \frac{m\lambda}{d} \qquad 4.1$$

Where n is the index of refraction of the material, θ_i is the incident angle of the beam, θ_m is the diffracted angle of the beam, m is the order of diffraction, λ is the wavelength of light, and d is the grating period. In our design the actuator displaced a maximum of 110 µm. If patterned elastomeric material (i.e. PDMS) originally 500 µm long was specially attached to the actuator, the total strain that could be imposed on the film is $\varepsilon = \Delta L/Li = .22$. Since λ/d is constant (constant angle of incidence and diffraction), if the starting wavelength is equal to $\lambda = 400$ nm, the final wavelength when the material is strained is $\lambda = 488$ nm. It can be seen that by making smaller Li, the wavelength range can be further increased.

For the variable capacitor, the idea is to simply construct two parallel plate capacitors with a dielectric fluid containing pure water and barium titanate nanoparticles as a high dielectric constant medium ($\varepsilon_m > 1000$). From the capacitance formula (equation 4.2), and based on the range of the actuator in this work (1 to 110 µm), the variable capacitor could operate over the range 17 to 0.16 nF – by changing the spacing distance between plates.

$$C = \varepsilon_o \varepsilon_m \frac{A}{d} \qquad 4.2$$

Where C is the capacitance, A is the area of parallel plates (100 µm X 100µm in this example), ε_o is the permittivity of a vacuum, ε_m is the permittivity of the dielectric material, and d is the plate separation distance.

4.2.5 LED Stimulation of the photo-responsive composite

Original work showed that light emitting diodes, at an irradiation intensity of 74.3 mW/cm^2, and at peak 532 nm intensity could also work as a stimulation source (rather than lasers), from which energy could be transduced by AuNP-PEGDA composites, as shown in figure 4.4.

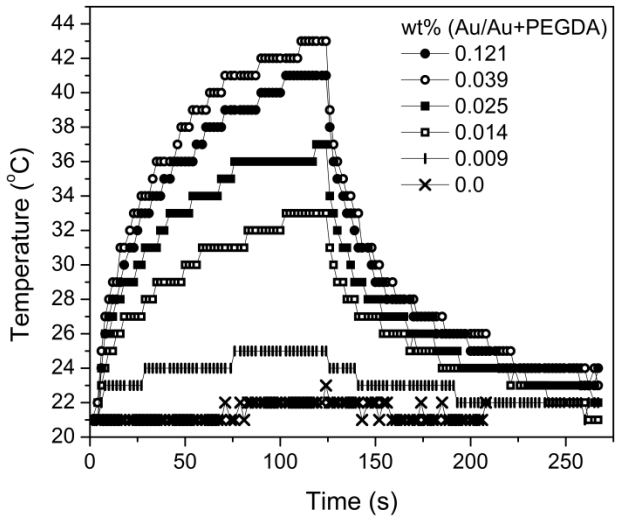

Figure 4.4: LED irradiation of AuNP-PEGDA microspheres at different concentrations.

As high temperatures were also achieved, as seen in figure 4.4 (i.e., above PEG wax's melting temperature), LED irradiation also demonstrate the possibility working as a remote stimulation source. Due to the ubiquity and low cost of high power LEDs, it is suggested that a single LED coupled with a converging lens irradiate a small volume of microspheres embedded in wax (or a single wax NP composite as mentioned in section 4.1.2) and in a reservoir sealed with a membrane, to also demonstrate microactuation. The advantage of LEDs over a laser is that a single LED occupies far less space for on-chip integration.

4.3 Conclusions

This thesis describes the synthesis of unique photo-responsive microspheres containing gold nanoparticles that resist agglomeration when dispersed in other chemical media and when thermally cycled in this media above and below its solid-liquid phase transition temperature, such as PEG wax. At a predetermined irradiant wavelength, the photo-responsive microspheres containing gold nanoparticles absorb and transfer energy at high efficiency due to a thermalization process during surface plasmon resonance within each nanoparticle. Under optical irradiation from a portable laser, the AuNP – polymer microsphere heaters transduced an average > 70% of the electromagnetic energy to heat, reaching a maximum temperature of 125 ºC in air. We then combined the microspheres with a phase change wax and developed a reversible microactuator that is activated remotely with a low power hand-held 532 nm laser. The microactuator demonstrated actuation heights between 42 and 110 μm, which depended on the volume of phase change PEG wax in the reservoir. An actuation cycle time less than 100 seconds with a vertical stroke height of 84 μm can be achieved for particular irradiation intensities and device characteristics. Thermal modeling of the microactuator showed that the time to melt wax in the reservoir reduces exponentially with respect to the reservoir radius. Our microactuator also serves to demonstrate that the displacement cycle time can be significantly reduced if scaled smaller, making the actuator reach practical stroke cycle periods for biologically based microfluidic platforms.

References

1. Sanchez, C., H. Arribart, and M.M.G. Guille, *Biomimetism and bioinspiration as tools for the design of innovative materials and systems.* Nature Materials, 2005. **4**(4): p. 277-288.
2. Stuart, M.A.C., et al., *Emerging applications of stimuli-responsive polymer materials.* Nature Materials, 2010. **9**(2): p. 101-113.
3. Sun, T.L. and G.Y. Qing, *Biomimetic Smart Interface Materials for Biological Applications.* Advanced Materials, 2011. **23**(12): p. H57-H77.
4. Xia, F. and L. Jiang, *Bio-inspired, smart, multiscale interfacial materials.* Advanced Materials, 2008. **20**(15): p. 2842-2858.
5. Yerushalmi, R., et al., *Stimuli responsive materials: new avenues toward smart organic devices.* Journal of Materials Chemistry, 2005. **15**(42): p. 4480-4487.
6. Stoeber, B., et al., *Flow control in microdevices using thermally responsive triblock copolymers.* Journal of Microelectromechanical Systems, 2005. **14**(2): p. 207-213.
7. Qiu, Y. and K. Park, *Environment-sensitive hydrogels for drug delivery.* Advanced Drug Delivery Reviews, 2001. **53**(3): p. 321-339.
8. Alarcon, C.D.H., S. Pennadam, and C. Alexander, *Stimuli responsive polymers for biomedical applications.* Chemical Society Reviews, 2005. **34**(3): p. 276-285.
9. Lendlein, A., et al., *Light-induced shape-memory polymers.* Nature, 2005. **434**(7035): p. 879-882.
10. Miyata, T., N. Asami, and T. Uragami, *A reversibly antigen-responsive hydrogel.* Nature, 1999. **399**(6738): p. 766-769.
11. Tanaka, T., et al., *Phase-transitions in ionic gels.* physical Review Letters, 1980. **45**(20): p. 1636-1639.
12. Tanaka, T., et al., *Collapse of gels in an electric-field.* Science, 1982. **218**(4571): p. 467-469.
13. Yoshida, R., et al., *Comb-type grafted hydrogels with rapid de-swelling response to temperature-changes.* Nature, 1995. **374**(6519): p. 240-242.
14. Baffou, G., R. Quidant, and C. Girard, *Heat generation in plasmonic nanostructures: Influence of morphology.* Applied Physics Letters, 2009. **94**(15).
15. Govorov, A.O., et al., *Gold nanoparticle ensembles as heaters and actuators: melting and collective plasmon resonances.* Nanoscale Research Letters, 2006. **1**(1): p. 84-90.
16. Khlebtsov, N.G. and L.A. Dykman, *Optical properties and biomedical applications of plasmonic nanoparticles.* Journal of Quantitative Spectroscopy & Radiative Transfer, 2010. **111**(1): p. 1-35.
17. Nearingburg, B. and A.L. Elias, *Characterization of surface plasmon energy transduction in gold nanoparticle/polymer composites by photo-DSC.* Thermochimica Acta, 2011. **512**(1-2): p. 247-253.

18. Richardson, H.H., et al., *Thermo-optical responses of nanoparticles: Melting of ice and nanocalorimetry approach.* Journal of Electronic Materials, 2007. **36**(12): p. 1587-1593.

19. Roper, D.K., W. Ahn, and M. Hoepfner, *Microscale heat transfer transduced by surface plasmon resonant gold nanoparticles.* Journal of Physical Chemistry C, 2007. **111**(9): p. 3636-3641.

20. Ueno, K., et al., *Spectral sensitivity of uniform arrays of gold nanorods to dielectric environment.* Journal of Physical Chemistry C, 2007. **111**(11): p. 4180-4184.

21. Sharma, V., K. Park, and M. Srinivasarao, *Colloidal dispersion of gold nanorods: Historical background, optical properties, seed-mediated synthesis, shape separation and self-assembly.* Materials Science & Engineering R-Reports, 2009. **65**(1-3): p. 1-38.

22. Anderson, R.R. and J.A. Parrish, *The optics of human-skin.* Journal of Investigative Dermatology, 1981. **77**(1): p. 13-19.

23. Sugiura, S., et al., *Photoresponsive polymer gel microvalves controlled by local light irradiation.* Sensors and Actuators a-Physical, 2007. **140**(2): p. 176-184.

24. Mathiowitz, E. and M.D. Cohen, *Polyamide microcapsules for controlled release .5. photochemical release.* Journal of Membrane Science, 1989. **40**(1): p. 67-86.

25. Seung Ki Baeki, Y.K.Y., and Jung Hwan Park, *Wirelessly actuated microvalve system using induction heating and its thermal effect on the microfluidic system, in Actuators and Microsystems Conference* (Transducers), 2011 16th International. 2011. p. 1304-1307.

26. Li, M.H. and P. Keller, *Artificial muscles based on liquid crystal elastomers.* Philosophical Transactions of the Royal Society a-Mathematical Physical and Engineering Sciences, 2006. **364**(1847): p. 2763-2777.

27. Figeys, D. and D. Pinto, *Lab-on-a-chip: A revolution in biological and medical sciences.* Analytical Chemistry, 2000. **72**(9): p. 330A-335A.

28. Metzker, M.L., *Applications of next-generation sequencing technologies - the next generation.* Nature Reviews Genetics, 2010. **11**(1): p. 31-46.

29. Mitchell, P., *Microfluidics - downsizing large-scale biology.* Nature Biotechnology, 2001. **19**(8): p. 717-721.

30. Richter, A., et al., *Electronically controllable microvalves based on smart hydrogels: Magnitudes and potential applications.* Journal of Microelectromechanical Systems, 2003. **12**(5): p. 748-753.

31. Zhang, C., D. Xing, and Y. Li, *Micropumps, microvalves, and micromixers within PCR microfluidic chips: Advances and trends.* Biotechnology Advances, 2007. **25**(5): p. 483-514.

32. Au, A.K., et al., *Microvalves and Micropumps for BioMEMS.* Micromachines, 2011. **2**(4): p. 179-220.

33. King, K.R., et al., *A high-throughput microfluidic real-time gene expression living cell array.* Lab on a Chip, 2007. **7**(1): p. 77-85.

34. Grover, W.H., et al., *Development and multiplexed control of latching pneumatic valves using microfluidic logical structures.* Lab on a Chip, 2006. **6**(5): p. 623-631.

35. Kim, D., et al., *Hydrodynamic fabrication and characterization of a pH-responsive microscale spherical actuating element.* Sensors and Actuators a-Physical, 2007. **134**(2): p. 321-328.

36. Oh, K.W. and C.H. Ahn, *A review of microvalves.* Journal of Micromechanics and Microengineering, 2006. **16**(5): p. R13-R39.

37. Kaigala, G.V., V.N. Hoang, and C.J. Backhouse, *Electrically controlled microvalves to integrate microchip polymerase chain reaction and capillary electrophoresis.* Lab on a Chip, 2008. **8**(7): p. 1071-1078.

38. Felton, M.J., *The new generation of microvalves.* Analytical Chemistry, 2003. **75**(19): p. 429A-432A.

39. Sethu, P. and C.H. Mastrangelo, *Polyethylene glycol (PEG)-based actuator for nozzle-diffuser pumps in plastic microfluidic systems.* Sensors and Actuators a-Physical, 2003. **104**(3): p. 283-289.

40. Satarkar, N.S., et al., *Magnetic hydrogel nanocomposites as remote controlled microfluidic valves.* Lab on a Chip, 2009. **9**(12): p. 1773-1779.

41. Chen, G., F. Svec, and D.R. Knapp, *Light-actuated high pressure-resisting microvalve for on-chip flow control based on thermo-responsive nanostructured polymer.* Lab on a Chip, 2008. **8**(7): p. 1198-1204.

42. Park, J.-M., et al., *Multifunctional microvalves control by optical illumination on nanoheaters and its application in centrifugal microfluidic devices.* Lab on a Chip, 2007. **7**(5): p. 557-564.

43. Chen, Y., T.-H. Wu, and P.-Y. Chiou, *Scanning laser pulses driven microfluidic peristaltic membrane pump.* Lab on a Chip, 2012. **12**(10): p. 1771-1774.

44. Jager, E.W.H., O. Inganas, and I. Lundstrom, *Microrobots for micrometer-size objects in aqueous media: Potential tools for single-cell manipulation.* Science, 2000. **288**(5475): p. 2335-2338.

45. Maitland, D.J., et al., *Photothermal properties of shape memory polymer micro-actuators for treating stroke.* Lasers in Surgery and Medicine, 2002. **30**(1): p. 1-11.

46. Aschwanden, M. and A. Stemmer, *Polymeric, electrically tunable diffraction grating based on artificial muscles.* Optics Letters, 2006. **31**(17): p. 2610-2612.

47. Nicoletta, F.P., et al., *Light Responsive Polymer Membranes: A Review.* Membranes, 2012. **2**(4): p. 134-197.

48. Sharma, A., et al., *Review on thermal energy storage with phase change materials and applications.* Renewable and Sustainable Energy Reviews, 2009. **13**(2): p. 318-345.

49. Menczel, J.D., *Thermal analysis of polymers*. 2009: John Wiley.

50. Seongok Han, C.K., Dongsook Kwon, *Thermal/oxidative degradation and stabilization of polyethylene glycol.* Polymer, 1997. **38**(2): p. 317-323.

51. Haes, A.J., et al., *Plasmonic materials for surface-enhanced sensing and spectroscopy.* Mrs Bulletin, 2005. **30**(5): p. 368-375.

52. El-Sayed, M.A., *Some interesting properties of metals confined in time and nanometer space of different shapes.* Accounts of Chemical Research, 2001. **34**(4): p. 257-264.

53. Kelly, K.L., et al., *The optical properties of metal nanoparticles: The influence of size, shape, and dielectric environment.* Journal of Physical Chemistry B, 2003. **107**(3): p. 668-677.

54. Amanda J. Haes, R.P.V.D., *A nanoscale optical biosensor: sensitivity and selectivity of an approach based on the loacalized surface plasmon resonance spectroscopy of triangular silver nanoparticles.* JACS, 2002. **124**: p. 10596-10604.

55. Jain, P.K., I.H. El-Sayed, and M.A. El-Sayed, *Au nanoparticles target cancer.* Nano Today, 2007. **2**(1): p. 18-29.

56. Jakobsohn, K., et al., *Towards real-time detection of tumor margins using photothermal imaging of immune-targeted gold nanoparticles.* International Journal of Nanomedicine, 2012. **7**: p. 4707-4713.

57. Qin, G., et al., *Partially polymerized liposomes: stable against leakage yet capable of instantaneous release for remote controlled drug delivery.* Nanotechnology, 2011. **22**(15): p. 155605.

58. Richardson, H.H., et al., *Experimental and Theoretical Studies of Light-to-Heat Conversion and Collective Heating Effects in Metal Nanoparticle Solutions.* Nano Letters, 2009. **9**(3): p. 1139-1146.

59. Balazs, A.C., T. Emrick, and T.P. Russell, *Nanoparticle polymer composites: Where two small worlds meet.* Science, 2006. **314**(5802): p. 1107-1110.

60. Garstecki, P., et al., *Formation of monodisperse bubbles in a microfluidic flow-focusing device.* Applied Physics Letters, 2004. **85**(13): p. 2649.

61. Tang, L. and N.Y. Lee, *A facile route for irreversible bonding of plastic-PDMS hybrid microdevices at room temperature.* Lab Chip, 2010. **10**(10): p. 1274-80.

Appendix A

Instrument calibration, fabrication procedures, LabView code and Matlab algorithms

A.1 Instrument and sensor calibration

A.1.1 IR camera calibration

To ensure all measurements carried out with the IR camera were correct (i.e., during irradiation of AuNP-PEGDA microspheres) it was necessary to first determine the accuracy of the IR camera with well-known references. To achieve this, the temperature of both an ice bath at 0ºC and water boiling at 100ºC were measured by both a mercury bulb thermometer and the IR camera. The emissivity value of wetted ice and boiling water was used as a corrective input into the IR camera.

A.1.2 Photodiode circuit and calibration

In this work, for irradiation measurements that involved power attenuations on the sample (sections 2.7.1 and 3.5.2), it was necessary to know the exact value of light power incident on the sample, for example, to determine transduction efficiencies. To achieve this, a photodiode was utilized. The photodiode was connected to a data acquisition module (DAQ) in order to collect a voltage signal proportional to the intensity of light.

The principal of the photodiode is that it transduces certain amounts of current in proportion to the quantity of incident light power at a certain frequency. The responsivity of the diode, or quantity of current per irradiant power, is unique for each electromagnetic frequency in the visible spectrum. The manufacturer provided an averaged curve of responsivity versus wavelength. However, as greatly emphasized from Thor Labs, each photodiode should be calibrated individually due to variability of sensor characteristics during its manufacture.

Since the photodiode generates a current in response to light and that the DAQ used only measured analog voltages, it was necessary to bridge the photodiode and DAQ with a current to voltage converter circuit (i.e., a resistor). The simplest circuit to achieve this conversion uses a voltage source, resistor, and the photodiode, figure A.1(a).

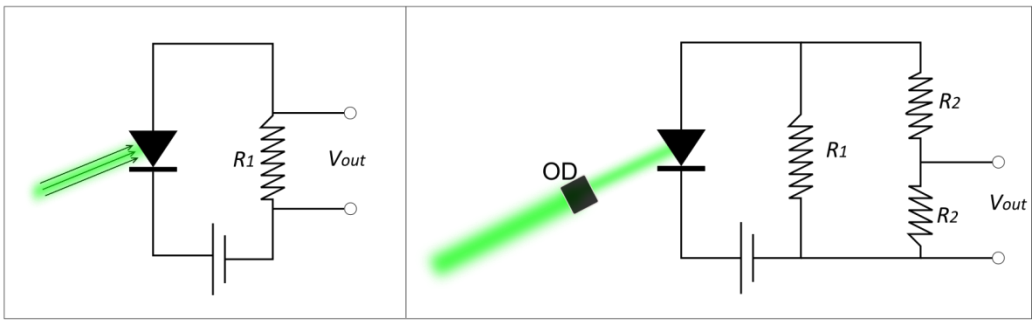

Figure A. 1: Photodiode calibration setup. a) Basic photodiode current to voltage circuit. b) Photodiode current to voltage and voltage divider circuit

The voltage source is biased to the photodiode, which improves the responsivity of the photodiode by increasing the bandgap energy. When current passes through resistor R_1, a voltage across the resistor is established. This voltage is then read by the DAQ.

Several circuit design consideration were made: (1) The value of R_1 is a key parameter that determines the speed of the response. A high value of R1 is desirable to give a fast response of the photodiode upon irradiation. It was experimentally found that R_1 should be greater than 1 kΩ and less than 10 kΩ. A resistor of 1052 ohms was chosen. (2) The size of the power supply was important since it should be able to provide enough voltage to pass at least 12.8 mA (estimated maximum power from the 72 mW laser) through R_1. A voltage source of 15 volts was sufficient. (3) The voltage range that the DAQ can read (± 10V) was also taken into account with respect to the voltage across R_1. If the photodiode is irradiated at 72.1 mW and R_1 is 1052 ohms, a potential of approximately 11 Volts across R_1 will be set. Since R_1 could be no less than 1000 ohms, to reduce the measured voltage for the DAQ, a voltage divider was the best solution. The value of R_2 was set to 99 kΩ, which halved the voltage, figure A.1(b).

To later calculate the current from the photodiode, it was necessary to establish a relationship between voltage and current. This was achieved by following the circuit in figure A.1, and taking into account the DAQ's built in impedance (R_L) of 200 kΩ, equation A.1.

$$V_{out} = \frac{(i_{diode} * R_1) * \left(\frac{R_2 R_L}{R_2 + R_L}\right)}{R_2 + \left(\frac{R_2 R_L}{R_2 + R_L}\right)} \qquad \text{A.1}$$

With resistors sized to convert the current to voltage and measured with a DAQ, the photo diode was then calibrated using optical density filters. Optical density filters attenuate light according to equation A.2.

$$T = I * 10^{-OD} \quad \text{A.2}$$

Where T is the transmitted power, I is the incident power on the filter, and OD is the optical density filter attenuation value. The OD value for each filter was measured, rather than taken from the specification sheet, using a spectrophotometer. Optical density (OD) filters with known magnitudes of attenuation intercepted the laser beam path incident on the photodiode. By applying a range of different OD filters versus measured voltage, and knowing the power of the laser, incident laser power versus measured voltage was obtained, with a responsivity profile in figure A.2.

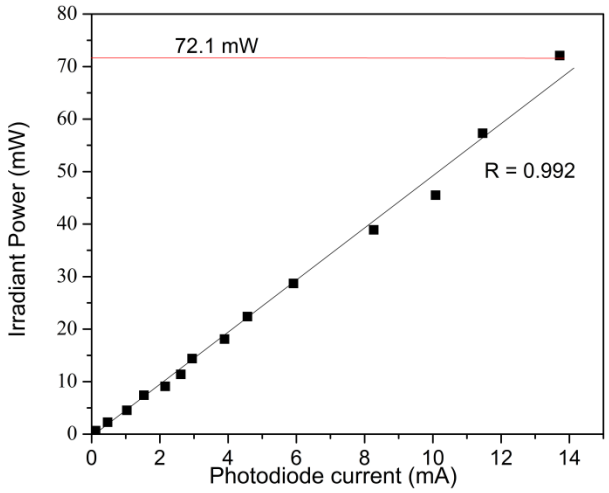

Figure A. 2: Calibration results of the photodiode

The measured responsivity of the photodiode was linear over the power range (3 to 72 mW) used in all our measurements. A linear equation was then fitted to the data in figure A.2 and used in all measurements to determine values of power. The fitted linear equation $y = 5.04x - 0.995$, where y = irradiant power and x = photodiode current.

A.1.3 Monodisperse microsphere emissivity calibration

To measure the temperature of the microspheres with the IR camera (section 2.7.1), the emissivity of the microspheres must be known. The emissivity of the AuNP-PEGDA microspheres was determined by comparing its observed temperature with a material with a known emissivity value, electrical tape, while both bodies were in thermal equilibrium with a heat source. To achieve this, a strip of electrical tape was applied to a glass slide, and monodisperse microspheres were pipetted next to this strip. Microspheres with different gold nanoparticle concentrations were also arranged. The glass slide was then placed on a hot plate and brought to a certain temperature, which was assumed to be the same for both the tape and the spheres. On the IR camera software, one can select specific regions of an area and assign different properties to that point. A point above the tape was selected, and the known emissivity value of the tape 0.97 was entered into the software, and a corresponding temperature was displayed. Similarly a point was selected over the microsphere sample and the emissivity value was adjusted until the same temperature as that of the electrical tape was observed. To verify that the emissivity value was constant over a given temperature range, the glass slide was heated and both the electrical tape and microsphere temperatures were independently recorded, with results shown in figure A.3.

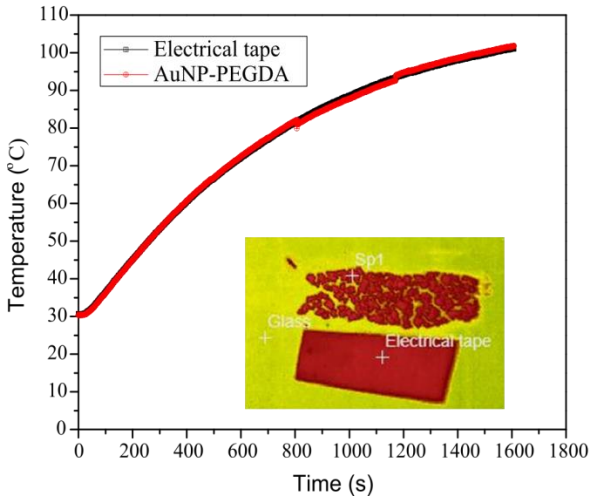

Figure A. 3: Calibration results of the emissivity of the AuNP-PEGDA microspheres

The result in figure A.3 shows that emissivity value selected for the AuNP-PEGDA microspheres (0.977) was constant over the temperature range 30-100 ºC, as the temperature of both the microspheres and electrical tape overlapped.

A.1.4 Force transducer calibration

In order to accurately measure the force applied by the actuator (as determined in section 3.5.2), a highly sensitive force transducer was employed. To achieve this, it was first necessary to calibrate the force transducer by coupling the force applied to the transducer with a high precision weigh scale. The mass the weigh scale measures upon an applied force by the probe of the transducer is proportional to the voltage from the transducer, with results shown in figure A.4.

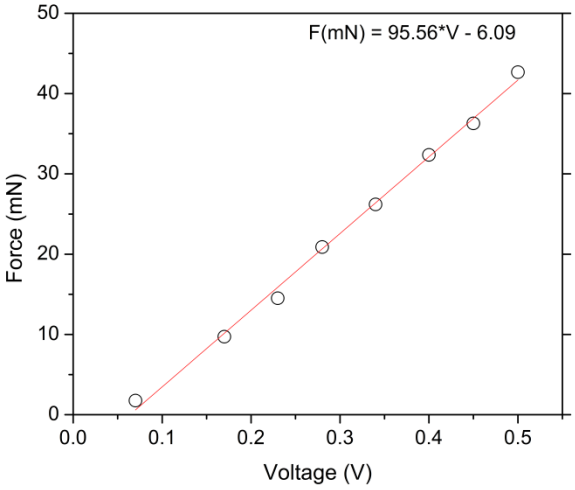

Figure A. 4: Force transducer calibration results

The results shown in figure A.4 show that the force (calculated from F = mg) was linear with respect to the voltage output from the transducer. A linear equation was then fit to the data and used to determine the force applied by the actuator. The fitted linear equation is $y = 95.56x - 6.09$, where y = force and x = voltage.

A.2 Microparticle Generator

The microdroplet generator used to make microspheres in section 2.6.1 is described. The materials used in its construction include: Test grade, 525 um thick, p-type, <100>, single

side polished silicon wafers, KMPR photoresist, trichloro(1H,1H,2H,2H-perfluorooctyl)silane, PDMS (Sylgard 184, Dow Corning), and Aquapel glass treatment solution (PPG Industries).

The fabrication of the microparticle generator is summarized as follows. A chrome-on-glass photomask depicting the microparticle generator geometry was produced using a pattern generator (Heidelberg DWL-200), figure A.5.

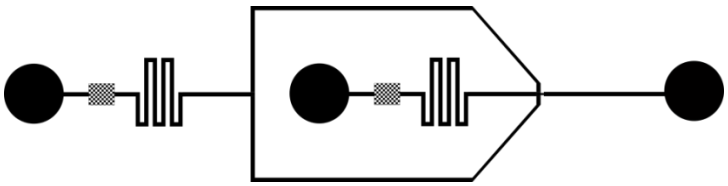

Figure A.5: Geometry used to create a photomask for the microdroplet generator.

Silicon wafers were cleaned in a piranha solution (3:1 H2O2:H2SO4) for 15 minutes. A 35 micron thick KMPR photoresist layer was spin coated at 4000 rpm for 1 minute, followed by a 12 minute bake at 100 ºC. The coated wafer was selectively irradiated with 500 mJ/cm^2 of UV light through the photomask. The wafer was baked at 100°C for 2 min and then developed in SU-8 developer solution for 2 min. The KMPR patterned silicon wafer was etched 140 microns deep with the use of a deep reactive ion etcher (ICPRIE STS), with the etched master shown in figure A.6.

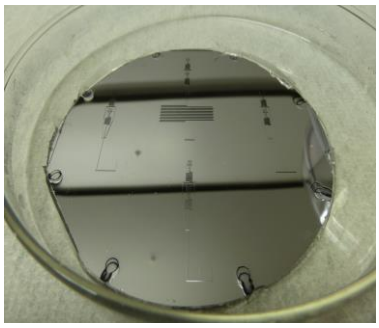

Figure A.6: Microdroplet generator silicon master.

The silicon surface was then silanized with trichloro(1H,1H,2H,2H-perfluorooctyl)silane. A 10:1 mixture of PDMS elastomer and curing agent was coated

onto both a blank 3 mm thick silicon substrate and the patterned silicon substrate, and was then cured at 80 ºC for 2 hrs. Both PDMS slabs were peeled off of the substrates, exposed to a UV-ozone bonder, aligned and then pressed together, forming an irreversible bond surrounding the channels. All the preceding steps took place in the University of Alberta's Nanofab facility. Inlet holes were then punched out in the blank PDMS slab. The Aquapel glass treatment solution was finally pumped through the channels making them hydrophobic.

A.3 Microvalve

Section 3.7 of this thesis discusses the incorporation of the stimulus responsive material into a microvalve with an eye on applications in microfluidic devices. In general, the microvalve was assembled by aligning the microactuator described in Chapter 3 with a separate layer containing a microchannel patterned in PDMS, to form the device which was shown in figure 3.19.

To design the microchannel (defined by width and height), on which the actuator intercepts, it was a matter of determining the width and height of the microchannel suitable to create a seal with the sidewalls of the channel and membrane of the actuator. To obtain a good seal between the flexible membrane of the actuator and the channel, it was necessary to make a channel smaller than the cross sectional area of the actuator, since the membrane would expand in the channel axis once contact was made with the side walls. To determine the channel dimensions, a fraction of the cross section of the perimeter from an actuator displaced to a height of 100 µm was calculated and set as the perimeter of the microchannel. Then, the width and height of the channel dimensions were changed until reasonable values were found, for example, it made sense to make both the width and height of the channel closely match the width and height of the actuator, however, slightly smaller. The dimensions of the microchannel were selected as 200 µm in width and 70 µm in height. This decision was also influenced from the fact that the actuator displaced above 70 µm in height.

The fabrication steps to make the silicone masters used to mold microchannel layers with different channel widths and height, was identical to the procedure described

above in section A.2. The actuator (fabrication steps described in section 3.4) and the microchannel layer were then activated in a UV ozone bonder for 1 minute. The samples were quickly removed, aligned with an x-y-z micrometer, then mated and compressed overnight.

A.4 LabView Code

LabView was the software used to interpret the data generated from the DAQ in all irradiation measurements. The code structure used for the feedback-control loop to measure the photodiode and power is provided in figure A.7.

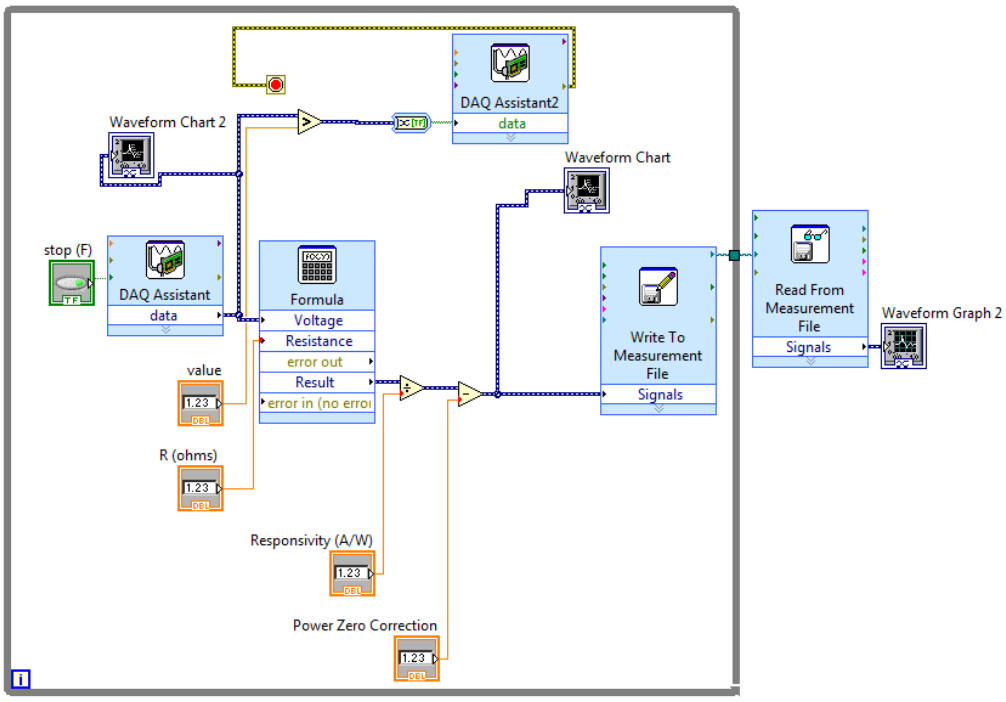

Figure A.7: LabView code

A.5 Matlab Code

A.5.1 Displacement of the microactuator

Matlab was utilized to convert all image files into matrix data from all actuations measurements. A sequence of image frames (from video) was analyzed for the actuator displacement and converted into numerical data according to the following code. The general scope of the program is an edge detection algorithm that determines the location of an edge at a common x-location for each frame in the video sequence.

```
   clear all

vid = VideoReader('EAZ3.33.18-12a.avi');

Is = read(vid, [1 vid.NumberOfFrames]);

%Read every nth frame
n = 10;
Ic = Is(:,:,:,1:n:size(Is,4)); %store every nth frame in new variable Ic
nFrames = size(Ic, 4); % Determine the new number of frames

%Determine region of interest.  Determine by first selecting area of
%interest and copying and pasting, this reduces future computation.
roi = [475.5 133.5 460 876]; %Select upper and lower X Y limits of interest
frame1 = Ic(:,:,:,1); %grab first frame in the new variable Ic
frameRegion = imcrop(frame1, roi); %crop first frame
%Create new matrix with uint8 (copies of zero) copies determined by size
%and nframes
regions = repmat(uint8(0), [size(frameRegion) nFrames]);
%Copy dimensions of frame1 and apply it to all others
for p = 1:nFrames,
    regions(:,:,:,p) = imcrop(Ic(:,:,:,p), roi);
end

%Create new logical zero matrix segImage with m, n and p determined by size() and
nFrames
segImage = false([size(frameRegion, 1) size(frameRegion, 2) nFrames]);
 for count = 1:nFrames,
    % Convert to grayscale.
    fr = regions(:,:,:,count);
    gfr = rgb2gray(fr);
    %level = graythresh(gfr);
    %Convert to logical black(0) and white(1)
    bw = im2bw(gfr,.31); %or experimentally determine threshold value
    segImage(:,:,count) = bw;
```

```
 end

 %Play converted video if desired
 %implay(segImage)

%Open an image to determine vertical range over which the for loop looks at
%the 0/1 interface
y_max = 350;
y_min = 50;
xm_const = 120;

%First loop to jump to next frame
for m = 1:nFrames
    %Second loop to look at each frame to determine 0/1 interface location
    %of membrane
    for k = y_max:-1:y_min %decrement by 1 from above the membrane
        P(k) = segImage(k, xm_const, m); %new variable P containing array of
vertical locations
        %if second loop encounters a logical 1 (starting in logical 0s)
        %break out of loop and store location in new variable H
        if P(k) == 0
            H(m) = k;
            break
        else
            H(m) = 130; %this is the y location of the membrane at zero
displacement
        end
    end
end

%Determine the time range at trigger point when laser begins irradiating.
%Idea is to look at intensity values
for x = 1:nFrames
TM(:,:,:,x) = impixel(regions(:,:,:,x),80,619); %Create 4D matrix of RGB values
for each frame
end
 Blueframes=TM(3,1,:,1:nFrames);
 for a = 1:nFrames
D(a) = double(Blueframes(a));
end

%Convert pixel thickness to true micron thickness
ImageWidth = 100; % pixel value
RefThickness = 60; %microns
PixelsPerMicron = ImageWidth/RefThickness;
Hmic = (H-130)/PixelsPerMicron;

%Convert frames into seconds
```

```
TimePeriod = (vid.Duration/vid.NumberOfFrames)*size(Is,4)
FramesPerPeriod = TimePeriod/nFrames;
for m = 1:nFrames
    Time(m) = FramesPerPeriod*m;
end
t =Time(1:nFrames);
x = Hmic(1:nFrames);
l = D(1:nFrames);
T = t';
X = x';
L = l';
A = [T X L];

%xlswrite('7.xls', A, '7d', 'A1');

%Plot Displacement versus time
figure;
plot(Time(1:nFrames),Hmic(1:nFrames),'--rs','LineWidth',1,'MarkerEdgeColor','k',
'MarkerFaceColor','g','MarkerSize',5)
title('Membrane Dynamics');
xlabel('time (s)');
ylabel('Displacement (microns)');
```

A.5.2 Microvalve flow rate

Using a derivative of the above program, droplets are instead counted over a time bin and multiplied by the volume within a droplet for the given number of droplets within each time bin, to determine flow rate.

```
   clear all

vid = VideoReader('SDV_0265.MP4');

Is = read(vid, [2001 3000]);

n = 1;
Ic = Is(:,:,:,1:n:size(Is,4));
nFrames = size(Ic, 4);
roi = [248.5 223.5 104 72];
frame1 = Ic(:,:,:,1);
frameRegion = imcrop(frame1, roi);
regions = repmat(uint8(0), [size(frameRegion) nFrames]);

for p = 1:nFrames,
    regions(:,:,:,p) = imcrop(Ic(:,:,:,p), roi);
```

```
end
segImage = false([size(frameRegion, 1) size(frameRegion, 2) nFrames]);
 for count = 1:nFrames,
    % Convert to grayscale.
    fr = regions(:,:,:,count);
    gfr = rgb2gray(fr);
    %level = graythresh(gfr);
    %Convert to logical black(0) and white(1)
    bw = im2bw(gfr,.76);
    segImage(:,:,count) = bw;
 end


for m = 1:nFrames
    P = segImage(30:50, 79, m); %new variable P containing array of vertical
locations
        %if second loop encounters a logical 1 (starting in logical 0s)
        %break out of loop and store location in new variable H
   avg(m) = sum(P)/(20);
   if avg(m) > .999
       H(m) = 0;
   else
       H(m) = 1;
   end

end
timestep = 34/vid.NumberOfFrames
for i = 1:7;
    Vdot(i) = (sum(H((100*(i-1)+1):100*i)))/(33.5/7); %Flow rate calculation
    TimePeriod(i) = (33.35/7)*i;
    end

v = H(900:1000);
t = timestep*(900:1000);

C = [t' v'];
xlswrite('Valvefrequency.xls', C, 'b', 'A1');

 plot(timestep*(900:1000), H(900:1000),'--rs','LineWidth',1,'MarkerEdgeColor','k',
'MarkerFaceColor','g','MarkerSize',5)
```

A.6 Heat transfer derivation

$$\dot{E}_{generation} = -\dot{E}_{convection} \quad \text{A.3}$$

$$mC_p \frac{dT}{dt} = -C(T_{max} - T) \quad \text{A.4}$$

$$Where:\ \ \theta = T_{max} - T, \qquad \theta_i = T - T_\infty, \qquad \theta_{max} = T_{max} - T_\infty \tag{A.5}$$

$$T_{max} = Constant \rightarrow \frac{d\theta}{dt} = -\frac{dT}{dt} \tag{A.6}$$

$$mC_p \frac{d\theta}{dt} = C\theta \rightarrow \frac{mC_p}{C}\int_{\theta_i}^{\theta_{max}} \frac{d\theta}{\theta} = \int_0^t dt \rightarrow \frac{mC_p}{C} \ln\left[\frac{\mathrm{T_{max}} - \mathrm{T_\infty}}{\mathrm{T} - \mathrm{T_\infty}}\right] = t; \quad \tau = \frac{mC_p}{C} \tag{A.7}$$

$$\frac{\mathrm{T} - \mathrm{T_\infty}}{\mathrm{T_{max}} - \mathrm{T_\infty}} = \frac{(\mathrm{T_{max}} - \mathrm{T_\infty}) - (T_{max} - T)}{\mathrm{T_{max}} - \mathrm{T_\infty}} = \frac{\theta_{max} - \theta}{\theta_{max}} = e^{-\frac{t}{\tau}} \rightarrow 1 - \frac{\theta}{\theta_{max}} = e^{-\frac{t}{\tau}} \tag{A.8}$$

$$\theta = \theta_{max}\left[1 - e^{-\frac{t}{\tau}}\right] \tag{A.9}$$

$$Since\ \dot{Q} = C(T_{max} - T) = C\theta, and\ C = \frac{mC_p}{\tau} \tag{A.10}$$

$$\dot{Q}(t) = \frac{m_{cond.}C_p}{\tau_{cond.}}\theta_{max}\left[1 - e^{-\frac{t}{\tau_{cond.}}}\right] \tag{A.11}$$

$$T(t) = T_\infty + \frac{Q_{max}\tau_{conv.}}{m_{conv.}C_p}\left[1 - e^{-\frac{t}{\tau_{conv.}}}\right] \tag{A.12}$$

Note that for convection $C = hA$, while for conduction $C = kA/L$. Where h is the convection coefficient, A is surface area of heat transfer, k is the thermal conductivity of the conduction body, and L is the length over which a temperature gradient is developed in the conduction body.